

Engineering 4D Regulation Toolbox to Control Spatiotemporal Cell-free Reconstitution



Haiyang Jia

München 2019

Engineering 4D Regulation Toolbox to Control Spatiotemporal Cell-free Reconstitution

Dissertation
an der Fakultät für Biologie
der Ludwig-Maximilians-Universität
München

vorgelegt von
Haiyang Jia
aus Zhangjiakou/Hebei, China

München, den 20.06.2019

Erstgutachter: Prof. Kirsten Jung
Zweitgutachter: Prof. Thorben Cordes
Tag der Einreichung: 26.06.2019
Tag der mündlichen Prüfung: 18.09.2019

Eidesstattliche Erklärung

Hiermit versichere ich an Eides statt, dass die vorliegende Dissertation von mir selbstständig und ohne unerlaubte Hilfe angefertigt wurde. Des Weiteren erkläre ich, dass ich nicht anderweitig ohne Erfolg versucht habe, eine Dissertation einzureichen oder mich der Doktorprüfung zu unterziehen. Die Dissertation liegt weder ganz, noch in wesentlichen Teilen einer anderen Prüfungskommission vor.

München, 20. June 2019

Haiyang Jia

Contents

Eidesstattliche Erklärung	III
List of Publications	IX
Summary	XI
1 Introduction	1
1.1 The prospect of building a synthetic cell	2
1.2 Membranes and microenvironments	4
1.2.1 2D model membrane.....	4
1.2.2 2.5D and 3D model membrane.....	5
1.3 Cell free transcription-translation machinery.....	8
1.3.1 Transcription and translation regulation tools	9
1.3.2 Cell free genetic circuits	9
1.3.3 Compartmentalized cell free system towards a synthetic cell	10
1.4 Cytoskeleton for spatial control and support.....	12
1.5 Objective of this thesis.....	15
2 Results	17
2.1 Temperature-sensitive protein expression in protocells.....	18
2.1.1 Supp. for Temperature-sensitive protein expression in protocells.....	23
2.2 Light-induced Printing of Protein Structures on Membrane <i>in vitro</i>	33
2.2.1 Supp. for Light-induced Printing of Protein Structures on Membrane <i>in vitro</i>	42
2.3 Shaping membrane vesicles in 3D-printed protein hydrogel cages.....	63

2.3.1	Supp. for Shaping membrane vesicles in 3D-printed protein hydrogel cages	83
2.4	Active forces driving 4D protein hydrogel origami.....	96
3	Discussion and Perspective	109
	Bibliography	114
	Abbreviations	119
	Acknowledgments	121

List of Publications

The following publications and manuscripts are included in this thesis:

Research articles

Jia, H., Kai, L., Heymann, M., Härtel, T., Kai, L., & Schwille, P. (2019). Temperature-sensitive protein expression in protocells. **Chemical communications**, DOI: 10.1039/c9cc02734c. (**First Author**)

Jia, H., Kai, L., Heymann, M., García-Soriano, D. A., Härtel, T., & Schwille, P. (2018). Light-induced Printing of Protein Structures on Membranes *in vitro*. **Nano letters**, 18(11), 7133-7140. (**First Author**)

Jia, H., Litschel, T., Heymann, M., Eto, H., Franquelim, Henri G., & Schwille, P. Shaping membrane vesicles in 3D-printed protein hydrogel cages, submitted. (**First Author**)

Jia, H., et. al., Active forces driving 4D protein hydrogel origami, in preparation. (**First Author**, the order for the other authors is still not defined)

Review articles:

Jia, H., Heymann, M., Bernhard, F., Schwille, P., & Kai, L. (2017). Cell-free protein synthesis in micro compartments: building a minimal cell from biobricks. **New biotechnology**, 39, 199-205. (**Shared First Author**)

Jia, H., Schwille, P. (2019). Bottom-up synthetic biology: reconstitution in space and time. **Current opinion in biotechnology**, 60:179–187. (**First Author**)

Summary

Bottom-up reconstituting well-characterized functional molecular entities, parts and modules towards a synthetic cell will give new insights into the general mechanisms and molecular origins of life. However, a remaining central challenge is how to organize cellular processes spatiotemporally from their component parts *in vitro*.

To this end, we developed a 4D regulation toolbox to facilitate a bottom-up reconstitution in both time and space. The spatiotemporal regulation of the 4D toolbox covers the aspects from dynamic gene transcription & translation, reversible protein interaction, spatially protein positioning, sequential protein assembly, extends to defining geometrical membrane boundaries and mimicking cellular anisotropic microenvironment.

Firstly, we developed a thermo-genetic regulation toolbox based on synthetic RNA thermometers, for temporally controlling protein expression *in vitro*. We validated RNA thermometers from *in vivo* to *in vitro* and tuned RNA thermometers through utilizing cell free protein synthesis system. Then we generated the thermo-sensitive protocell by encapsulating thermo-regulated transcription and translation machine in water-in-oil droplets. With the temperature sensing devices, the protocells can be operated with logic AND gates, differentially processing temperature stimuli into biological signals.

Secondly, we engineered the PhyB-PIF6 system to spatiotemporally target proteins by light onto model membranes and thus sequentially guide protein pattern formation and structural assembly *in vitro* from the bottom up. We show that complex micrometer-sized protein patterns can be printed on timescales of seconds. Moreover, when printing self-assembling proteins such as the

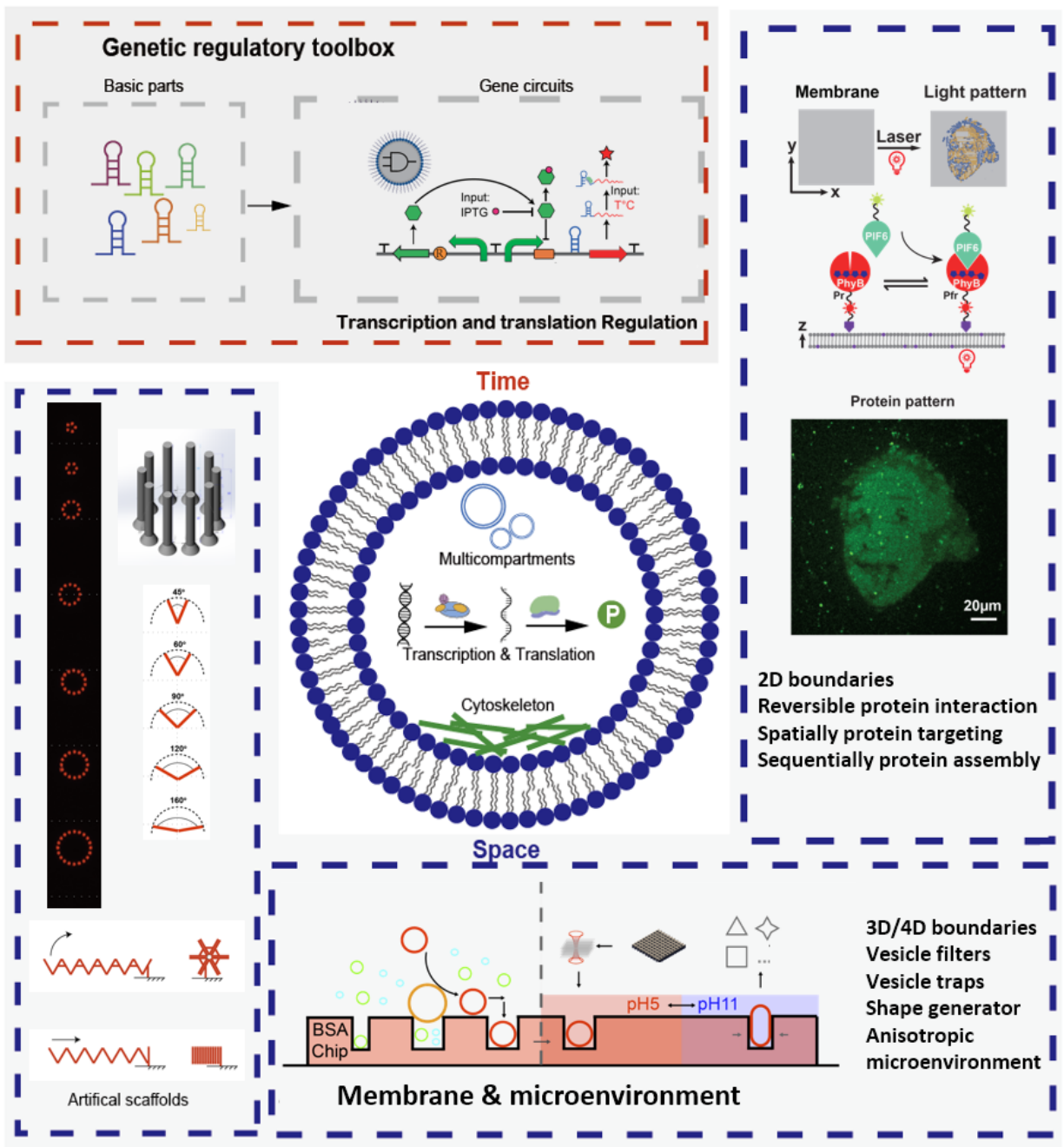
bacterial cytoskeleton protein FtsZ, the targeted assembly into filaments and large-scale structures such as artificial rings can be accomplished.

To develop an artificial anisotropic membrane environment, we introduced a 3D printed protein hydrogel device to induce pH-stimulated reversible shape changes in trapped vesicles. Deformations towards unusual quadratic or triangular shapes can be accomplished. Mechanical force induced by the cages to phase-separated membrane vesicles can lead to spontaneous shape deformations. Moreover, the shape-tunable vesicle provides a spatially well-defined microenvironment for reconstituting shape-dependent protein systems, such as reaction-diffusion system that request explicitly non-spherical geometries.

By taking advantages of the 3D printed hydrogel, we programmably engineered contractible scaffolds for actin-myosin motor reconstitution in 3D space. Nanoscale actomyosin motor as a bio-actuator could generate, transmit active contraction and then drive large-scale shape-morphing of complex 3D hydrogel scaffolds.

In summary, by developing the spatiotemporal toolbox, this thesis introduces a promising step towards establishing bottom-up reconstitution in space and time, which could also guide future efforts in hierarchically building up the next level of complexity towards a minimal cell.

4D TOOLBOX



Schematic overview of 4D regulation toolbox



1 Introduction

The material in the introduction section draws heavily on the author's previously published literature review, “Jia, H., Schwille, P. (2019). Bottom-up synthetic biology: reconstitution in space and time. *Current opinion in biotechnology*, 60:179–187.”.

Source online: <https://doi.org/10.1016/j.copbio.2019.05.008>

Reprinted with permission have been granted by the publisher.

Bottom-up reconstituting well-characterized functional molecular entities, parts and modules towards a synthetic cell will give new insights into the mechanisms and origin of life. However, a remaining central challenge is how to organize cellular processes spatiotemporally from their component parts *in vitro*. To archive the end towards a fully functional synthetic cell, cutting edge tools and technologies have been developed to facilitate such a bottom-up reconstitution in space and time, particularly with regard to the following aspects:

- (1) Reliable model membrane- and microenvironments;
- (2) Dynamic genetic regulation and self-sustaining transcription and translation machinery;
- (3) Spatial organized cytoskeleton that supports the biological architecture and cellular self-reproduction in space.

1.1 The prospect of building a synthetic cell

The hierarchical order of cellular structures and processes arises from the self-assembly and self-organization of mutually interdependent species of molecules, molecular complexes, and supramolecular entities in space and time. Molecular and cell biology has made tremendous progress in characterizing the various components and compartments of the cell independently; however, the remaining central challenge is to understand how cellular processes can generally emerge by spatiotemporal organization from such a variety of components. *In vivo*, many cellular factors co-affect these spatiotemporal dynamics by modifying spatial structures, such as cell size and shape, membrane surfaces, cytoskeleton networks, scaffolding proteins, and the location of intracellular organelles. Moreover, the redundancy and complexity of molecular function elements seriously limits the dissection of cellular networks.

To approach a holistic understanding of biological processes, a promising strategy is the abstraction from full cellular complexity, in favor of the definition of a minimal system that could reproduce in essence the same functionality. This systematic reconstitution of cellular functions module by module is called bottom-up synthetic biology. Through recombining these well-characterized functional molecular entities, parts and modules towards a synthetic cell, one ideally also gains new insights into the general mechanisms and molecular origins of life as a whole. Successful examples of functional bottom-up reconstitution comprise various cytoskeletal, molecular motors, and membrane trafficking systems. In order to accomplish large-scale biomimetic behavior and realize the vision of a fully functional synthetic cell beyond the molecular or subcellular scale, a large number of cutting-edge tools or technologies, like cell free protein synthesis technology, genetic regulation, micro- and nano-packaging, micropatterning technology, DNA/RNA nanotechnology, microfabrication and microfluidic technology, have been developed or favorably employed to this end. In this section, we will focus on summarizing these advanced approaches that, in principle, facilitate the bottom-up reconstitution in time and space, with particular focus on the following aspects: cell membrane and microenvironments, transcription/translation, as well as cytoskeleton organization and cell division (Figure 1).

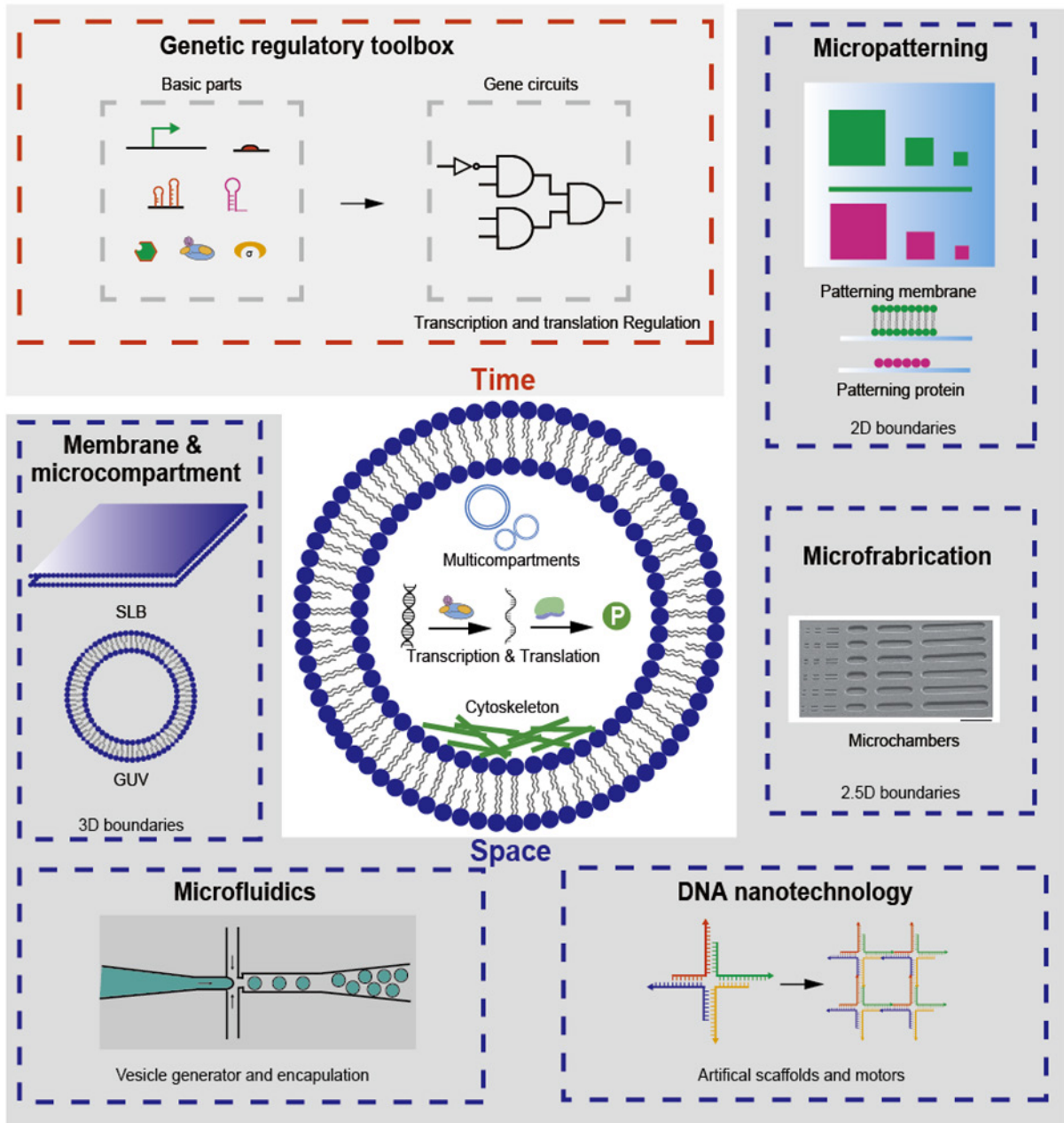


Figure 1. Schematic overview of the multiple aspects, tools and technologies that facilitate the spatiotemporal assembly of functional modules and parts towards a synthetic cell from the bottom up, as discussed in this article.

1.2 Membranes and microenvironments

Phospholipid membranes act as a boundaries and interfaces between the cells and their environments, maintain stable inner microenvironments with distinct compositions and functions, control the exchange of substances between the inside and the outside, template the cytoskeleton to provide distinct cell shapes and shape transformations, and harbor the many protein machineries that help carrying out all of these functionalities efficiently. Similar to the natural cell, membranes usually represent the most basic compartmentation units for synthetic cells.

To create cell-like microenvironments, plasma membranes are mimicked by more or less heterogeneous assemblies of synthetic or natural lipids. So far, diverse model membranes have been developed and tuned with respect to composition, asymmetry, structure and other mechanical properties¹. For different aspects of spatial control, model membranes with different dimensionalities were constructed, ranging from two-dimensional supported lipid bilayers (SLBs) to three-dimensional giant unilamellar vesicles (GUVs)(Figure 2).

1.2.1 2D model membrane

Solid supported lipid bilayers, featuring many properties of biological membranes, but with a simplified and well-controlled topology, have recently received great interest in bottom-up synthetic biology in spite of their technical limitations. The SLBs are stable and particularly well accessible to surface probe techniques; however, the static support limits their application with regard to all machineries that induce membrane transformation. In order to customize them for proteins that sense geometry or particular cues, such as membrane composition or specific receptors the substrate surfaces need to be functionalized. This can be done by directly patterning membrane or proteins on the surfaces with high spatial precision. For spatially confining two-dimensional membrane structures, micro-structured layers of gold can be deposited on glass substrates, to create flat membranes of defined dimensions and geometries on the non-coated area². Such patterned membranes enable the definition of well-defined 2D membrane boundaries; however, because of the much larger scale of the patterned membrane patches compared to the scale of lipids or proteins, it is not suitable for applications that require specific molecular control. To accomplish protein localization on membrane with spatial accuracy on the single molecule

level, light based optochemical and optogenetic tools have thus been utilized to regulate protein properties and functions spatiotemporally. The attractiveness of these approaches are particularly their specificity, ease of use, and the high application precision of light. The tools, such as light-inducible chemically modified phospholipid anchors³ or photoactivatable chemical dimerization⁴, can be made biorthogonal for protein targeting on membrane. Compared with synthetic chemicals introduced to the biological system, optogenetic tools based on proteins in the visible spectral range are comparably specific, while more biologically compatible and reversibly applicable. Because of their low phototoxicity, protein based optogenetic tools are thus very promising in physiologically relevant studies. Diverse light-inducible protein interaction pairs were developed for controlling protein binding to membranes *in vivo*. Recently, the engineered LOV proteins (iLID and Nano) have been applied to pattern proteins on GUVs; however, they have been operated monodirectionally, that is, controlled by just one wavelength, and spontaneously switch off in the dark⁵. Therefore, validating the tunable and reversible optogenetic tools *in vitro* are still under quest.

With these patterning tools in hands, the boundaries of supported lipid membrane can be defined precisely and proteins can be localized spatially well-defined; however, due to neglect of information in Z axis, such a 2D supported membrane cannot implement the structural complexity of a real 3D cell microenvironment.

1.2.2 2.5D and 3D model membrane

For better mimicking the 3D features of cells, with respect to their particular shapes and scales, polydimethylsiloxane (PDMS) as soft polymer support can be templated with various topologies using microfabrication⁶. Microfabricated chambers functionalized by model membranes were developed as reaction compartments with restricted sample volumes (Figure 2). The microfabricated compartments are more closely resembling the rod-like shapes of, e.g., *E.coli*, and thus provide a better environment for reconstituting volume-dependent functions of proteins of that organism⁷⁻⁸. However, regardless of whether glass, mica or PDMS are used to support a membrane, they all face the problem that a such defined model membrane is non-contractible and the compartments are usually not fully closed. To overcome these limitations, spherical and closed giant vesicles (liposomes) were created from cholesterol and natural non-toxic phospholipids.

Other concepts for building closed 3D compartments involve water droplets in oil phase, colloidal particles (colloidosomes), fatty acid vesicles, amphiphilic block copolymers (polyomersomes) and protein-lipid-systems (proteoliposomes)⁹. Liposomes can be produced in bulk in different ways, like hydration, electroporation, extrusion, and solvent evaporation methods.

Unfortunately, these bulk techniques offer a low degree of control, producing, e.g. liposomes with a large size range, typically low efficiency of encapsulation, and are sometimes incompatible with specific cellular modules¹⁰. Recently, microfluidic technologies were thus employed, which dramatically improve encapsulation efficiency and homogenize the size range by generating and manipulating droplets and liposomes with high throughput on chip¹¹. Microfluidic devices were also used for implementing mechanical division of cell-sized liposomes¹²; controlling liposome fusion, trapping¹³, real-time analysis, sorting¹⁴ and pico-injection of substrates into vesicles through the application of short electric pulses¹⁵.

Due to their high reproducibility, automation, and manifold of different manipulation features, microfluidic technologies provide a powerful toolkit for the bottom up reconstitution of biological systems in space and time. However, to yield an even higher precision of control on smaller spatial scales, DNA nanotechnology has recently been employed to develop fully new generations of artificial tools, mimicking natural objects that are otherwise hard to obtain *in vitro* at the nanometer scale. Prominent examples are DNA origami templates for controlling liposomes size¹⁶; DNA nano-poles mediating substrates exchange¹⁷⁻¹⁸, DNA scaffolds for membrane sculpting¹⁹⁻²⁰, functionalized DNA-based membrane anchors²¹, DNA-programmed membrane adhesion²², fusion²³ and liposome self-assembly. Such artificial DNA nano-devices will provide the synthetic cell with programmable parts through which preexisting biological components can be controlled to mimic natural components. Spherical vesicles are attractive starting points for constructing minimal living cells from the bottom-up. However, their spherical shape renders them rather inappropriate to study phenomena that are based on distinct cell shape and polarity, such as cell division. So far, several methods to template membrane vesicles and induce anisotropic structure *in vitro* have been developed, like microfluidics¹³, micropipette aspiration, optical tweezers, and dielectrophoretic field cages²⁴. However, most of them require sophisticated technology or are unable to dynamically control the membrane geometry in a well-defined, i.e., precise and

programmable, manner. On the other hand, cell biology-derived tools like 2D micro-patterning²⁵ and 3D soft lithography of hydrogel²⁶ have been successfully applied to control interfacial geometry in order to define the extracellular environment. Since the development of 3D printing technology, rationally designed 3D objects can be produced from various materials on different scales. In future, 3D printed microniches or molds with smart materials would provide a proper way for rationally shaping vesicle and mimicking the dynamic native cell matrix, allowing us to create a spatially well-defined microenvironment.

In cell biology, compartmentalization and organelle formation represent another level of spatiotemporal regulation. By separating and confining particular reaction volumes, the diffusion of the enzymes and substrates are limited, and thus, their efficiency can be optimized to promote specific enzymatic reactions even at low overall concentrations. Meantime, the reactions can be separated from each other, product can be dissipated and inhibitors kept away. Thus, in order to engineer a synthetic cell, uncoupling enzymatic reactions is an invaluable requirement for constructing higher-order functions in space. To address this aspect, synthetic multicompartments vesicles were generated by surfactant-assisted microfluidic strategies²⁷. Concentric and/or pericentric monodisperse multi-compartments can be prepared at controlled sizes by assembling them hierarchically. Uniform multi-compartments result from de-wetting of double emulsion templates in a multi-step procedure²⁸. Light-triggered enzymatic reactions have already been assembled in nested multi-compartment vesicles, which as reactors show promising application from bio-catalysis through to drug delivery²⁹. Recently, photosynthetic artificial organelles were built in a proto-cellular system to mimic “chloroplasts”, in order to create a self-sustaining synthetic cell that provides an energy source and means of directing intra-vesicular reactions³⁰. Instead of membrane organelles, synthetic membrane-less organelles were generated by fluid phase separation with intrinsically disordered protein domains, suggesting promising applications for packaging collections of proteins in engineered cells and protocells³¹.

Such reproducibly engineered membrane systems provide stable inner microenvironments and basic spatial architectures, laying the technological foundation of building a synthetic cell from the bottom up. In order to build a fully active cellular system, two essential factors need be considered: (1) a dynamic genetic regulation, i.e., a self-sustaining transcription and translation

machinery; (2) a spatially organized cytoskeleton that mechanically supports the biological architecture and enables cellular self-reproduction in space.

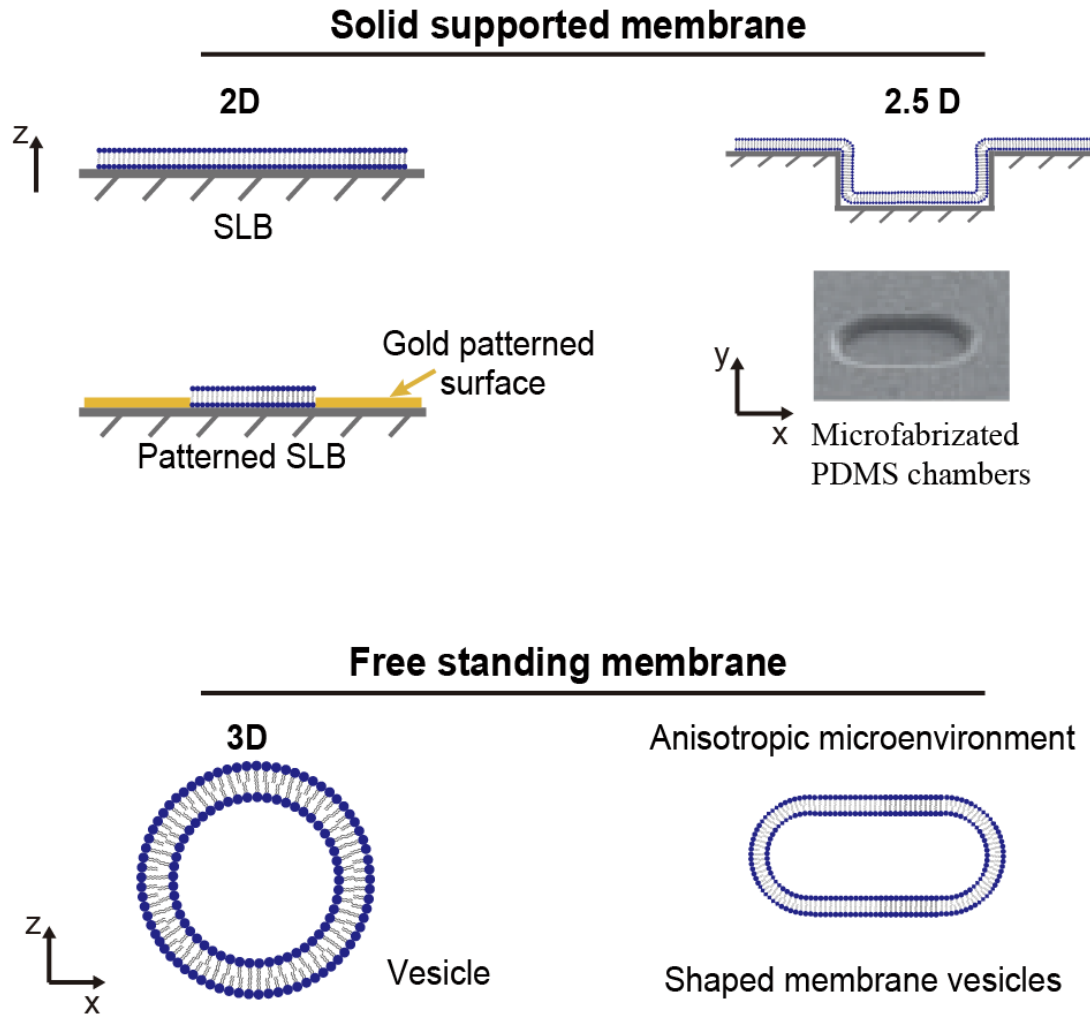


Figure 2. 2D and 3D model membranes defined microenvironments in different dimensions.

1.3 Cell free transcription-translation machinery

In nature, cells can respond to external stimuli and self-regulate homeostasis by the conversion of DNA to RNA (transcription), then to protein (translation), thereby orchestrating diverse

cellular processes at distinct time points, in which the various biological components are involved, in particular: the genome, the transcription-translation machinery, and sensory/signal transduction modules.

1.3.1 Transcription and translation regulation tools

In vitro, various cell free protein synthesis (CFPS) systems have been implemented as a transcription-translation platform for genetic regulation tools that allow dynamic control of protein production and function *in vitro*. CFPS systems harness the core transcription and translation machinery from a living organism source, via either purified biomolecules or crude cell lysates. The advances in CFPS are reviewed elsewhere³². In order to supplement the regulation for CFPS as *in vivo*, *E. coli* sigma factors, different RNA polymerases (T7, SP6 and bacterial *E. coli* RNA polymerases), and a set of repressors were adapted and used for controlling CFPS transcription rates³³. In addition to proteins regulators, RNA molecules themselves can provide regulation with respect to transcription (RNA transcriptional attenuators³⁴, toehold switches³⁵) and translation (riboswitches³⁶, RNA thermometers³⁷). Due to their small sizes, structural flexibility, programmability and directly controllability, RNA tools represent an attractive alternative toolbox of regulatory elements for engineering a minimal system *in vitro*.

1.3.2 Cell free genetic circuits

Based on these basic tools, elementary circuit motifs were constructed for a more rational and logic operator-based controlling, e.g. feedback loops^{33 38}, feed-forward loops³⁹ and *in vitro* ring oscillators⁴⁰. Such *in vitro* gene circuits can process logically within the cell free synthetic environment, allowing us to rationally define systems-level behavior over time. Yet, controlling expression of one or only a few proteins, as it is so far possible *in vitro*, cannot achieve the complexity of even a minimal cell, in which thousands of different proteins should be produced and organized hierarchically. In contrast using a top-down approach, minimal genomes can be rationally designed, chemically synthesized and successfully established in living cells⁴¹⁻⁴². Although it has so far not been achieved, it is conceivable to combine a minimal genome and CFPS to arrive at a fully active synthetic cell in the future. To reach this highly ambitious long-term goal of a synthetic cell, relying on the time-dependent genetic regulations only, without engineering their spatial topology, seem not to be sufficient.

1.3.3 Compartmentalized cell free system towards a synthetic cell

In cells, the spatial organization of the transcription-translation machinery can additionally rely on the modulations of diffusion in crowded and small-volume microenvironments. To mimic such small and crowded environments, CFPS was encapsulated into cell-sized microcompartments. The transcription and translation efficiency can be enhanced by such a micro-compartmentalization, due to more frequent collisions of the functional elements, while the crowded environment may limit the diffusion rates⁴³; in fact, the encapsulated CFPS appears to show stochastic behavior. The gene expression noise in the crowded environment could be quantified using high throughput droplet microfluidics, enabling us to take into account the influence of stochasticity when reconstituting CFPS in a picoliter volume environment⁴⁴.

Self-sustainment represents an essential property of an autonomous living cell, which again relies crucially on the spatial self-organization within cell or with environment. DNA replication and the production of sufficient amounts of functional proteins for the daughter cells are the key requirements to sustain the cell cycle. In a recent effort towards a synthetic minimal cell, the DNA replication machinery of the $\Phi 29$ virus was reconstituted in a cell-free gene expression system. The self-replicated genetic information could encode specific proteins in liposome-based synthetic cells, providing the chassis for evolving functions in a prospective synthetic cell⁴⁵. Metabolism, i.e., substrate cycling between the cell and its environment, needs to provide the required energy and building blocks in order to sustain the three- and four dimensional self-assembly and self-organization of cellular structures and dynamics. Up to now, different functional metabolic pathways have been rebuilt in CFPS (reviewed elsewhere⁴⁶). In the presence of membrane nanopores⁴⁷, either natural transporters or artificial pores, new substrates can pass the membrane, feed and sustain a long-term biological process *in vitro*. In such self-renewing systems, it is possible to engineer genetic circuit interactions within and even between synthetic minimal cells⁴⁸. Via exchanging the quorum sensing signals, chemical communication and unidirectional signaling pathways can be processed between protocell-protocell, even protocell-cell⁴⁹⁻⁵¹. Through electrostatic binding based interaction, the predatory behavior was investigated in synthetic protocell communities⁵². Mediating with micro-pores, molecules transfer, artificial signaling and differentiation processes were demonstrated for realizing spatiotemporal dynamics in artificial multicellular systems⁵³⁻⁵⁴. Another virtue of living cells and minimal cell models is their capacity

to responding to external stimuli and self-regulation of homeostasis³², which is crucial for surviving adverse and fluctuating environment. So far, however, few experimental examples achieved protocells that could convert environmental stimuli, such as heat, into biological signals.

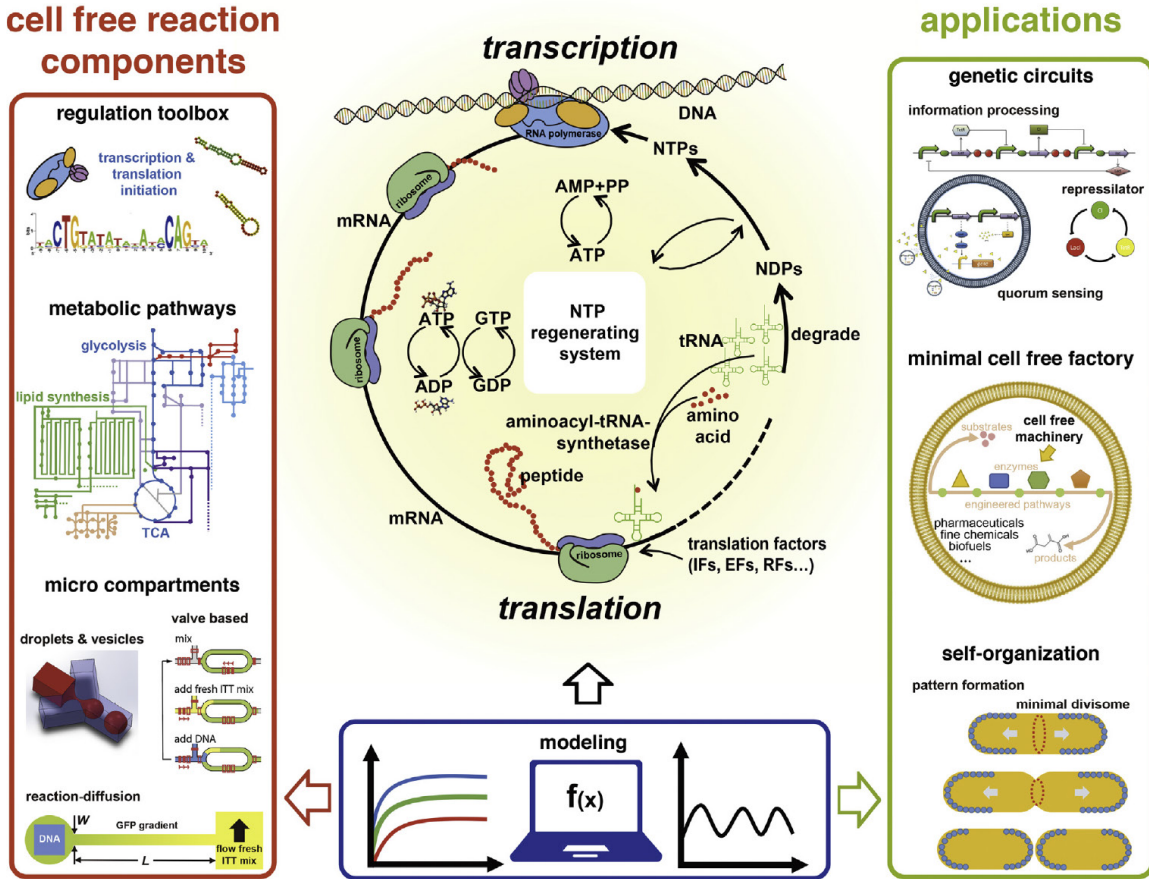


Figure 3. Cell free protein synthesis (CFPS) components and their application in minimal cell models. CFPS contain a core transcription/translation machinery that can interface with a large range of genetic tools and regulatory elements to control and program protein production. New metabolic pathways can increase the productivity of the CFPS, thereby mimicking the high protein production efficiency of a cellular system. In addition, deletion or repression of unrelated metabolic pathways can further increase efficiency by funneling energy consumption into protein expression. Generating micro-compartments with microfluidic devices has pushed CFPS towards ultra-high throughput applications. Accurate computational modeling of the various functional bio bricks will help to improve their robustness, utility and assist in their integration. Collectively, these methods can be used to construct model systems to investigate in depth genetic circuits or fundamental aspects of self-organization that are difficult to investigate *in vivo*, and ultimately

facilitate engineering of artificial cell factories.

1.4 Cytoskeleton for spatial control and support

In vitro, model membranes can be precisely shaped in two and three dimensions in different ways, as described above. In biological cells, their shape is usually inferred by protein assemblies outside (as often the case for bacteria) or inside of the membrane. These internal structures of mostly eukaryotic cells are consequently called cytoskeleton, and built up by several species of filament-forming proteins. Their self-organization in space and time does not only form static support and maintains a certain cellular shape, but also plays indispensable roles in many active processes, like intracellular cargo delivery, cell division, and cell movement. To accomplish these functions, the cytoskeleton must be permanently restructured, based on the activity of a multitude of cytoplasmic proteins. So far, many minimal building blocks of both prokaryotic and eukaryotic cytoskeletons have been identified, abstracted and reconstituted functionally *in vitro*. For the bacterial cytoskeleton, the cell division-related cytoskeletal tubulin homolog protein, FtsZ, was reconstituted onto model membrane through the actin-related protein FtsA or artificial membrane anchors. It has been shown to self-organize into complex patterns, such as fast-moving filament bundles and chirally rotating rings⁵⁵⁻⁵⁶. Additionally, its spatial modulators, the oscillating Min CDE system, were reconstituted into self-organizing waves and oscillations, which act as spatial cues to dynamically control the positioning of FtsZ networks *in vitro*⁵⁷. Intriguingly, the Min system has recently been shown to act as a generic cue for spatially regulating completely unrelated membrane proteins, far beyond FtsZ and other divisome components. It thus opens up exciting perspectives for organizing reaction networks, but also non-bacterial cytoskeleton elements, into defined patterns and gradients on membranes⁵⁸.

To mimic cortical actin present in eukaryotic cells, a minimal system consisting of filamentous actin (F-actin) and myosin-II motors was reconstituted on the SLBs⁵⁹. Together with the synthetic myofilaments formed from the actin motor myosin-II *in vitro*, force can be generated upon ATP addition, leading to rapid actomyosin contractions in the form of asters that are able to introduce changes in the membrane lateral structure⁵⁹. To control the dynamics of the actin cortices, other actin-associated proteins were introduced into the minimal system, e.g. anchor proteins, nucleation factors, elongation factors, stabilizing cap protein and signaling factors.

The mechanisms underlying these minimal cytoskeleton systems can be quantitatively elucidated by biochemical reconstitution of the network assembly and remodeling, in bulk solution or within biomimetic devices. It can be investigated how geometrical boundaries affect the dynamic self-organization and contractions of the highly ordered network^{2,60}. The minimal FtsZ cell division system and its spatial cues have been reconstituted within patterned membranes featuring artificial space boundaries, like 2D patterned membrane² or 2.5D PDMS-supported microchambers⁸. To emphasize the polarity of actin networks, micropatterning technologies were employed to spatially control the nucleation of actin filament architecture in certain geometries with two dimensions⁶⁰ and investigate the force generation⁶¹⁻⁶². Through both, micropatterning of actin nucleation factors and biochemical control of actin filament polymerization, it becomes possible to reconstitute the assembly of complex branched actin architectures in 3D⁶³.

2D DNA origami scaffolds were also used to precisely pattern myosin and systematically dissect the role of motor-motor interactions in the collective behavior⁶⁴. As classical micropatterning is limited to two-dimensional surfaces, 3D devices, like microfabricated chambers⁶⁵, microfluidics chips⁶⁶, water-in-oil droplets⁶⁷ and cell-sized liposomes⁶⁸⁻⁶⁹ were used to mimic cell size, shape and microenvironment in 3D. Artificial cytoskeletons with diverse programmable features were created by DNA nanotechnology. For example, a Y-shaped DNA cytoskeleton can form a dense network structure in the gel phase, which can be used as artificial cytoskeleton for stabilizing liposomes⁷⁰. Even synthetic nucleic acid walkers⁷¹⁻⁷² were engineered for long-term tunable cargo transportation in space. Myosin-patterned DNA nanotube rings were created for engineering circular gliding of actin filaments⁷³. Artificial myosin filaments were functionalized with DNA nanotube scaffolds to enable large-scale movement and force generation, representing the first step towards reconstituting muscle activity⁷⁴.

Last but not least, division is one of the most obvious and distinctive features of living cells. In modern cells, large protein machineries are devoted to the spatial organization and orchestration of the division process. In order to approach synthetic cell division, a minimal *E. coli* divisome based on FtsZ and some of its regulators was encapsulated into the lipid vesicles, to particularly attempt the induction of membrane deformation, with the final goal of budding or fission. FtsZ with either natural or artificial membrane anchors has been found to form curved filaments or proto-rings inside or outside liposomes, which can deform soft giant vesicle membranes

reminiscent of the induction of Z-ring constriction, resulting in concave depressions, convex bulges, of membrane tubulation ⁷⁵. Although some liposomes have apparently even undergone fission based on FtsZ activity, quantification of results has been difficult because of the low reproducibility of well-defined Z rings assembled within liposomes. Even though Z-rings can definitely form inside liposomes, their localizations were so far randomly distributed, due to their highly dynamic properties, and their sizes too small to induce large-scale spatial modulations of giant vesicles.

Likewise, the reconstituted actomyosin cortices could generate tension and drive shape changes of cell-sized liposomes ⁷⁶. Actomyosin was reconstituted as a contractile ring inside the cell sized liposome, but without membrane deformation activity reported ⁶⁹. Although in some cases, the membrane has been shown to be deformed by a cytoskeleton mimicry, it still remains a grand challenge to fully reconstitute an active division machinery *in vitro* that can mediate a mother cell to spontaneously or controllably divide into two daughter cells. Due to the sophisticated spatiotemporal regulation of the cell division process in nature, it will be one the key challenges for bottom-up synthetic biology to actually define and bring together a simplified set of functional modules to accomplish this task. Recently, by help of microfluidic pico-injection technology, purified transmembrane and cytoskeleton proteins could be sequentially loaded in stabilized GUVs, which shows great promise at least for the efficient assembly of functional parts in suitable compartments ¹⁵.

1.5 Objective of this thesis

The bottom-up reconstitution of functional parts towards a minimal living system is a great challenge of modern synthetic biology, which will likely persist for many more years to come, but deliver not only fully new insights into the fundamental properties of life, but also into many still hidden or insufficiently understood cellular mechanisms. Of particular interest is the hierarchical assembly and spatiotemporal connection between the many fundamental parts that have already been, or await to be, identified and successfully reconstituted in simplified environments.

Ideally, genetic parts and circuits provide a temporal regulation for the biological processes *in vitro*, either in bulk environment or in crowded microcompartments. Until now, the *in vitro* developed functional parts are still the tip of the iceberg, compared with the many different cellular functionalities in nature. Moreover, to render various different tools to function compatibly in the same compartment and to sustain thousands of reactions over extended periods of time are still crucial challenges for any cell-free technology. Another key issue is the efficient regulation of “cells” by their environment, and the respective communication with it. With regard to proper compartmentation, two- and three-dimensional model membrane systems have been shown to maintain stable microenvironments and provide biocompatible spatial boundaries with potentially tunable permeability. Supported by polymers or protein-based coats and filaments, these model membranes can be designed to resemble natural cell membranes in topology and composition, but are still far from active cellular membranes that can regulate their own transformation. Artificial tools enabling cell-shape mimics in 3D and controlling the localization of cytoskeleton elements on a microcompartment are still required to aid the functional reconstitution and the orchestration of individual parts into regulatory networks, in which some reactions serve as spatiotemporal cues for others.

This thesis therefore has distinct objectives to develop the methodological tools and technologies that facilitate a bottom-up reconstitution from different dimensions, both in time and space.

Time:

1) To generate self-sustaining protocells by encapsulating transcription and translation machinery in droplets. To engineer a synthetic genetic regulation toolbox for rationally

controlling transcription and translation in protocells, and enabling protocells logically sense and respond to environment stimuli, such as heat.

Space:

2) To spatiotemporally position and pattern protein on 2D and 3D model membrane and sequentially instruct cytoskeleton protein self-assembly in cell free system, such as *E. coli* cell division primary factor FtsZ.

3) To reversibly shape and program freestanding membrane vesicles in order to mimicking the spatial anisotropic microenvironment. To explore the boundary geometry effect of the shaped vesicles to the membrane dynamics and the molecular reaction-diffusion.

4) To engineer contractible artificial scaffolds with biocompatible soft materials. To reconstitute minimal cytoskeleton, such as actin-myosin system, on the scaffolds for active contraction investigation.

2 Results

This cumulative thesis consists of two published papers and two manuscripts.

Jia, H., Heymann, M., Härtel, T., Kai, L., & Schwille, P. (2019). Temperature-sensitive protein expression in protocells. **Chemical communications**, DOI: 10.1039/c9cc02734c. **(First Author)**

Jia, H., Kai, L., Heymann, M., García-Soriano, D. A., Härtel, T., & Schwille, P. (2018). Light-induced Printing of Protein Structures on Membranes *in vitro*. **Nano letters**, 18(11), 7133-7140. **(First Author)**

Jia, H., Litschel, T., Heymann, M., Eto, H., Franquelim, Henri G., & Schwille, P. Shaping membrane vesicles in 3D-printed protein hydrogel cages, submitted. **(First Author)**

Jia, H., et. al., Active forces driving 4D protein hydrogel origami, in preparation. **(First Author)**

Publications

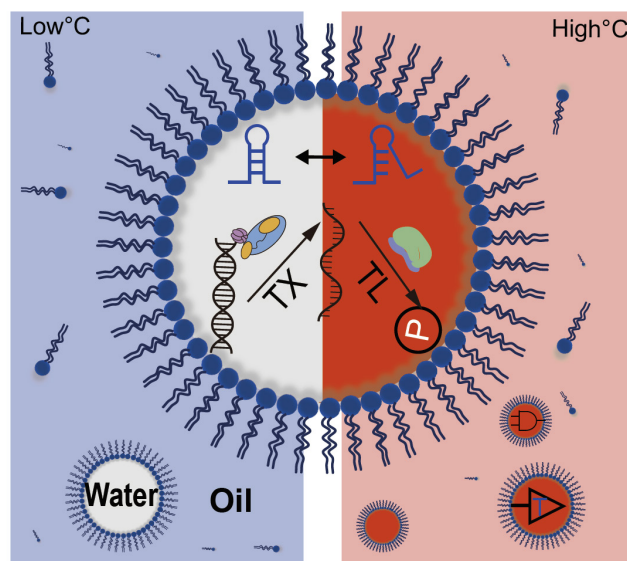
Time dimensional regulation tools:

2.1 Temperature-sensitive protein expression in protocells

In this manuscript, we engineered a synthetic RNA thermometers based temperature regulation toolbox, which enables protocells selectively sense and respond to heat. Based on the logic temperature-sensing genetic devices, the protocells can differentially process temperature stimuli into biological signals. Additionally, with respect to bottom-up reconstitution, temperature dependent differential regulation of protein expression will enable us to establish reaction schemes that require a delicate concentration ratio and dynamic expression in time.

This article is licensed under a Creative Commons Attribution 3.0 Unported Licence.

Source online: DOI: 10.1039/c9cc02734c





Cite this: DOI: 10.1039/c9cc02734c

Received 9th April 2019,
Accepted 10th May 2019

DOI: 10.1039/c9cc02734c

rsc.li/chemcomm

Temperature-sensitive protein expression in protocells†

 Haiyang Jia,^{id} Michael Heymann,^{id} Tobias Härtel,^{id} Lei Kai^{id} and
Petra Schwillie^{id}*

We engineered a synthetic temperature regulation toolbox to enable protocells to sense and respond to heat, utilizing RNA thermometers. The thermo-sensitive protocells were generated by encapsulating temperature feedback transcription/translation machinery in droplets. Based on these temperature-sensing devices, the protocells can be operated with logic AND gates, differentially processing temperature stimuli into biological signals.

The construction of a minimal cell or protocell from the bottom-up may deepen our understanding of the essence of cellular life and its origin on earth.¹ It also offers new avenues for applications in biotechnology, medicine, and environmental engineering.² Recent advances in protocell design also reinvigorated interest and improvements of cell-free protein synthesis (CFPS).³ CFPS reconstitutes the components of the cellular transcription and translation machinery for protein synthesis *de novo*, thus avoiding purification. Encapsulated into emulsion droplets or lipid vesicles, CFPS provides a versatile platform to specifically utilize protein functionality, ultimately paving the way for the construction of complex living systems from the bottom up.⁴ A variety of synthetic biological circuits have been adapted for dynamically controlling transcription and translation of protocells, such as negative/positive feedback loops.^{4,5} These have been used to regulate different components within a protocell, but also to achieve global communication between protocell communities.^{6–9} Addition of micro-pores, molecule transfer, artificial signalling and differentiation cascades achieved and improved spatiotemporal dynamics in multicellular artificial cell models.^{10,11} However, one key virtue of living cells and minimal cell models is their capacity to selectively respond to external stimuli and to self-regulate homeostasis,¹² which is crucial for surviving adverse and fluctuating environments. With regard to the aspects of resilience and adaptation to the

environment, protocells are still much inferior to the standards of nature. In particular, few experimental studies achieved protocells that could convert physical stimuli, such as heat, into biological signals. In living bacteria, *e.g.*, stress response to heat is essential for effective adaptation to environmental fluctuations.¹³ On the other hand, with regard to biotechnological applications, a temperature-sensitive model system would be ideally poised for efficient control. Thus, implementing a temperature-sensing module for converting temperature stimuli into biological signals would greatly improve the design of protocells, mimicking natural stress responses, or establishing an easy to operate control element. Temperature serves as a well-defined signal that could be used by engineered protocell or bacterial therapeutics to detect and respond to host conditions, or spatially targeted external triggers such as focused ultrasound.¹⁴

Here we describe the engineering of a protocell that can respond to temperature stimuli, using temperature sensitive non-coding RNA sequences that we refer to as RNA thermometers (RNATs). Natural as well as artificial RNATs have been discovered *in vivo*¹⁵ and designed *in vitro*.^{16,17} Most commonly, these RNATs are located in the 5'-untranslated region of the messenger RNA, and fold into secondary structure to control translation by blocking ribosome binding sites (RBS) at low temperature. The RNAT loop unfolds when temperatures exceed a defined threshold, to release the RBS for subsequent gene expression.¹⁸

We designed synthetic RNATs based on a simple RNA-melting mechanism.¹⁹ Accordingly, we implemented a suite of synthetic RNATs to form a single stem-loop structure, which is composed of three elements: a RBS sequence, a complementary anti-RBS (ARBS) sequence and the loop sequence (Fig. 1a). A reporter gene cassette containing a T7 promoter, RNAT, and red fluorescent protein (RFP) was used to validate various constructs (Fig. 1b). Transcription of mRNA was driven by T7 promoter and its translation was subsequently controlled by the RNA thermometer. We selected the well-established RNAT3 thermometer¹⁵ to validate the functionality of our gene cassette using the *in vitro* PURE reaction²⁰ by quantifying RFP fluorescence at 37 °C and 42 °C. At 37 °C, RNAT3 inhibited the

Dept. Cellular and Molecular Biophysics, Max Planck Institute of Biochemistry,
Am Klopferspitz 18, D - 82152 Martinsried, Germany.

E-mail: schwillie@biochem.mpg.de

† Electronic supplementary information (ESI) available. See DOI: 10.1039/c9cc02734c



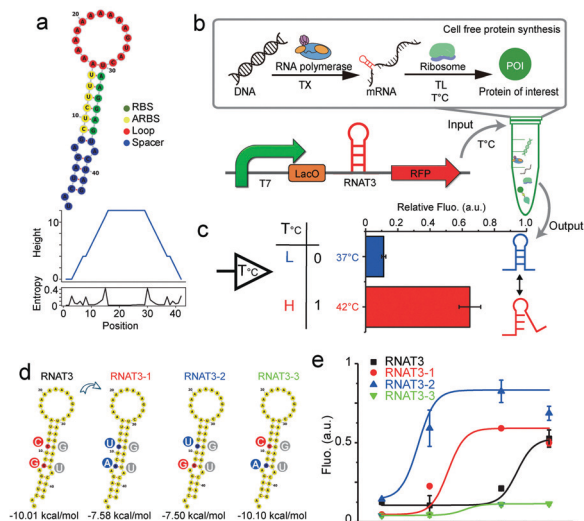


Fig. 1 Validating RNATs for cell free protein synthesis. (a) RNA thermometer and stem loop secondary structure simulated with RNAfold. Bottom: Mountain plot and positional entropy plot of RNAT3, in which the height indicates the number of base pairs enclosing the base at position 0. (b) Scheme of cell free protein synthesis test-tube reaction used to validate RNA thermometer construct. (c) Relative function of RNAT3 was verified by PURE cell free protein synthesis at 37 °C and 42 °C. (d and e) Tuning RNATs in cell free system. (d) Sequence changing and structure simulation of three good candidates after cycling improvement. (e) Functional investigation at different temperatures.

PURE reaction from expressing RFP (“off” state), analogous to previous *in vivo* results.¹⁵ At temperatures of 42 °C, a “jump” in expression could be observed (“on” state). At 42 °C the PURE reaction under RNAT3 regulation yielded 3.3 times higher RFP yields compared to 37 °C. Switching from “off” to “on”, the relative expression ability compared to a control has been increased about sevenfold (Fig. 1c). Ionic strength influences the stability of RNA secondary structure.²¹ The higher Mg^{2+} concentration can stabilize the RNAT3 structure; consequently, inhibit its switching in the PURE system (Fig. S1, ESI†).

We tuned RNATs activation temperatures by utilizing a cell-free transcription/translation system in the test tube (Fig. S2, ESI†). A series of RNATs with different minimum free energies was designed through the RNAfold Web Server and inserted into the reporter gene cassette. New RNATs contained the introduced base pair mismatches into the stem. Their melting temperatures were verified through coupled cell-free transcription and translation at different temperatures, while monitoring RFP synthesis by a fluorescence plate reader assay. By avoiding the need for cell culturing, this screening approach can be at least three days shorter in comparison to conventional *in vivo* approaches. This significantly accelerates the design and validation process.

The screen obtained three excellent candidates derived from the original RNAT3 (Fig. 1d and e). While RNAT3 dehybridized at 40 °C¹⁵, the RNAT3-1 mutant sequence had a threshold temperature of 37 °C, while the final RFP expression yield was unaffected. RNAT3-2 had a transition temperature of 35 °C. The switching behaviour of RNAT3-3 was similar to RNAT3, but with overall reduced expression. Considering the

sequence of the RNATs, since the bond strength of C–G pair is stronger than U–G, mutation from C to U in the mismatch of the RBS region would make the stem-loop easier to open. Therefore, the switching temperature of RNAT3-2 was reduced, while the expression was enhanced. Conversely, the RNAT3-3 mutation of (G to A) stabilized the loop structure, resulting in the lowest observed expression level. RNAT3-1 contained both mutations, thus featured with all the factors of RNAT3, RNAT3-2 and RNAT3-3. Owing to the balance effects of the two sites, RNAT3-1 could maintain similar expression ability with the original RNAT3; meanwhile it switched on at lower temperature and yielded 30% weaker expression level compared with RNAT3-2. This toolbox of different RNATs provides us with a variety of different expression control modules in dependence of temperature (temperature sensors). *In vitro* designed RNATs could also work *in vivo*, and showed similar “on” and “off” manners (Fig. S3, ESI†).

Based on these results, we then prototyped a temperature sensitive protocell model by co-encapsulating the thermometer controlled gene circuits and the PURE transcription/translation machinery in picoliter emulsion droplet compartments (Fig. 2a). Emulsion droplets were formed through mechanical agitation, to disperse the aqueous phase into HFE7500 fluorinated oil with a PFPE-PEG-PFE biocompatible surfactant.²² The resulting micro-emulsion droplets are stable against coalescence for days and can tolerate temperature fluctuations. We encapsulated the RNAT3-1 controlled cell-free protein synthesis system into water-in-oil droplets (Fig. 2b). Protocells programmed with RNAT3 expressed RFP (red) signal at 40 °C, but were insensitive to 35 and 37 °C (Fig. 2d). In turn, RNAT3-1 protocells were activated by lower temperature around 37 °C. Both did not express RFP (“off”) at 35 °C incubation. Thus, consistent with our previous bulk

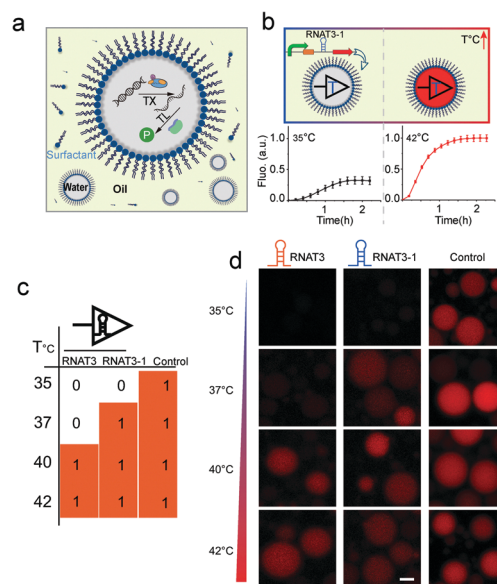


Fig. 2 (a) Scheme of temperature sensitive protocell created by encapsulating transcription/translation machinery into emulsion droplets. (b) Fluorescence intensity of RFP synthesized in thermal protocell at different temperatures. (c and d) Droplet protocell variants with different RNATs can sense and respond to specific temperatures. Scale bar, 20 μ m.



experiments, RNATs laden protocells responded specifically to different temperatures. The results confirm that synthetic RNATs endowed the protocells with the ability to convert ambient temperature into a specific biological response, demonstrating a direct connection between the protocell and environmental temperature cues.

Dynamic logic circuits capable of controlling multiple gene functions at different temperatures are required to further integrate thermal protocell responses with other metabolic cues. Such genetic logic circuits would enable a synthetic cell to initiate different biological functions in a defined workflow to ultimately connect a functional biological network to specific thermal cues *in vitro*. In particular, differential expression of proteins in response to defined environmental settings is an elegant way of titrating intracellular reactions. Towards this goal, we engineered a multiplexed protocell capable of reporting metabolic activity through EGFP fluorescence, while simultaneously reporting temperature through RFP fluorescence. Expression levels of enhanced green fluorescent protein (EGFP) and RFP in picoliter droplets under constitutively active T7 promoters were identical for all investigated temperatures (Fig. S4, ESI[†]). We then combined constitutively active EGFP expression with RFP expression under RNAT3-1 control (Fig. 3b). As expected, only EGFP was detected for low temperature of 35 °C. Although the stretch of DNA transcribed into an RNA molecule, the translation of RFP was blocked by RNAT3-1. When the temperature was shifted to 42 °C (above the 37 °C threshold), co-expression of RFP and EGFP inside of microcompartments was observed (Fig. 3c and Fig. S4, ESI[†]), demonstrating that the thermal genetic multiplexer can

enable the protocells to selectively transform expression of different genes in response to a changing environment.

Controlled microfluidic encapsulation into identically sized protocell droplets was then carried out in order to access response fluctuations. We measured the fluorescence intensity of EGFP (pCoofy1-T7-RBS-EGFP) and RFP (pCoofy1-T7-RNAT3-1-E1010) per droplet for a population of >3000 droplets every 10 min, allowing us to track the behaviour of protocell populations with thermal multiplexer. Intriguingly, in the initial half hour, the protocell population showed almost homogeneous expression for both independent genes, *egfp* and *rfp* (Fig. 3d). Afterwards, the protocell population started to differentiate over time, especially RFP expression noise accumulated over time (Fig. 3d, e and Fig. S5a, ESI[†]). This may be due to stochastic on/off switching of the RNATs that leads to slight differences in expression rates (Fig. S5b, ESI[†]). Such stochasticity is inherent to biochemical gene expression,²³ and may further be amplified through inhomogeneous distributions of materials among different bioreactors.^{23,24} The long-time moderate heat stress (42 °C) may reduce the maturation rate and decrease fluorescence,²⁵ which may also be reason of the overtime change.

In a next step, we extended our protocell expression control architecture to implement a temperature sensitive AND gate, enabling protocells sensing both chemical and thermal signals (Fig. 4). Different published logic gates have been implanted as gene circuits.^{26,27} We design our thermo-responsive AND gate to function on both, the transcription and translation level (Fig. 4a). The AND gate utilized chemical inducer and temperature as the two independent inputs. A T7 promoter with a lac operon as regulator was used to control transcription of the RFP, to respond to the chemical inducer (IPTG). LacI repressor was constitutively controlled by another T7 promoter (without lac operon). Therefore, the transcription was kept off in the absence of IPTG. IPTG mediated inhibition of the LacI repressor in turn activated mRNA synthesis. After mRNA expression, our RNA thermometer inhibits

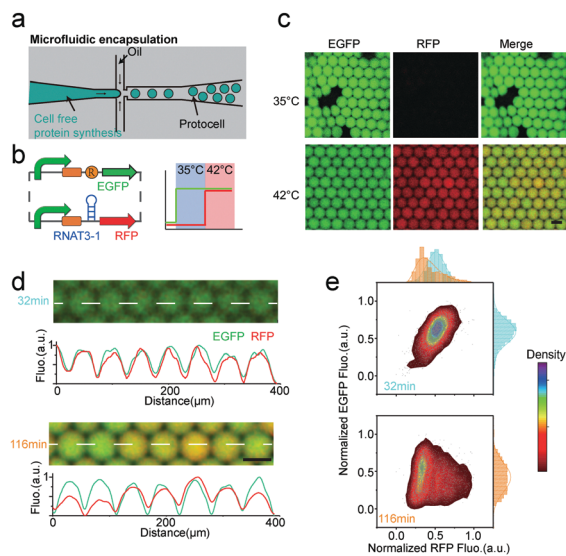


Fig. 3 Thermal-controlled multiplexer. (a) Droplet microfluidics used to create protocells of identical size. (b) Design of the thermal-gene circuit and the expected multiplexed thermal activation at different temperature. (c) Representative images of thermal-multiplexer controlled protocell at 35 and 42 °C. Scale bar, 50 μ m. (d) Microscopy images and intensity line plots of droplets expressing slightly different amounts of EGFP and RFP. Scale bar, 50 μ m. The white dash line in the micrographs indicate the position of measured curves. (e) Normalized EGFP versus normalized RFP intensities of the whole population of droplets.

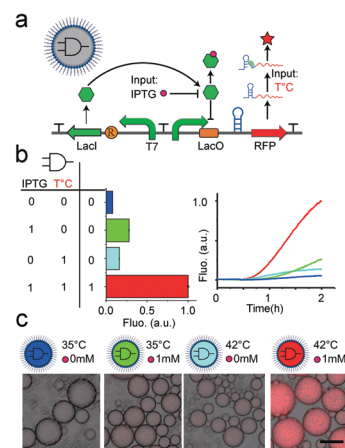


Fig. 4 Thermal mini-logic AND gate. (a) Illustration shows the design of AND gate circuit. (b) Truth table and the output (RFP signal) of the thermal mini-logic AND gate. Right: Time course curve of the AND gate outputs in buck reaction. (c) The images show the thermal mini-logic AND gated protocell preformed with different behaviours according to the truth table, scale bar, 50 μ m.



translation at low temperature. This combined transcriptional and translational based AND gate could produce different reporter outputs according to different input combinations: the two input signals temperature and IPTG (Fig. 4b). We validated the function of this circuit in a bulk assay in test tube. Compared with the highest background, the expression was increased about fourfold (Fig. 4b). We then encapsulated the mini-AND into our water-in-oil emulsion droplets to generate protocells that can integrate the different signals. The compartmentalized protocells can perform logic as well as the AND gate in the bulk reaction, by responding to the chemical environment and temperature (Fig. 4c). This minimal AND gate only required one inducible promoter, one constitutive promoter, one repressor and one RNA thermometer. Compared with other transcription based genetic AND gates,²⁸ our approach reduced the amount of required gene parts by half. The mini-AND gates would thus be more flexible for the application of protocell engineering.

Artificial cells or protocells, which can be built by top-down or bottom-up methods, have attracted much attention as substitutes for natural cells mimicking some of their essential properties. However, despite the impressive progress to date, there is still a wide gap between artificial cells and biological cells. To fill this gap, several issues remain to be solved. A key issue is the efficient regulation of “cells” by their environment, and the respective communication with it.² Our study addressed this problem by developing a synthetic temperature feedback regulation toolbox to render protocells responsive to heat. We validated our RNA thermometer *in vitro* and developed an *in vitro* strategy for tuning the thermal response rapidly and simply. As a translation level regulator, RNA thermometers can minimize the transcriptional redundancy of the genetic circuits to make them easier to be implanted in a minimal cell model.

We generated protocells from the bottom-up by encapsulating a temperature feedback transcription/translation machinery into picoliter emulsion droplets. With these temperature sensitive devices, the protocells can process different inputs in a deterministic way. We demonstrated a thermally driven gene multiplexer and a logic AND gate, capable of processing both thermal and chemical signals. Such tunable temperature sensitive protocells will enable a variety of applications in biotechnology, medicine, and industry. For example, by their ability to detect temperature changes, respectively optimized medical protocells may at some point replace microbial therapy as a much safer way to produce and deliver pharmaceuticals by sensing the fever of host. Alternatively, drug synthesis and release from protocells may be controlled by focused ultrasound heating, potentially targeting drugs directly to the specific sites in the host. With respect to fundamental research, temperature dependent differential regulation of protein expression, as shown here, will enable us to establish reaction schemes that require a delicate concentration ratio, such as the self-organization of MinDE proteins,²⁹ in cell free expression schemes. Undoubtedly, further development of environment sensitive logics as shown here within artificial cells or protocells will bring attractive opportunities to many fields.

This research has been supported by the GRK2062 funded by Deutsche Forschungsgemeinschaft (DFG); and MaxSynBio consortium funded by the Federal Ministry of Education and Research of Germany and the Max Planck Society.

Open Access funding provided by the Max Planck Society.

Conflicts of interest

There are no conflicts to declare.

References

- P. Schwillie and S. Diez, *Crit. Rev. Biochem. Mol. Biol.*, 2009, **44**, 223–242.
- C. Xu, S. Hu and X. Chen, *Mater. Today*, 2016, **19**, 516–532.
- V. Noireaux, R. Bar-Ziv and A. Libchaber, *Proc. Natl. Acad. Sci. U. S. A.*, 2003, **100**, 12672–12677.
- J. Shin and V. Noireaux, *ACS Synth. Biol.*, 2012, **1**, 29–41.
- H. Niederholtmeyer, Z. Z. Sun, Y. Hori, E. Yeung, A. Verpoorte, R. M. Murray and S. J. Maerkl, *eLife*, 2015, **4**, e09771.
- P. M. Gardner, K. Winzer and B. G. Davis, *Nat. Chem.*, 2009, **1**, 377–383.
- Y. Qiao, M. Li, R. Booth and S. Mann, *Nat. Chem.*, 2017, **9**, 110.
- G. Rampioni, F. D'Angelo, M. Messina, A. Zennaro, Y. Kuruma, D. Tofani, L. Leoni and P. Stano, *Chem. Commun.*, 2018, **54**, 2090–2093.
- T. D. Tang, D. Cecchi, G. Fracasso, D. Accardi, A. Coutable-Pennarun, S. S. Mansy, A. W. Perriman, J. R. Anderson and S. Mann, *ACS Synth. Biol.*, 2017, **7**, 339–346.
- G. Villar, A. D. Graham and H. Bayley, *Science*, 2013, **340**, 48–52.
- A. Dupin and F. C. Simmel, *Nat. Chem.*, 2019, **11**, 32.
- H. Jia, M. Heymann, F. Bernhard, P. Schwillie and L. Kai, *Nat. Biotechnol.*, 2017, **39**, 199–205.
- G. Segal and E. Z. Ron, *Ann. N. Y. Acad. Sci.*, 1998, **851**, 147–151.
- D. I. Piraner, M. H. Abedi, B. A. Moser, A. Lee-Gosselin and M. G. Shapiro, *Nat. Chem. Biol.*, 2017, **13**, 75.
- H. Jia, X. Sun, H. Sun, C. Li, Y. Wang, X. Feng and C. Li, *ACS Synth. Biol.*, 2016, **5**, 312–320.
- S. Sen, D. Apurva, R. Satija, D. Siegal and R. M. Murray, *ACS Synth. Biol.*, 2017, **6**, 1461–1470.
- F. W. Sadler, I. Dodevski and C. A. Sarkar, *ACS Synth. Biol.*, 2017, **7**, 292–296.
- J. Kortmann and F. Narberhaus, *Nat. Rev. Microbiol.*, 2012, **10**, 255–265.
- A. S. Mironov, I. Gusarov, R. Rafikov, L. E. Lopez, K. Shatalin, R. A. Kreneva, D. A. Perumov and E. Nudler, *Cell*, 2002, **111**, 747–756.
- Y. Shimizu, A. Inoue, Y. Tomari, T. Suzuki, T. Yokogawa, K. Nishikawa and T. Ueda, *Nat. Biotechnol.*, 2001, **19**, 751–755.
- D. E. Draper, *RNA*, 2004, **10**, 335–343.
- C. Holtze, A. Rowat, J. Agresti, J. Hutchison, F. Angile, C. Schmitz, S. Köster, H. Duan, K. Humphry and R. Scanga, *Lab Chip*, 2008, **8**, 1632–1639.
- M. B. Elowitz, A. J. Levine, E. D. Siggia and P. S. Swain, *Science*, 2002, **297**, 1183–1186.
- M. M. Hansen, L. H. Meijer, E. Spruijt, R. J. Maas, M. V. Rosquelles, J. Groen, H. A. Heus and W. T. Huck, *Nat. Nanotechnol.*, 2016, **11**, 191.
- K. Deepankumar, S. P. Nadarajan, D.-H. Bae, K.-H. Baek, K.-Y. Choi and H. Yun, *Biotechnol. Bioprocess Eng.*, 2015, **20**, 67–72.
- B. Wang, R. I. Kitney, N. Joly and M. Buck, *Nat. Commun.*, 2011, **2**, 508.
- T. S. Moon, C. Lou, A. Tamsir, B. C. Stanton and C. A. Voigt, *Nature*, 2012, **491**, 249–253.
- J. Bonnet, P. Yin, M. E. Ortiz, P. Subsoontorn and D. Endy, *Science*, 2013, **340**, 599–603.
- P. Glock, B. Ramm, T. Heermann, S. Kretschmer, J. Schweizer, J. Mücksch, G. K. Alagöz and P. Schwillie, *ACS Synth. Biol.*, 2018, **8**, 148–157.



Supporting Material for

Temperature-sensitive protein expression in protocells

Haiyang Jia^a, Michael Heymann^a, Tobias Härtel^a, Lei Kai^a, Petra Schwille^{a*}

^a Dept. Cellular and Molecular Biophysics, Max Planck Institute of Biochemistry, Am Klopferspitz 18, D - 82152 Martinsried, Germany

*Corresponding author: Petra Schwille, schwille@biochem.mpg.de

Methods

Plasmid construction

Plasmid constructions and DNA manipulations were performed as the standard molecular biology techniques. RNAT3-E1010 (E1010: <http://partsregistry.org>) was cloned from the plasmid (pSB1K3-J23119-RNAT3-E1010¹) and was inserted into pCoofy1 vectors (Life Technologies) with Xba-I at the 5' end of the coding sequence (CDS) and a Xho-I restriction site at the 3' end of the CDS. The mutants of RNA Thermometers were constructed with the whole plasmid mutagenesis method². All the plasmid used in the cell free reaction were extracted from *E. coli* (TOP10) with the QIGEN medium plasmid extract kit. The investigation of the RNATs *in vivo* were performed in the *E. coli*(BL21DE3) strain as the reported method¹.

***In vitro* transcription/translation mixture.**

PURExpress® In Vitro Protein Synthesis Kit (NEB) was used in all the cell free reactions. The reactions were performed as 10µl Buffer A, 7.5µl Buffer B, 300ng DNA and the ddH₂O, then incubated at 30°C, 35°C, 37°C, 40°C, 42°C for 2 hours using incubators or Thermomixer C(Eppendorf) and stopped by placing the tube(s) on ice. Then the fluorescence of the reactions were tested by the Infinite M200 PRO plate reader (TECAN). The controls used in the experiment were the black control and the positive control(Pcoofy1-T7-RBS-E1010) All experiments were performed in triplicate, and differences between the mean values were considered as significant at p<0.05 with T-test.

Droplet generation

Droplet produced with 'shaken-not-stirred' method

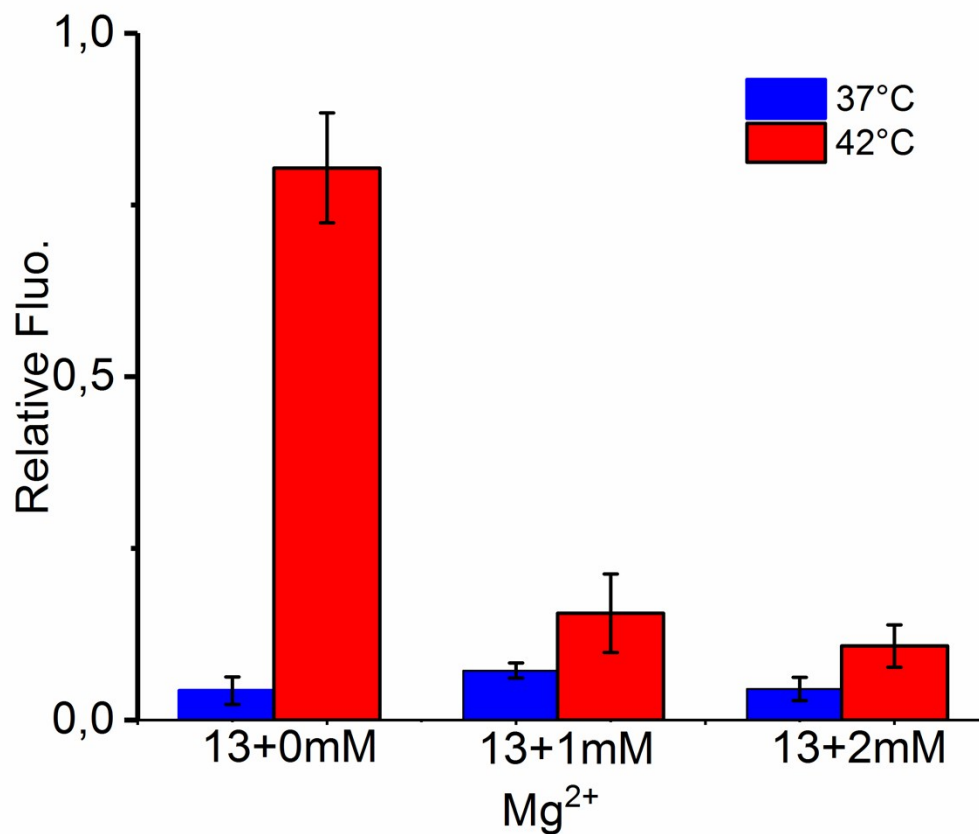
Different radii droplets were generated with the 'shaken-not-stirred' method. We mixed 5 µL cell free transcription/translation reaction mix with 25µL HFE7500 fluorinated oil with 1.8 % (w/w) PFPE-PEG-PFE biocompatible surfactant in PCR tubes (Eppendorf) using a benchtop vortex mixer for 60 s at maximum speed. Then the top droplets were absorbed in the 1.1*0.5mm glass vocabulary and the vocabulary was immobilized onto the glass slide for microscope measurements. This technique offers the possibility to generate a big range of different sized compartments in a very short time.

Microfluidic method

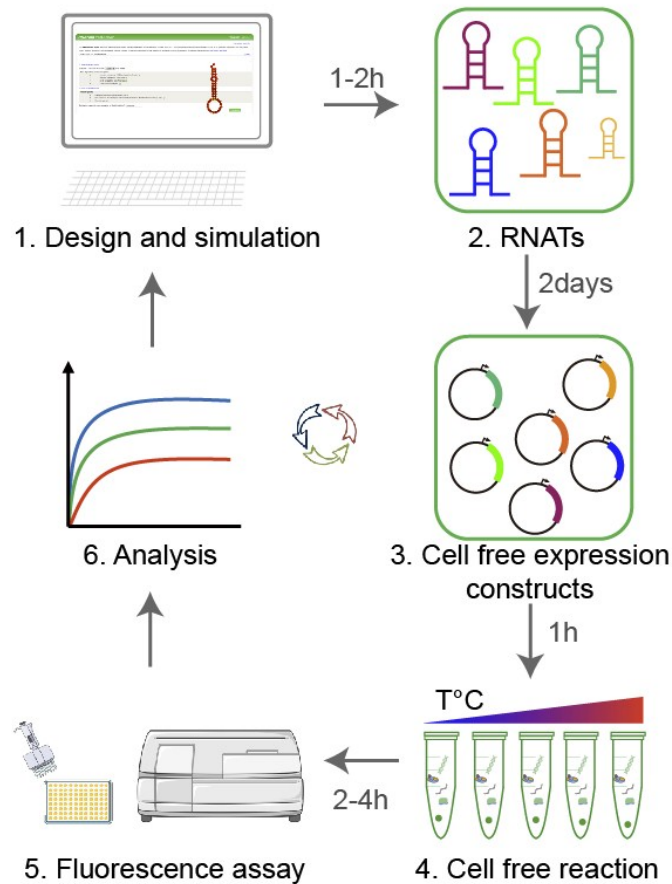
Microfluidic chip based droplets were generated according to the published protocol³. Briefly, all fluids were loaded into syringes (BD Luer-Lock™ 1-mL syringe) mounted onto high precision syringe pumps (neMESYS base 120 with neMESYS 290N). We formed micro-droplets by injecting PURE system as the inner phase and HFE7500 fluorinated oil with 1.8 % (w/w) PFPE-PEG-PFE biocompatible surfactant as the outer phase.

Imaging and image analysis

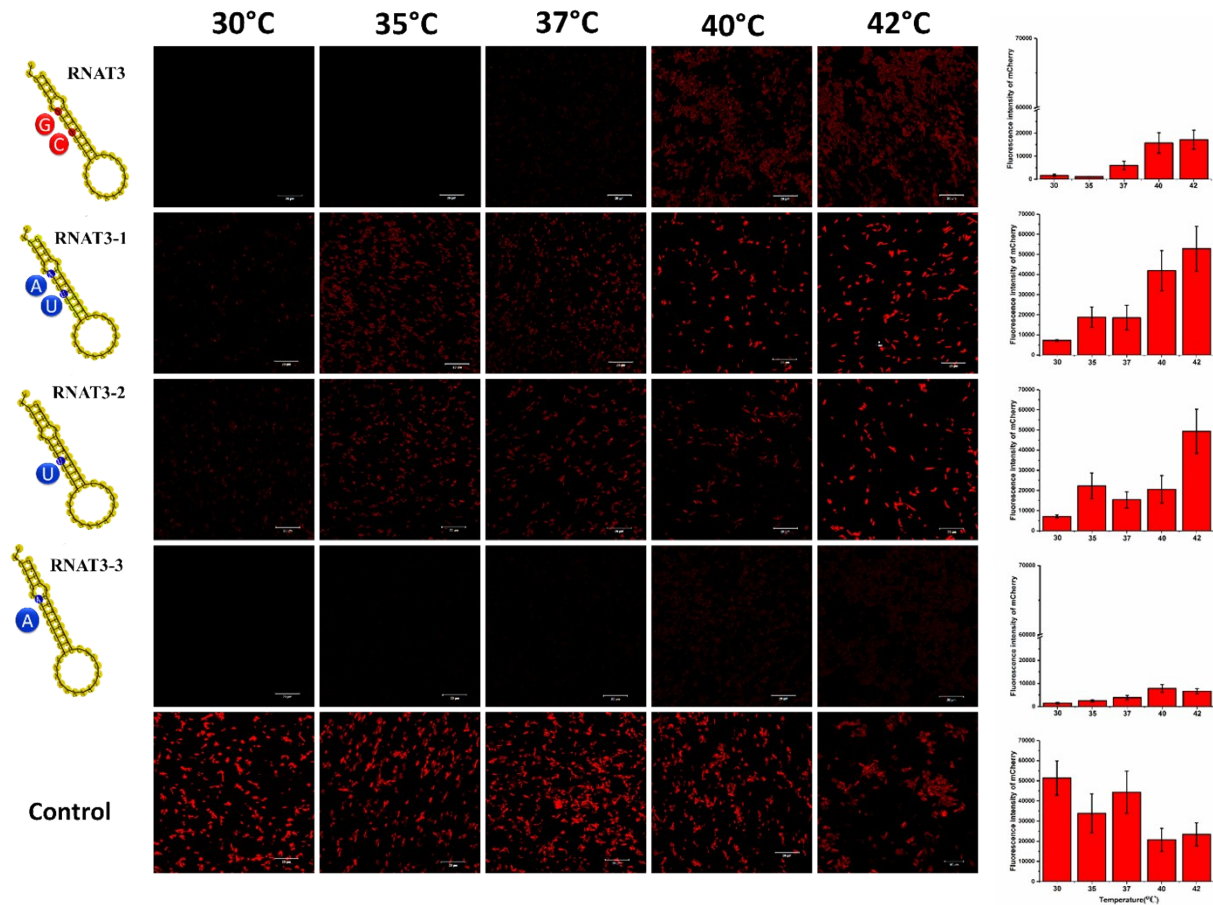
Imaging was taken by confocal microscopy (LSM780) equipped with an argon laser, C-Apochromat 40x/1.20 water-immersion objective and a incubation chamber. Laser lines 488nm, and 561nm lasers were used for fluorescence imaging. Image analysis and processing was carried out with Fiji⁴. The frames of time-lapse movies were normalized to have a constant overall intensity. Representative micrographs and intensity curves correspond to at least three successfully repeated experiments. Fluorescence intensities of droplets were quantified by Analyze Particles Plugins.



Supplement Figure S1. Mg²⁺ concentration influences the functionality of RNAT3 in PURE. Compared to the 13 mM Mg²⁺ reference concentration, adding more Mg²⁺ (Magnesium acetate, ≤ 1–2mM (inhibition concentration)) drastically inhibited the switching-on behavior of RNAT3 at 42°C. The possible reason could be that high concentrations of magnesium ions mediate the RNA secondary structure stabilization ⁵.

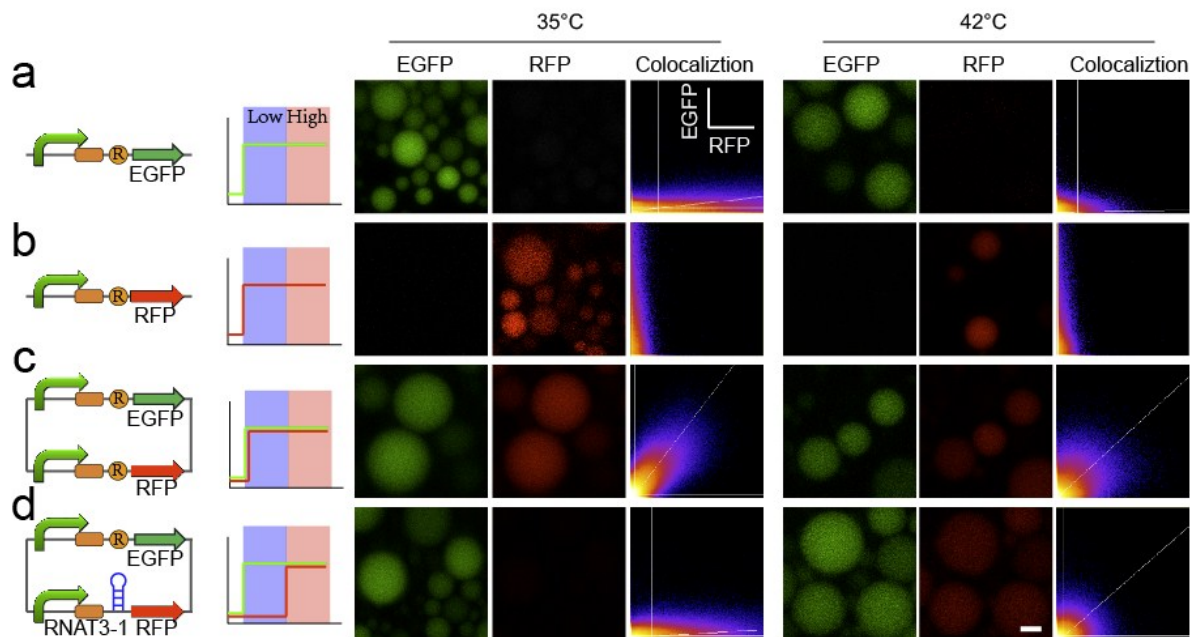


Supplement Figure S2. Tuning RNA thermometers in cell free system. Illustration of *in vitro* design and investigation process: (1-2) RNA thermometers sequence design and simulation with online tool; (3) Plasmid construction with site mutation or fragment changing. (4) Cell free reaction setup at different temperature; (5) Fast fluorescence measurement by plate reader. Then according to the results, the RNATs will be kept as candidates or redesigned for next round

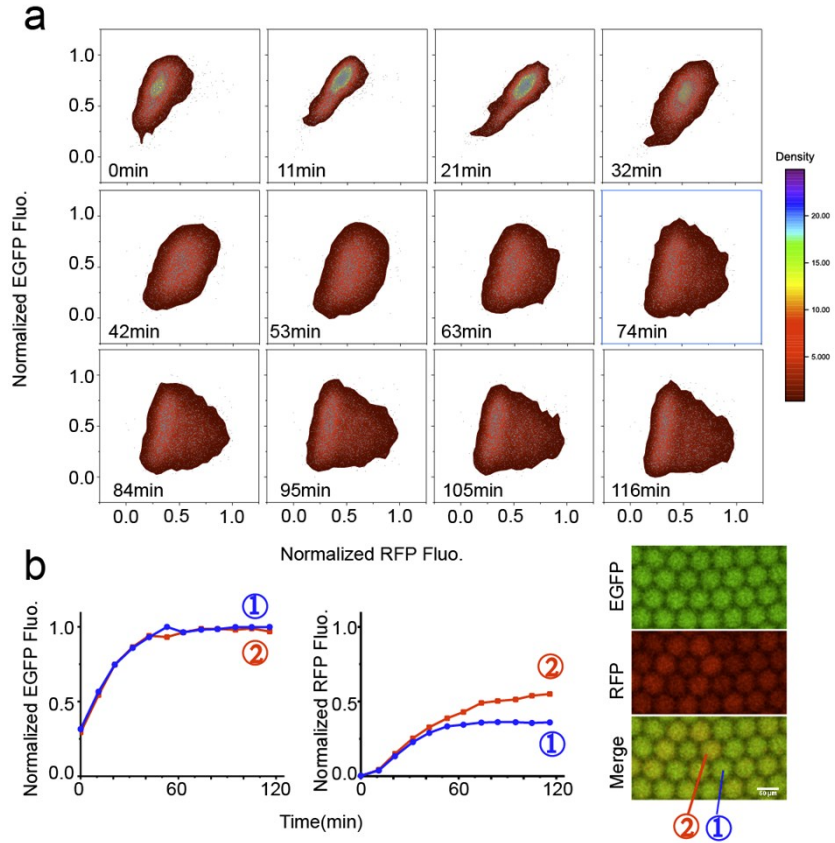


Supplement Figure S3. *In vitro* screened RNA thermometers function *in vivo*. The represent fluorescence images show RFP expression controlled with RNATs at different temperature. Scale bars, 20 μ m. The right column charts show the quantified fluorescence intensity of the whole population of *E. coli* at different temperature with image J. The sensing temperature slightly shifted to lower temperature *in vivo*. The temperature threshold of RNAT3-1 and RNAT3-2 *in vivo* were 35°C and 30°C (*in vitro* 37°C and 35°C), respectively. It seems that their secondary structures *in vitro* were more stable than *in vivo*. Intriguingly, RNAT3 and RNAT3-3 remained comparable *in vitro* and *in vivo*. Compared the sequence between RNAT3 and RNAT3-2, only one site is different, but their switching manners showed significant different both *in vitro* and *in vivo*. This variability may arise from mRNA secondary structure. Several factors *in vitro* may be more susceptible to effect the secondary structure compared with the natural biological system. Firstly, the PURE system lacks RNA helicases that utilize the energy from ATP hydrolysis to unwind RNA⁶. Secondly, Magnesium ions play an important role in maintaining the secondary structure

during translation. The concentration of Mg^{2+} in PURE system is $13mM^6$, which is much higher than in *E. coli* (5 mM). High concentration of magnesium ions will stabilize the RNA secondary structure ^{7, 8}.



Supplement Figure S4. Thermal controlled multiplexer. a.-d.) The diagrams show the design of thermos-gene circuits and the multiplexed thermal activation with different temperature. T7-RBS-EGFP, T7-RBS- RFP and the T7-RBS-EGFP-T7-RBS- RFP (on two plasmids) were regarded as the control constructions. In the multiplexer, RFP is gated by RNA thermometer (RNAT3-1) and T7 promoter. EGFP is gated by T7 promoter and an unblocked ribosome binding site on another plasmid. Right: represent images of thermal-multiplexer controlled protocell at 35 and 42 °C. The images were analysed by colocalization for demonstrating the two-colour fluorescence proteins expression in the droplets. Scale bar, 20 μ m.



Supplement Figure S5. a.) Normalized EGFP versus normalized RFP intensities of the whole population of droplets after the start of expression. b.) Fluorescence time courses of EGFP and RFP in a single droplet. Scale bar, 50 μm . ① and ② are two respective droplets that showed different expression ability of RFP.

Supplement TableS1

Name	Sequence
RNAT3	TACTAGAGCTCTTTAAAAAAAAAAAAAGTACTAAGGAGTACTAG
RNAT3-1	TACTAGAACTTTTTAAAAAAAAAAAAAGTACTAAGGAGTACTAG
RNAT3-2	TACTAGAGCTTTTTAAAAAAAAAAAAAGTACTAAGGAGTACTAG
RNAT3-3	TACTAGAACTCTTTAAAAAAAAAAAAAGTACTAAGGAGTACTAG

Supplement TableS2 list of vectors genes

<p>Pcoofy1-RNAT3-E1010</p> <p>TTGACAGCTAGCTCAGTCCTAGGTATAATGCTAGCTACTAGAGCTCTTTAAAAAAAAAAAAAGTACTAAGGAGTACTAGATGGCTTCTCCGAAGACGTTATCAAAGAGTTCATGCGTTTCAAAGTTCGTATGGAAGGTTCCGTTAACGGTCACGAGTTCGAAATCGAAGGTGAAGGTGAAGGTGTCGTCGTACGAAGGTACCCAGACCGCTAAACTGAAAGTTACCAAAGGTGGTCCGCTGCCGTTGCTGGGACATCCTGTCCCCGCAGTTCAGTACGTTCCAAAGCTTACGTAAACACCCGGCTGACATCCCGGACTACCTGAAACTGTCCTTCCCGAAGGTTTCAAATGGGAACGTGTTATGA ACTTCGAAGACGGTGGTGTGTTACCGTTACCCAGGACTCCTCCCTGCAAGACGGTGAGTTCATCTACAAAGTTAAACTGCGTGGTACCAACTTCCCGTCCGACGGTCCGTTATGCAGAAAAAACCATGGGTTGGGAAGCTTCCACCGAACGTATGTACCCGGAAGACGGTGTCTGAAAGGTGAAATCAAAATGCGTCTGAAACTGAAAGACGGTGTCACTACGACGCTGAAGTTAAAACCACTACATGGCTAAAAACCGGTTGAGCTGCCGGGTGCTTACAAAACGACATCAAACTGGACATCACCTCCCACAACGAAGACTACACCATCGTTGAACAGTACGAACGTGCTGAA.GGTCGTCCTCCACCGGTGCTTAATAACGCTGATAGTGCTAGTGTAGATCGC</p>
<p>Lacl-RBS-T7-T7-lacO-RNAT3-1-E1010</p> <p>tcactgccgctttccagtcgggaaacctgtcgtgccagctgcattaatgaatcgccaacgcgcgaggagaggcggtttgctattggcgccaggggtgtttttctttccaccagtgagacgggcaacagctgattgcccttcaccgcctggccctgagagagttgagcaagcggtccacgctgtttgccagcagggcgaatacctgtttgatgggtgtaacggcgggataatacatgagctgtcttccggtatcgctgtaactaccgagatccgcac caacgcgcagcccggactcggtaatggcgcgattgcgccagcgcctatgatcgttggcaaccagcatcgagtggaacgatgcctcattc agcatttgatggtttgtgaaaaccggacatggcactccagtcgcttccggttcgctatcggctgaatttgatgagtgatgagatattatgccagccagacgcagacgcggagacagaacttaatgggcccctaacagcgcgatttctggtgaccaatgcgaccagatgctccagccc agtcgctaccgtcttcatgggagaaaataactgttgatgggtgtcgtgcagagacatcaagaaataacgccggaacattagtcaggcagc ttccagcaatggcatcctggtcatccagcggatagtaatgatcagcccactgacgcgttgcgcgagaagattgtcaccgcccgtttacaggtc tcgacgccgttctgcttaccatcgacaccaccagctggcaccagttgatggcgcgagatttaacgcgcgacaatttgagcggcgctgc agggccagactggaggtggcaacccaatcagcaacgactgtttgcccccagttgtgtgccacgcggttgggaatgaattcagctccgccatc gccgcttccacttttcccgcgttttcgagaaacgtggctggcctggttaccacgcgggaacggtctgataagagacaccggcactctcgga catcgtatacgttactggtttcacggtatatctccttctaagtaaacaaaattattcctatagtgagtcgtattacgggatctgcagctctcct tatgcgactcctgattaggaagcagcccagtagtaggttagggcgttgagcaccgcccgcgaaggaatggtgatgcaaggagatggcgcc caacagtcccccggccacggggcctgccaccataccacgccgaacaagcgtcatgagcccgaagtgaggagcccgatctccccatcgggtg atgtcggcgatagggccagcaaccgacgtggcgcgggtgatgccggccacgatcgtccggcgtagaggatcgagatctgatcccgcg aaatgaatacgcactactataggggaattgtgagcggataacaattcccctctagaTACTAGAACTTTTTAAAAAAAAAAAAAGTACTA AGGAGTACTAGATGGCTTCTCCGAAGACGTTATCAAAGAGTTCATGCGTTTCAAAGTTCGTATGGAAGGTTCCGTTAACGGTTCACGAGTTCGAAATCGAAGGTGAAGGTGAAGGTGTCGTCGTACGAAGGTACCCAGACCGCTAAAC TGAAAGTTACCAAAGGTGGTCCGCTGCCGTTGCTGGGACATCCTGTCCCCGCAGTTCAGTACGTTCCAAA GCTTACGTTAAACACCCGGCTGACATCCCGGACTACCTGAAACTGTCCTTCCCGAAGGTTTCAAATGGGAACG TGTTATGAACTTCGAAGACGGTGGTGTGTTACCGTTACCCAGGACTCCTCCCTGCAAGACGGTGAGTTCATCT ACAAAGTTAAACTGCGTGGTACCAACTTCCCGTCCGACGGTCCGTTATGCAGAAAAAACCATGGGTTGGGA AGCTTCCACCGAACGTATGTACCCGGAAGACGGTGTCTGAAAGGTGAAATCAAAATGCGTCTGAAACTGAAA</p>

GACGGTGGTCACTACGACGCTGAAGTTAAAACCACTACATGGCTAAAAAACCGGTTGAGCTGCCGGGTGCTT
ACAAAACCGACATCAAACCTGGACATCACCTCCCACAACGAAGACTACACCATCGTTGAACAGTACGAACGTGCT
GAAGTCGTCACCTCCACCGGTGCTTAAgcggccgcactcgagcaccaccaccaccactgagatccggctgctaacaagcccg
aaaggaagctgagttggctgctgccaccgctgagcaataactagcataacccttggggcctctaaacgggtcttgaggggtttttg

References

1. H. Jia, X. Sun, H. Sun, C. Li, Y. Wang, X. Feng and C. Li, *ACS Synth. Biol.*, 2016, **5**, 312-320.
2. C. Papworth, J. Bauer, J. Braman and D. Wright, *Strategies*, 1996, **9**.
3. O. Wagner, J. Thiele, M. Weinhart, L. Mazutis, D. A. Weitz, W. T. Huck and R. Haag, *Lab Chip*, 2016, **16**, 65-69.
4. J. Schindelin, I. Arganda-Carreras, E. Frise, V. Kaynig, M. Longair, T. Pietzsch, S. Preibisch, C. Rueden, S. Saalfeld and B. Schmid, *Nat. methods*, 2012, **9**, 676-682.
5. D. E. Draper, *Rna*, 2004, **10**, 335-343.
6. Y. Shimizu, A. Inoue, Y. Tomari, T. Suzuki, T. Yokogawa, K. Nishikawa and T. Ueda, *Nat. biotechnol*, 2001, **19**, 751-755.
7. Y. Xue, B. Gracia, D. Herschlag, R. Russell and H. M. Al-Hashimi, *Nat. Commun*, 2016, **7**.
8. D. Thirumalai and N. A. Denesyuk, *bioRxiv*, 2016, 037895.

Publications

2D space regulation tools:

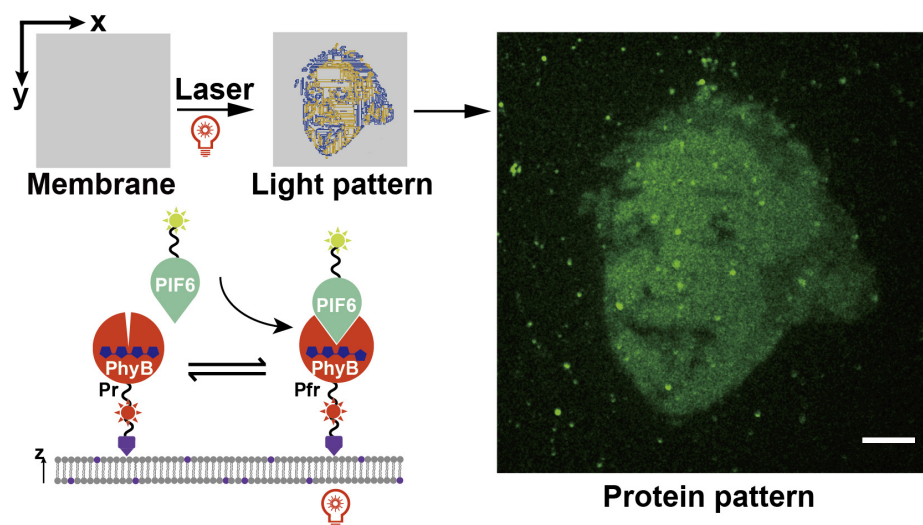
2.2 Light-induced Printing of Protein Structures on Membrane *in vitro*

In this manuscript, we engineered the light switchable dimerization system to spatiotemporally target protein on model membrane, and sequentially mediate protein assembly in cell free systems.

The results discussed in this section have been published as: “Jia, H., Kai, L., Heymann, M., García-Soriano, D. A., Härtel, T., & Schwille, P. (2018). Light-induced Printing of Protein Structures on Membranes *in vitro*. Nano letters, 18(11), 7133-7140.”

Source online: DOI: 10.1021/acs.nanolett.8b03187

Reprinted with permission have been granted by the publisher.



Light-Induced Printing of Protein Structures on Membranes in Vitro

Haiyang Jia,[†] Lei Kai,[†] Michael Heymann,[†] Daniela A. García-Soriano,^{†,‡} Tobias Härtel,[†] and Petra Schwille^{*,†}

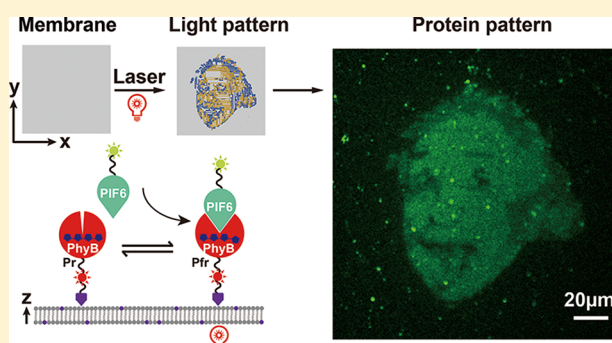
[†]Max Planck Institute of Biochemistry, Am Klopferspitz 18, D-82152 Martinsried, Germany

[‡]Graduate School for Quantitative Biosciences (QBM), Ludwig-Maximilians-University, Munich, Germany

S Supporting Information

ABSTRACT: Reconstituting functional modules of biological systems in vitro is an important yet challenging goal of bottom-up synthetic biology, in particular with respect to their precise spatiotemporal regulation. One of the most desirable external control parameters for the engineering of biological systems is visible light, owing to its specificity and ease of defined application in space and time. Here we engineered the PhyB-PIF6 system to spatiotemporally target proteins by light onto model membranes and thus sequentially guide protein pattern formation and structural assembly in vitro from the bottom up. We show that complex micrometer-sized protein patterns can be printed on time scales of seconds, and the pattern density can be precisely controlled by protein concentration, laser power, and activation time. Moreover, when printing self-assembling proteins such as the bacterial cytoskeleton protein FtsZ, the targeted assembly into filaments and large-scale structures such as artificial rings can be accomplished. Thus, light mediated sequential protein assembly in cell-free systems represents a promising approach to hierarchically building up the next level of complexity toward a minimal cell.

KEYWORDS: Photoactivation, pattern formation, membranes, bottom-up, synthetic biology, FtsZ



Moreover, when printing self-assembling proteins such as the bacterial cytoskeleton protein FtsZ, the targeted assembly into filaments and large-scale structures such as artificial rings can be accomplished. Thus, light mediated sequential protein assembly in cell-free systems represents a promising approach to hierarchically building up the next level of complexity toward a minimal cell.

The systematic construction of cellular functions module by module from the bottom up is a painstaking but valuable exercise for understanding biological systems, particularly with respect to revealing a minimal essence of life and its origin on earth.¹ In fact, even the smallest system that could be identified by abstraction from existing life forms still appears to be highly complex.² Thus, constructing essential modules from the bottom up will potentially benefit from the substitution of some subsystems with simpler analogs that could be addressed by external cues.¹ Until now, some minimal systems such as actomyosin structures³ and parts of the bacterial cell division machinery^{4,5} have been successfully studied in vitro by reconstitution on biological mimics of cellular membranes both in 2D on supported lipid bilayers and in 3D within membrane-clad soft polymer microcompartments or giant unilamellar vesicles. These model membranes provide a versatile platform to quantitatively study protein-induced patterns and transformations that are hardly discernible in vivo. However, because of the spatial homogeneity of the model membrane, the formation of protein structures solely relies on the self-assembly properties of the protein themselves and leaves little room for precise large-scale regulation of processes in space and time compared to cellular membranes.⁶ Therefore, to quickly move on to more globally regulated mimics of cellular processes, external spatiotemporal control elements should be introduced, which will help to boost

functionality while still keeping the compositional complexity of a bottom-up assembled synthetic biological system minimal.

Utilizing light to regulate protein properties and functions represents a powerful approach both in vivo and in vitro due to its specificity, ease of use, and spatiotemporal control of application.^{7–9} So far, various optochemical and optogenetic tools for patterning protein have been developed, which can control protein assembly in different dimensions.^{10–13} Optochemical approaches, such as chemically modified phospholipid anchors for applications with membrane proteins¹⁴ or photoactivatable chemical dimerization,¹⁵ provide high spatial control and biorthogonality for membrane targeting; however, many of them rely on cytotoxic UV light activation and function only irreversibly.¹⁶ Some promising optochemical approaches using nontoxic light, like two photon activation, have not yet been made compatible for membrane applications.¹¹ Compared with synthetic chemicals introduced to the biological system, optogenetic tools based on proteins in the visible spectral range are comparably specific, while more biologically compatible and reversibly applicable. Because of their low phototoxicity, protein based optogenetic tools are thus very promising in physiologically relevant studies. Diverse

Received: August 3, 2018

Revised: October 4, 2018

Published: October 8, 2018

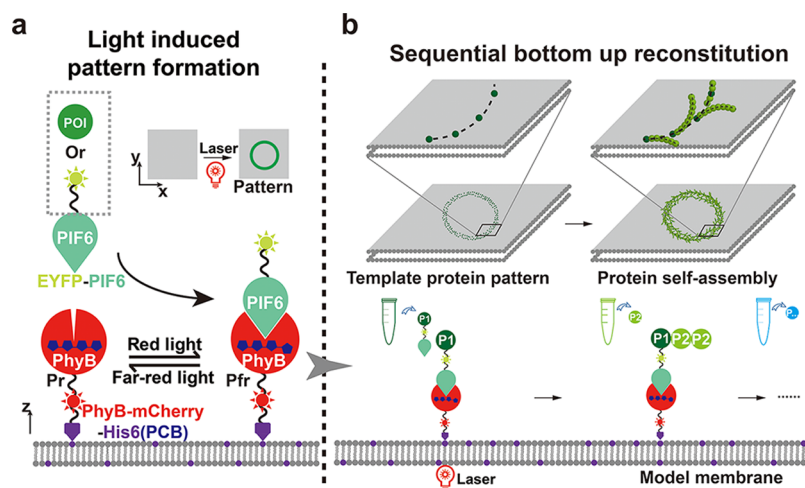


Figure 1. Light controlled bottom-up protein assembly in cell-free systems. (a) PhyB covalently binding to the chromophore phycocyanobilin (PCB) can be targeted to the model membrane with a His6 membrane anchor. Upon red or infrared light illumination, PhyB undergoes conformational switching between the Pr and Pfr states and reversibly associates with the PIF6 domain. The PIF6 domain as a ligand can thus be used to target any protein of interest (POI) to the membrane. (b) Sequentially assembling proteins unit by unit into intrinsic (left) or artificial (right) ring structures.

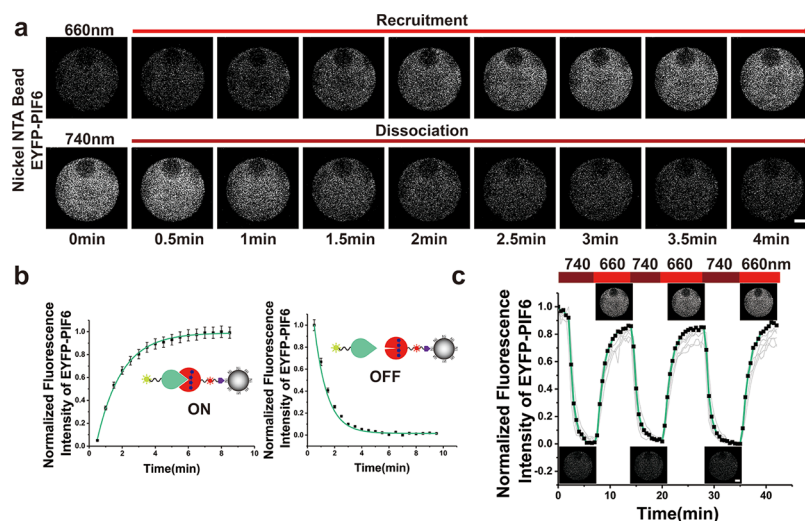


Figure 2. Reversible PhyB-PIF photoswitching in vitro. (a) PhyB-PIF6 photoinduced recruitment to the surface of Ni-NTA agarose beads. (b) Fitting exponentials to the fluorescence intensity rise and decay of EYFP reveals typical k_{on}/k_{off} constants ($n = 3$). The black error bars represent the standard deviations of the fluorescence intensity. (c) Recruitment cycles of EYFP-PIF6 by alternating between 660 and 740 nm illumination. Normalized fluorescence intensity of EYFP on the beads for this series was plotted. EYFP-PIF6 concentration: $8 \mu\text{M}$. Scale bars in panels a and c are $20 \mu\text{m}$.

light-inducible protein interaction pairs were developed for controlling protein binding to membranes including the cryptochrome 2 (CRY2) and cryptochrome-interacting basic helix–loop–helix 1 (CIB1);¹⁷ flavin-binding kelch repeat f-box (FKF1) and GIGANTEA (GI);^{18,19} engineered photoreactive light oxygen-voltage domains (LOV and LOV2);^{16,20} engineered vivid (VVD, pMag/nMag);²¹ bacterial phytochrome photoreceptors (BphPs) and their natural binding partner (PpsR2);²² a plant phytochrome B (PhyB); and the phytochrome-interacting factors (PIF).^{23,24} The engineered LOV proteins (iLID and Nano) have been applied to pattern proteins on GUVs; however, they have been operated monodirectionally, that is, controlled by just one wavelength, and spontaneously switch off in the dark.¹⁶ Currently, the phytochrome B (PhyB)–phytochrome interacting factor (PIF) is the only light-induced dimerization system that operates at

long wavelength light.¹⁷ It detects red and near-infrared light through the photoisomerization of a covalently bound tetrapyrrole chromophore such as phycocyanobilin (PCB). The plant PhyB can be photoconverted between two conformational states called Pr (red-absorbing) and Pfr (far-red-absorbing). The active form of PhyB is able to interact with its nuclear signaling partner phytochrome interacting factor (PIF), forming a dimer that is red/far-red light-dependent (Figure 1a). In previous work, the PhyB and PIF light-dependent interactions have been utilized for gene transcription regulation in Yeast and mammalian cells,^{25,26} protein–protein interaction regulation,^{27,28} and controlling signaling processes in vivo.^{17,23,29}

So far, however, none of the reported systems based on light induced protein interactions has been employed to enable precise spatiotemporal control of protein self-assembly on

model membranes *in vitro*. Here, we engineered the PhyB-PIF system to selectively target proteins onto model membranes and spatiotemporally guide large-scale protein self-assembly in a cell free system, representing a promising approach to building up the next level of complexity toward a minimal synthetic cell (Figure 1).

To engineer a robust light-induced targeting system *in vitro*, we first confirmed that the *in vitro* purified PhyB-PIF sensor pairs can function as well as *in vivo*. Multiple potential phytochrome-PIF pairs were chosen as candidates. The wild-type (residues 1–908),^{30,31} photosensory core (residues 1–650),^{32,33} and the minimal photosensory core (residues 1–621)¹⁷ have been reported to function as light sensors responding to red light for interaction with their respective binding partners (PIF3/6).^{17,23} However, the interaction between the PhyB photosensory core (residues 1–650) and PIFs is irreversible under infrared light.²³ Additionally, full-length wild type PhyB (residues 1–908) is hard to purify even if using double tags (N-terminal streptag and C-terminal His6 tags). Of the previously reported PIF domains, only the N terminus of PIF6 (residues 1–100) is sufficient to cause significant translocation of protein to the membrane.³¹ Finally, we chose the PhyB (residues 1–621) and PIF6 (residues 1–100) pair as our optical tool to induce reversible interactions.

The PhyB was labeled by fusing it to the mCherry by a 15 AAs long flexible linker. A C-terminal His6 tag of PhyB was used as an anchor to target the protein to the Ni-NTA functionalized surface. PIF6 as the ligand, which can carry any protein of interest to the membrane when interacting with PhyB, was labeled with the enhanced yellow fluorescence protein (EYFP) (Figure 1a). To verify their function, we immobilized PhyB on the surface of Ni-NTA agarose beads and then incubated with soluble PIF6 protein (without His tag). Their light-dependent interaction was measured by the fluorescence translocation assay.^{17,31} The ligand PIF6 was rapidly recruited to the beads upon red light illumination (660 nm, light intensity: $\sim 0.386 \text{ mW cm}^{-2}$) and disassociated under far-red light illumination (740 nm, light intensity: $\sim 0.304 \text{ mW cm}^{-2}$) (Figure 2a and Supplement Movie S1). The “on” and “off” switching can be robustly repeated by switching between two wavelengths (Figure 2c). The PhyB induced recruitment of EYFP-PIF6 reveals fast association ($k_{\text{on}} 660 \text{ nm} = 0.62 \pm 0.02 \text{ min}^{-1}$; $t_{1/2}$: 1.17 min) and dissociation ($k_{\text{off}} 740 \text{ nm} = 0.97 \pm 0.0 \text{ min}^{-1}$; $t_{1/2}$: 0.72 min) (Figure 2a,b). We observed that increasing the EYFP-PIF6 concentration from 0.25 μM to 4 μM increased the association rates and dissociation rates (Supplement Figure S10).

We also measured the absorbance spectrum of the purified PhyB-mCherry-His6 protein charged with 1.5 mM PCB *in vitro*. When irradiated under continuous red light (660 nm), the *in vitro* absorbance peak at around 725 nm is reduced and a second peak at 650 nm can be observed. Upon 740 nm light illumination, the absorbance can be switched back (Supplement Figure S1a). Remarkably, not only 660 nm can activate PhyB-mCherry, but also other wavelengths like green light at 550 nm can induce the conformational switch of PhyB (Supplement Figure S1b), according to the reported results.²⁰ Thus, the more widespread 561 nm laser line can be used to activate the PhyB/PIF6 pair interaction and target protein precisely to Ni-NTA beads (Supplement Figure S2a). In the same way as for red light (660 nm), the 561 nm laser activation can be reversed dynamically by far-red light (Supplement Figure S2b,c and Supplement Movie S2).

The rapid forward and reverse kinetics of the PhyB-PIF system allow us to dynamically control protein association and dissociation *in vitro* by switching between the two wavelengths. To obtain maximum spatial control, we chose a planar supported lipid bilayer (SLB) as model membrane and applied the above validated PhyB-PIF pair onto the SLB, which generated light controlled 2D patterns.

First, to check whether the PhyB-mCherry-His6/EYFP-PIF6 pair works equally well as on beads, we investigated the global light-induced on- and off-recruitment to the SLB. Different concentrations of DOGS-NTA(Ni) lipid mixed with DOPC were used to establish homogeneous PhyB-mCherry-His6 layers. Bilayer fluidity ensures that even at low chelator lipid densities, the His tag can frequently interact with potential binding sites, forming multivalent protein–lipid complexes and greatly stabilizing the surface species.³⁴ After immobilization, the excess soluble PhyB-mCherry-His6 protein was carefully washed away using a pipet. Although His tag and Ni-NTA binding is reversible,³⁵ the slow transition from multivalent to monovalent will make the polyvalently bound protein remain stable on the SLB surface over 23 h.³⁴ Such multivalent immobilization³⁶ provides us a stable microenvironment for light-induced patterning. Upon incubation with PIF6-EYFP in the dark, only a small amount of protein was recruited to the membrane after washing. Upon 660 nm light illumination, an EYFP-PIF6 layer was formed on the SLB by interacting with PhyB. The fluorescence of the EYFP-PIF6 increased about five-fold compared with the dark condition control (Supplement Figure S3b). The resulting layer of recruited PIF6-EYFP was rapidly released back to the solution by continuous exposure with inactivating far-red light (740 nm, light intensity: $\sim 0.304 \text{ mW cm}^{-2}$) (Supplement Figure S3). With similar EYFP-PIF6 concentration, the light controlled on and off dynamics on SLBs are similar to that on agarose beads (Supplement Figure S10e,f). Protein localized at a membrane may undergo lateral diffusion,³⁷ which limits the spatial precision of membrane targeting.¹⁵ Thus, the mobility of PhyB-mCherry-His6 was checked by fluorescence recovery after photobleaching (FRAP). When the mCherry was bleached with the 561 nm laser, the signal in the bleached area (mobile fraction: $7.3 \pm 3.5\%$) showed a negligible recovery compared to fluorescent lipids (mobile fraction: $92.0 \pm 8\%$). PhyB-mCherry-His6 itself has slow mobility, even at low membrane protein densities, and the slow mobility is independent of NTA-lipid density (Supplement Figure S4c). However, the rather immobile PhyB-mCherry-His6 does not affect membrane fluidity itself (Supplement Figure S4c,d). Compared with PhyB-mCherry-His6, His6-EGFP showed a high mobile fraction of $90.4 \pm 6\%$ on high concentration NTA(Ni) lipid (34 mol % DOGS-NTA(Ni); 66 mol % DOPC), demonstrating that the static behavior is not a membrane artifact (Supplement Figure S4a) but rather induced by protein properties. Any interaction with another protein may affect the lateral diffusion of a membrane protein.³⁸ In our case, PhyB monomers can form head-to-head dimers.³⁹ Each monomer contains one His6 tag as membrane anchor that interacts with NTA lipid. This multivalency leads to protein–lipid complexes that greatly stabilize the surface binding. This may affect the lateral diffusion on membrane and finally make the protein nearly static. Because of the low mobility of the first protein layer, all subsequently recruited binding partners can also be considered

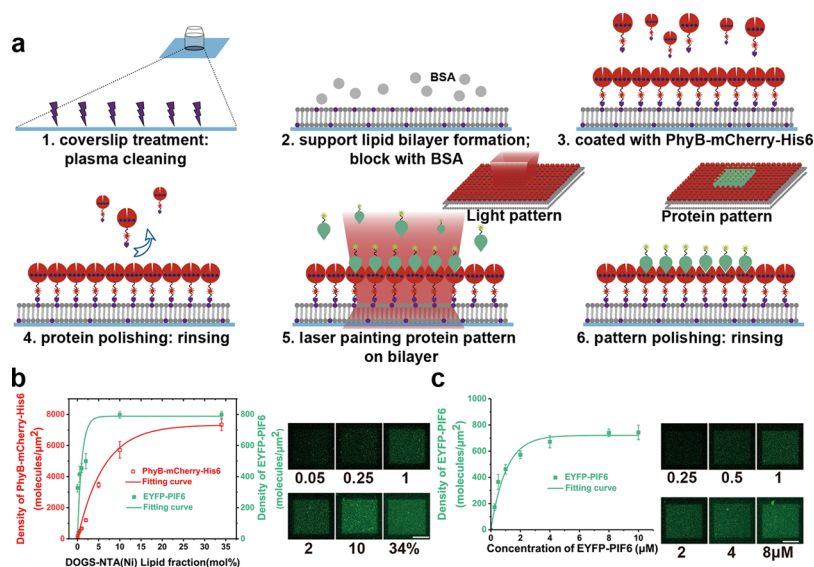


Figure 3. Light-printing protein patterns on supported lipid bilayers. (a) Schematic of the patterning principle. (1) Preparation of glass cover slides by plasma cleaning. (2) Generation of a uniform supported DOPC lipid bilayer containing DOGS-NTA(Ni) lipid. (3, 4) Immobilization of PhyB-mCherry-His6 protein on the membrane and rinsing away excess soluble protein. (5, 6) Incubation with the ligand EYFP-PIF6 and photo activating a pattern by 561 or 633 nm laser illumination. After activation, the protein pattern can be polished by washing. (b) Defined protein patches printed on different DOGS-NTA(Ni) lipid fractions from 0.05 mol % to 34 mol % (1 μM phyB-mCherry-His6, 8 μM EYFP-PIF6 in solution), scale bar 10 μm . (c) Dependence of printed protein density (i.e., fluorescence intensity) on EYFP-PIF6 concentration in solution (SLB: 34 mol % DOGS-NTA(Ni) and 64%mol DOPC), scale bar 10 μm . Protein densities were determined by quantitative epifluorescence microscopy.⁴⁰ For the plots, each data point was generated from at least three different protein patterns in the sample chamber. Error bars represent the mean value and standard deviation of the three independent experiments. The plots were fitted with BoxLucas model.

as nearly static. This renders PhyB-mCherry-His6 an excellent primer for stable protein patterns on the lipid bilayer.

To improve the spatial precision of light-printed protein patterns on the membrane, we utilized the custom mode of a confocal microscope for photobleaching predefined regions with high optical resolution. This allowed us to print a defined protein pattern on the SLB (Figure 3a and Supplement Figure S5). In the same way as for the global activation on Ni-NTA SLBs, PhyB-mCherry-His6 was incubated with the Ni-NTA-SLB to form a homogeneous protein layer. Then the unbound protein was washed away to avoid undesired light-induced interactions in the solution above the membrane. Owing to the flexibility of confocal illumination, we can design nearly any pattern by the “region of interest” function. For activation and transfer of a specific pattern to the membrane, the 561 or 633 nm laser lines can be employed (Supplement Figure S6). To decrease the amount of unspecific activation by reflected or scattered light, a continuous isotropic “protecting” illumination by infrared light from a simple LED source (2% 740 nm) was applied. The rapid “off” kinetics of the PhyB-PIF interaction traps the membrane-recruited EYFP-PIF6 pool to the pattern, as any EYFP diffusing away is dissociated from the membrane by the surrounding far-red light.²³ This light-induced painting is PCB dependent. In the control experiment where PCB was missing, no binding was detected (Supplement Figure S5). The active state of PhyB(Pfr) slowly converts back to inactive Pr state by spontaneous thermal reversion.³⁹ Therefore, the protein pattern persisted much longer in the dark than under illumination (Supplement Figure S10g,h). Because of the nearly static behavior of PhyB, the protein patterns were still visible for at least 4 h (Supplement Figure S10i).

Protein densities of the patterns were determined by quantitative epifluorescence microscopy.⁴⁰ Naturally, the adsorbed protein density depends strongly on the NTA lipid

fraction and the protein concentration in solution (Figure 3b,c). Additionally, after activating pattern formation on the membrane, the density of adsorbed molecules is regulated by the intensity of laser light and the activation time (Figure 4a). Under 1.6 mW laser power, the binding ratio of PhyB-PIF is around 10:1, calculated by the protein densities in the patterns. Here, the EYFP-PIF6 density in the pattern can reach up to about 800 molecules per μm^2 . Strong laser light and longer activation time will accelerate and enhance the protein recruitment, respectively. By controlling the protein concentration, laser power, and activation time, the protein density on the membrane can be controlled from 100 to 1000 molecules per μm^2 .

The pattern formation relies on the photoactivation; therefore, the smallest scale of possible features in the pattern depends on the resolution of the scanning laser. Two printed lines with distances about 1 and 0.5 μm resolution in x and y direction, respectively, can still be visibly resolved (Supplement Figure S9). Additionally, single protein line with lowest thickness of about 0.56 μm can be printed (Figure 4b). Because of the high resolution illumination, complex patterns with features ranging from 500 nm to 1 mm can be printed in one step within seconds like the logo of MaxSynBio (Max Planck Research Network in Synthetic Biology) (Figure 4c). To generate patterns with more than two brightness values (“grey scales”), like the pixel picture of Albert Einstein, the printing can be done sequentially by varying laser intensity (Figure 4d). The two-color printing can also be successfully processed with two different proteins (EYFP-PIF6 and EYFP-PIF6 labeled with Alexa Fluor 405 NHS ester) (Supplement Figure S11). In principle, the dual-color printing may even be extended to additional colors in the future. Our current setup is limited by loading different proteins manually. This can cause laser focus shifts; therefore, custom-made microfluidics

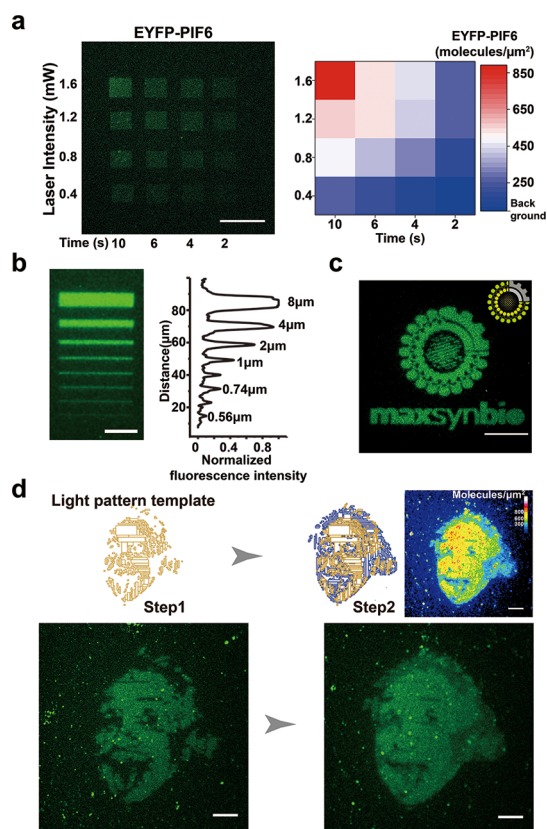


Figure 4. Light induced arbitrary patterns on supported lipid bilayers. (a) Protein gradient printing by varying laser intensity and incubation time (left, protein pattern; right, heat map plot of EYFP-PIF6 density on the patterns induced with different laser intensity and activation time), scale bar $20 \mu\text{m}$. (b) Printed protein lines with thickness values from eight micrometers to half micrometer, scale bar $20 \mu\text{m}$. The right panel shows the intensity distribution of the eight lines. (c) Two-dimensional MaxSynBio protein logo printed on the membrane, scale bar $50 \mu\text{m}$. (d) Gray-scale picture of Albert Einstein printed sequentially with two densities pattern of EYFP-PIF6, scale bar $20 \mu\text{m}$. Green signals represent the localization of EYFP-PIF6.

will be needed for such extended multicolor patterns in the future to render loading and rising more precise. Besides the 2D SLB, our approach can also be applied to 3D micro-compartments, like GUVs, showing great promise for a sequential and spatially well-defined bottom-up protein assembly on membranes in vitro.

Having shown that a precise spatial targeting of proteins to membranes can be achieved, we aim to transfer large-scale protein self-assemblies to selected loci by light. The final goal is to bottom-up assemble functional protein machineries with membrane activity such as contractile rings for enforced membrane fission. Consequently, the self-assembly prone protein we chose here for being templated by light is the primary factor of the bacterial Z ring, FtsZ.

During bacterial cell division, the tubulin homologue FtsZ is the first protein positioned to the division site. It is essential for recruiting other proteins that produce a new cell wall between the dividing cells.⁴¹ Purified FtsZ assembles into polar, straight, or gently curved proto-filaments in the presence of GTP. Lateral interactions between FtsZ proto-filaments can lead to higher-ordered structures such as tubules, bundles, circles, and sheets.^{42,43} In *Escherichia coli*, FtsZ is recruited to the membrane by FtsA, which binds to the membrane through a

C-terminal amphipathic helix,^{44,45} and the transmembrane protein ZipA.⁴⁶ The precise targeting of the Z ring to the middle of the long cell axis is accomplished by several biochemical cues, of which the Min protein oscillations and nucleoid occlusion are the most prominent.^{47,48} However, positioning by these factors is strongly dependent on compartment geometry as well as the exact concentrations of proteins and nucleotides. Thus, we here explore the ability to circumvent the biochemically regulated positioning by selective light-induced targeting of FtsZ structures to predefined positions.

To this end, FtsZ (1–366)-YFP, a truncated FtsZ-construct⁵ but without a membrane targeting sequence, was fused to the PIF6 ligand by a 19 amino acid flexible linker. We refer to this construct as “FtsZ-YFP-PIF6”. Through the light induced recruitment of FtsZ to the membrane, FtsZ can self-assemble into ring structures ($0.727 \pm 0.209 \mu\text{m}$, $n = 96$) with a similar diameter as the *E. coli* cell ($0.7\text{--}1.4 \mu\text{m}$ ⁴⁹). Although the rings do not appear to perform dynamic treadmilling as observed in direct membrane-attached FtsZ,⁴ a progressive growth dynamics can be observed. After local activation by red light (660 nm, light intensity 2% 193 mW, time point: 0 min), short intrinsically curved filaments of FtsZ started to appear on the membrane, forming a nucleation point to steadily grow in width and length by recruiting new FtsZ protofilaments for lateral assembly. Thus, they self-organized into a rapidly reorganizing structure that matured into a cell-sized ring (Figure 5a and Supplement Movie S4 for single ring and Supplement Movie S4 for overview of rings). The ring diameter continued to grow for about 25 min (Figure 5a right). Comparable growth in size has also been reported in

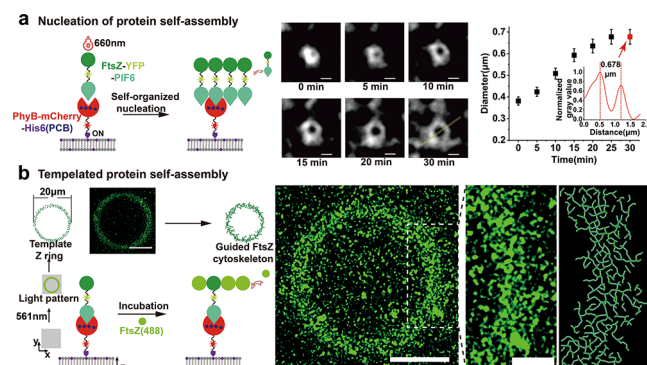


Figure 5. (a) Nucleation of FtsZ protein self-assembly on SLB. FtsZ was recruited to the membrane through interaction of PhyB and PIF6, when activated with 660 nm light. The middle images show typical ring patterns of FtsZ emerging from nucleation points locally selected through light-sensitive interaction (FtsZ-YFP-PIF6, $4 \mu\text{M}$; 5 mM Mg^{2+} , 4 mM GTP). The images were taken by total internal reflection fluorescence microscopy (TIRFM). Scale bar: $0.5 \mu\text{m}$. Right figure: maturation time course curve of FtsZ ring diameter. Diameters were determined by measuring the peak-to-peak distance in the intensity plot profile (yellow line shown in the middle images). Black error bars: standard deviations of ring diameters. (b) Spatial templating of large-scale FtsZ networks. Ring patterns were obtained by 661 nm illumination on SLB (2 mol % DOGS-NTA(Ni), 98 mol % DOPC). After incubation with soluble FtsZ protein ($1.6 \mu\text{M}$ FtsZ (Alexa fluor 488 dye), 5 mM Mg^{2+} , 4 mM GTP), the light induced template ring (FtsZ-YFP-PIF6) recruited further FtsZ into a ring-shaped cytoskeletal network. Scale bars in the middle and zoom-in image: 10 and $4 \mu\text{m}$, respectively. The network was analyzed with stretching open active contours (SOAX).⁵¹

in vitro with natural anchor protein FtsA⁴ and artificial membrane targeting motifs to FtsZ.⁵⁰ In all cases, FtsZ forms growing ring patterns, indicating that the light-initiated growth observed here is supported by the intrinsic self-assembly properties of the protein. We also tested the reversibility of FtsZ ring assembly and confirmed that the rings can be reversibly removed from the membrane upon 740 nm (deactivation light) (Supplement Movie S5).

The demonstrated ability to spatiotemporally target nucleation sites for protein self-assembly is the starting point for a more elaborate design of functional 3D protein structures. FtsZ's structural features have so far been reported to promote the assembly of rings on membranes in only a small range of curvatures,⁴ with an upper limit of about one micrometer (see above), close to the resolution limit of standard microscopes. To evaluate whether considerably larger FtsZ structures can be templated, rings with diameters around 20 μm were patterned by light. The preexisting FtsZ-YFP-PIF6 can be organized into an unsmooth ring structure with many single nucleation points for FtsZ self-assembly, as shown above. In a second step, wild-type FtsZ labeled with Alexa fluor 488 dye was incubated with the light patterned ring-shaped seed (Figure 5b). FtsZ-YFP-PIF6 recruited FtsZ monomers into the template ring, forming bundles toward a 3D ring mimicry of a bacterial cytoskeleton (Figure 5b).

In conclusion, we have developed an in vitro protein patterning assay on membranes based on the reversible and light-switchable interaction PhyB-PIF6 that can enable spatiotemporal control for bottom-up protein self-assembly. The range of potential and desired applications extends from dynamically controlling local protein interactions in well-defined regions to spatially targeting the self-assembly of larger protein structures on membranes, which may selectively induce local membrane transformations. To this end, the optical templating will have to be adapted to support 3D illumination of transformable free-standing membranes, as in giant unilamellar vesicles (GUVs). Compared with the classical chemistry-based protein patterning methods in vitro,^{10,11,13,52–58} our assay has shown to be compatible with model membranes, allowing us to largely reduce diffusive spreading by using patterned light (Supplement Table S1) while mimicking natural biological regulation processes, not relying on unspecific chemical binding, thus preserving physiological properties. The method can function without special hardware besides widely available confocal microscopes. The high spatial and temporal specificity of light activation establishes this system as a useful tool for local control of protein patterns in two and three dimensions on model membranes. For bottom-up synthetic biology, the ability to guide large-scale and reversible self-assembly of functional protein structures by light can tremendously help in designing minimal cellular systems with desired properties, without having to rely entirely on biochemical cues. In summary, our method provides a promising tool for the design of biomolecular systems composed of proteins and model membranes. Fast patterning of proteins provides a promising tool to track many interactions and activities of proteins on membranes in parallel, representing a new design option for protein microarrays. In the future, approaches like this will greatly help the reconstitution of biological systems from the bottom-up, with a wide range of potential applications from fundamental protocell research to tissue engineering.

■ ASSOCIATED CONTENT

§ Supporting Information

The Supporting Information is available free of charge on the ACS Publications website at DOI: 10.1021/acs.nanolett.8b03187.

- Experimental procedures, supplemental figures (PDF)
- PhyB–PIF6 photoswitchable global recruitment in vitro tested on surface of Ni-NTA agarose beads (AVI)
- Reversibly spatial activating recruitment of EYFP-PIF6 protein to specific localization on beads with 561 nm laser and 740 nm LED light source (AVI)
- Single FtsZ ring emerging from its recruitment to supported membrane by light sensitive interaction (AVI)
- TIRF monitored global view of rings developing on SLB controlled with light-sensitive interaction (AVI)
- FtsZ rings dissociated from supported membrane under 740 nm light (AVI)

■ AUTHOR INFORMATION

Corresponding Author

*E-mail: schwille@biochem.mpg.de.

ORCID

Haiyang Jia: 0000-0002-8330-5031

Lei Kai: 0000-0003-0879-7918

Michael Heymann: 0000-0002-9278-8207

Daniela A. García-Soriano: 0000-0003-2849-8528

Tobias Härtel: 0000-0002-6952-0667

Petra Schwille: 0000-0002-6106-4847

Notes

The authors declare no competing financial interest.

■ ACKNOWLEDGMENTS

H.J. was supported by the GRK2062 Molecular Principles of Synthetic Biology, funded by Deutsche Forschungsgemeinschaft (DFG). This work is also part of the MaxSynBio consortium, which is jointly funded by the Federal Ministry of Education and Research of Germany and the Max Planck Society. M.H. gratefully acknowledges support from the Joachim Herz Foundation.

■ REFERENCES

- (1) Schwille, P. Bottom-up synthetic biology: engineering in a tinkerer's world. *Science* **2011**, 333 (6047), 1252–1254.
- (2) Forster, A. C.; Church, G. M. Towards synthesis of a minimal cell. *Mol. Syst. Biol.* **2006**, 2 (1), 45.
- (3) Vogel, S. K.; Greiss, F.; Khmelinskaia, A.; Schwille, P. Control of lipid domain organization by a biomimetic contractile actomyosin cortex. *eLife* **2017**, 6, e24350.
- (4) Loose, M.; Mitchison, T. J. The bacterial cell division proteins FtsA and FtsZ self-organize into dynamic cytoskeletal patterns. *Nat. Cell Biol.* **2014**, 16 (1), 38–46.
- (5) Osawa, M.; Anderson, D. E.; Erickson, H. P. Reconstitution of contractile FtsZ rings in liposomes. *Science* **2008**, 320 (5877), 792–794.
- (6) Schweizer, J.; Loose, M.; Bonny, M.; Kruse, K.; Mönch, I.; Schwille, P. Geometry sensing by self-organized protein patterns. *Proc. Natl. Acad. Sci. U. S. A.* **2012**, 109 (38), 15283–15288.
- (7) Shcherbakova, D. M.; Shemetov, A. A.; Kaberniuk, A. A.; Verkhusa, V. V. Natural photoreceptors as a source of fluorescent proteins, biosensors, and optogenetic tools. *Annu. Rev. Biochem.* **2015**, 84, 519–550.

- (8) Bacchus, W.; Fussenegger, M. The use of light for engineered control and reprogramming of cellular functions. *Curr. Opin. Biotechnol.* **2012**, *23* (5), 695–702.
- (9) Caldwell, R. M.; Bermudez, J. G.; Thai, D.; Aonbangkhen, C.; Schuster, B. S.; Courtney, T.; Deiters, A.; Hammer, D. A.; Chenoweth, D. M.; Good, M. C. Optochemical Control of Protein Localization and Activity within Cell-like Compartments. *Biochemistry* **2018**, *57* (18), 2590–2596.
- (10) Strale, P. O.; Azioune, A.; Bugnicourt, G.; Lecomte, Y.; Chahid, M.; Studer, V. Multiprotein Printing by Light-Induced Molecular Adsorption. *Adv. Mater.* **2016**, *28* (10), 2024–2029.
- (11) Gatterdam, V.; Ramadass, R.; Stoess, T.; Fichte, M. A.; Wachtveitl, J.; Heckel, A.; Tampé, R. Three-Dimensional Protein Networks Assembled by Two-Photon Activation. *Angew. Chem., Int. Ed.* **2014**, *53* (22), 5680–5684.
- (12) Fichte, M. A.; Weyel, X. M.; Junek, S.; Schäfer, F.; Herbivo, C.; Goeldner, M.; Specht, A.; Wachtveitl, J.; Heckel, A. Three-Dimensional Control of DNA Hybridization by Orthogonal Two-Color Two-Photon Uncaging. *Angew. Chem.* **2016**, *128* (31), 9094–9098.
- (13) Labòria, N.; Wieneke, R.; Tampé, R. Control of nanomolar interaction and in situ assembly of proteins in four dimensions by light. *Angew. Chem., Int. Ed.* **2013**, *52* (3), 848–853.
- (14) Rudd, A. K.; Valls Cuevas, J. M.; Devaraj, N. K. SNAP-tag-reactive lipid anchors enable targeted and spatiotemporally controlled localization of proteins to phospholipid membranes. *J. Am. Chem. Soc.* **2015**, *137* (15), 4884–4887.
- (15) Chen, X.; Venkatachalapathy, M.; Kamps, D.; Weigel, S.; Kumar, R.; Orlich, M.; Garrecht, R.; Hirtz, M.; Niemeyer, C. M.; Wu, Y. W.; et al. Molecular Activity Painting[®]: Switch-like, Light-Controlled Perturbations inside Living Cells. *Angew. Chem., Int. Ed.* **2017**, *56* (21), 5916–5920.
- (16) Bartelt, S. M.; Chervyachkova, E.; Steinkühler, J.; Ricken, J.; Wieneke, R.; Tampé, R.; Dimova, R.; Wegner, S. V. Dynamic blue light-switchable protein patterns on giant unilamellar vesicles. *Chem. Commun.* **2018**, *54* (8), 948–951.
- (17) Uda, Y.; Goto, Y.; Oda, S.; Kohchi, T.; Matsuda, M.; Aoki, K. Efficient synthesis of phycocyanobilin in mammalian cells for optogenetic control of cell signaling. *Proc. Natl. Acad. Sci. U. S. A.* **2017**, *114* (45), 11962–11967.
- (18) Sawa, M.; Nusinow, D. A.; Kay, S. A.; Imaizumi, T. FKF1 and GIGANTEA complex formation is required for day-length measurement in *Arabidopsis*. *Science* **2007**, *318* (5848), 261–265.
- (19) Kennedy, M. J.; Hughes, R. M.; Peteya, L. A.; Schwartz, J. W.; Ehlers, M. D.; Tucker, C. L. Rapid blue-light-mediated induction of protein interactions in living cells. *Nat. Methods* **2010**, *7* (12), 973.
- (20) Guntas, G.; Hallett, R. A.; Zimmerman, S. P.; Williams, T.; Yumerefendi, H.; Bear, J. E.; Kuhlman, B. Engineering an improved light-induced dimer (iLID) for controlling the localization and activity of signaling proteins. *Proc. Natl. Acad. Sci. U. S. A.* **2015**, *112* (1), 112–117.
- (21) Kawano, F.; Suzuki, H.; Furuya, A.; Sato, M. Engineered pairs of distinct photoswitches for optogenetic control of cellular proteins. *Nat. Commun.* **2015**, *6*, 6256.
- (22) Redchuk, T. A.; Omelina, E. S.; Chernov, K. G.; Verkhusha, V. V. Near-infrared optogenetic pair for protein regulation and spectral multiplexing. *Nat. Chem. Biol.* **2017**, *13*, 633.
- (23) Levsikaya, A.; Weiner, O. D.; Lim, W. A.; Voigt, C. A. Spatiotemporal control of cell signalling using a light-switchable protein interaction. *Nature* **2009**, *461* (7266), 997–1001.
- (24) Ni, M.; Tepperman, J. M.; Quail, P. H. Binding of phytochrome B to its nuclear signalling partner PIF3 is reversibly induced by light. *Nature* **1999**, *400* (6746), 781–784.
- (25) Shimizu-Sato, S.; Huq, E.; Tepperman, J. M.; Quail, P. H. A light-switchable gene promoter system. *Nat. Biotechnol.* **2002**, *20* (10), 1041–1044.
- (26) Müller, K.; Engesser, R.; Metzger, S.; Schulz, S.; Kämpf, M. M.; Busacker, M.; Steinberg, T.; Tomakidi, P.; Ehrbar, M.; Nagy, F.; et al. A red/far-red light-responsive bi-stable toggle switch to control gene expression in mammalian cells. *Nucleic Acids Res.* **2013**, *41* (7), e77–e77.
- (27) Tyszkiewicz, A. B.; Muir, T. W. Activation of protein splicing with light in yeast. *Nat. Methods* **2008**, *5* (4), 303–305.
- (28) Leung, D. W.; Otomo, C.; Chory, J.; Rosen, M. K. Genetically encoded photoswitching of actin assembly through the Cdc42-WASP-Arp2/3 complex pathway. *Proc. Natl. Acad. Sci. U. S. A.* **2008**, *105* (35), 12797–12802.
- (29) Toettcher, J. E.; Gong, D.; Lim, W. A.; Weiner, O. D. Light-based feedback for controlling intracellular signaling dynamics. *Nat. Methods* **2011**, *8* (10), 837–839.
- (30) Ni, M.; Tepperman, J. M.; Quail, P. H. Binding of phytochrome B to its nuclear signalling partner PIF3 is reversibly induced by light. *Nature* **1999**, *400* (6746), 781.
- (31) Levsikaya, A.; Weiner, O. D.; Lim, W. A.; Voigt, C. A. Spatiotemporal control of cell signalling using a light-switchable protein interaction. *Nature* **2009**, *461* (7266), 997.
- (32) Matsushita, T.; Mochizuki, N.; Nagatani, A. Dimers of the N-terminal domain of phytochrome B are functional in the nucleus. *Nature* **2003**, *424* (6948), 571.
- (33) Müller, K.; Zurbriggen, M. D.; Weber, W. Control of gene expression using a red-and far-red light-responsive bi-stable toggle switch. *Nat. Protoc.* **2014**, *9* (3), 622.
- (34) Nye, J. A.; Groves, J. T. Kinetic control of histidine-tagged protein surface density on supported lipid bilayers. *Langmuir* **2008**, *24* (8), 4145–4149.
- (35) Kubalek, E. W.; Le Grice, S. F.; Brown, P. O. Two-dimensional crystallization of histidine-tagged, HIV-1 reverse transcriptase promoted by a novel nickel-chelating lipid. *J. Struct. Biol.* **1994**, *113* (2), 117–123.
- (36) You, C.; Piehler, J. Multivalent chelators for spatially and temporally controlled protein functionalization. *Anal. Bioanal. Chem.* **2014**, *406* (14), 3345–3357.
- (37) Frick, M.; Schmidt, K.; Nichols, B. J. Modulation of lateral diffusion in the plasma membrane by protein density. *Curr. Biol.* **2007**, *17* (5), 462–467.
- (38) Alenghat, F. J.; Golan, D. E. Membrane protein dynamics and functional implications in mammalian cells. In *Current Topics in Membranes*; Elsevier, 2013; Vol. 72, pp 89–120.
- (39) Burgie, E. S.; Bussell, A. N.; Walker, J. M.; Dubiel, K.; Vierstra, R. D. Crystal structure of the photosensing module from a red/far-red light-absorbing plant phytochrome. *Proc. Natl. Acad. Sci. U. S. A.* **2014**, *111*, 201403096.
- (40) Galush, W. J.; Nye, J. A.; Groves, J. T. Quantitative fluorescence microscopy using supported lipid bilayer standards. *Biophys. J.* **2008**, *95* (5), 2512–2519.
- (41) Bisson-Filho, A. W.; Hsu, Y.-P.; Squyres, G. R.; Kuru, E.; Wu, F.; Jukes, C.; Sun, Y.; Dekker, C.; Holden, S.; VanNieuwenhze, M. S.; et al. Treadmilling by FtsZ filaments drives peptidoglycan synthesis and bacterial cell division. *Science* **2017**, *355* (6326), 739–743.
- (42) Erickson, H. P.; Taylor, D. W.; Taylor, K. A.; Bramhill, D. Bacterial cell division protein FtsZ assembles into protofilament sheets and minirings, structural homologs of tubulin polymers. *Proc. Natl. Acad. Sci. U. S. A.* **1996**, *93* (1), 519–523.
- (43) Lu, C.; Reedy, M.; Erickson, H. P. Straight and curved conformations of FtsZ are regulated by GTP hydrolysis. *J. Bacteriol.* **2000**, *182* (1), 164–170.
- (44) Pichoff, S.; Lutkenhaus, J. Unique and overlapping roles for ZipA and FtsA in septal ring assembly in *Escherichia coli*. *EMBO J.* **2002**, *21* (4), 685–693.
- (45) Pichoff, S.; Lutkenhaus, J. Tethering the Z ring to the membrane through a conserved membrane targeting sequence in FtsA. *Mol. Microbiol.* **2005**, *55* (6), 1722–1734.
- (46) Hale, C. A.; de Boer, P. A. Direct binding of FtsZ to ZipA, an essential component of the septal ring structure that mediates cell division in *E. coli*. *Cell* **1997**, *88* (2), 175–185.
- (47) Ortiz, C.; Natale, P.; Cueto, L.; Vicente, M. The keepers of the ring: regulators of FtsZ assembly. *FEMS Microbiol. Rev.* **2016**, *40* (1), 57–67.

(48) Haeusser, D. P.; Margolin, W. Splitsville: structural and functional insights into the dynamic bacterial Z ring. *Nat. Rev. Microbiol.* **2016**, *14* (5), 305–319.

(49) Moran, U.; Phillips, R.; Milo, R. SnapShot: key numbers in biology. *Cell* **2010**, *141* (7), 1262–1262.

(50) Ramirez-Diaz, D. A.; García-Soriano, D. A.; Raso, A.; Mücksch, J.; Feingold, M.; Rivas, G.; Schwille, P. Treadmilling analysis reveals new insights into dynamic FtsZ ring architecture. *PLoS Biol.* **2018**, *16* (5), e2004845.

(51) Xu, T.; Vavylonis, D.; Tsai, F.-C.; Koenderink, G. H.; Nie, W.; Yusuf, E.; Lee, I.-J.; Wu, J.-Q.; Huang, X. SOAX: A software for quantification of 3D biopolymer networks. *Sci. Rep.* **2015**, *5*, 9081.

(52) Bélisle, J. M.; Correia, J. P.; Wiseman, P. W.; Kennedy, T. E.; Costantino, S. Patterning protein concentration using laser-assisted adsorption by photobleaching, LAPAP. *Lab Chip* **2008**, *8* (12), 2164–2167.

(53) Hong, S.; Zhu, J.; Mirkin, C. A. Multiple ink nanolithography: toward a multiple-pen nano-plotter. *Science* **1999**, *286* (5439), 523–525.

(54) Scott, M. A.; Wissner-Gross, Z. D.; Yanik, M. F. Ultra-rapid laser protein micropatterning: screening for directed polarization of single neurons. *Lab Chip* **2012**, *12* (12), 2265–2276.

(55) Théry, M. Micropatterning as a tool to decipher cell morphogenesis and functions. *J. Cell Sci.* **2010**, *123* (24), 4201–4213.

(56) Martin, T. A.; Herman, C. T.; Limpoco, F. T.; Michael, M. C.; Potts, G. K.; Bailey, R. C. Quantitative photochemical immobilization of biomolecules on planar and corrugated substrates: a versatile strategy for creating functional biointerfaces. *ACS Appl. Mater. Interfaces* **2011**, *3* (9), 3762–3771.

(57) Falconnet, D.; Csucs, G.; Grandin, H. M.; Textor, M. Surface engineering approaches to micropattern surfaces for cell-based assays. *Biomaterials* **2006**, *27* (16), 3044–3063.

(58) Reuther, C.; Tucker, R.; Ionov, L.; Diez, S. Programmable patterning of protein bioactivity by visible light. *Nano Lett.* **2014**, *14* (7), 4050–4057.

Supporting Material for

Light-induced Printing of Protein Structures on Membranes *in vitro*

Haiyang Jia¹, Lei Kai¹, Michael Heymann¹, Daniela A. Garcia-Soriano^{1,2}, Tobias Härtel¹, Petra Schwille^{1,*}

¹ Max Planck Institute of Biochemistry, Am Klopferspitz 18, D-82152 Martinsried, Germany.

²Graduate School for Quantitative Biosciences (QBM), Ludwig-Maximilians-University,
Munich, Germany

*Corresponding author: Petra Schwille, schwille@biochem.mpg.de

This PDF file includes

Materials and Methods

Supplement figure S1 to S12

Table S1 to S2

Other Supporting Online Material for this manuscript includes the following:

Movies S1 to S5

References

Materials and Methods

Protein Expression and Purification

Pcoofy12-onestrep-PhyB621-mcherry-His6(*PhyB* genebank id: NC_003071.7; pCoofy12 plasmid¹) encodes the PhyB(1-621)-mCherry construct bearing N-streptag and C-terminal His6 tags was transformed into *Escherichia coli* BL21-star cells. Cells were induced with 1mM IPTG at OD_{600nm} = 0.6 and cultured overnight at 18°C. Cell pellets were collected via centrifugation at 6000g for 15 min and washed 3 times with buffer PBS(pH7.4). The resulting pellet was resuspended with lysis buffer, which included 50mM HEPES-NaOH (pH 7.8), 500mM NaCl, 10% glycerol, 30mM imidazole, 1mM phenylmethanesulfonyl fluoride(PMSF), 1mM 2-Mercaptoethanol, 1 tablet/liter Roche EDTA-free complete protease inhibitor. Then the cells were lysed with French press(G.HEINEMANN,) at 17,000 psi. Lysates were clarified by centrifugation (20000g) and the supernatant was filtered through a 0.22 µm membrane. The resulting filtered sample was loaded onto a Ni²⁺ affinity chromatography(GE Healthcare, HisTrap HP 5 ml) that was pre-equilibrated with washing buffer(50mM HEPES-NaOH (pH 7.8), 500mM NaCl, 10% glycerol, 30mM imidazole, 1mM 2-Mercaptoethanol, 1 tablet/liter Roche EDTA-free complete protease inhibitor). The protein was eluted with Lysis buffer supplemented with 300mM imidazole. Then the eluate was loaded onto the StrepTrap HP column(1 ml, GE Healthcare). Protein was eluted using a strep elution buffer containing 50mM HEPES-NaOH (pH 7.8), 500mM NaCl, 10% glycerol, 0.25mM desthiobiotin, 1mM 2-Mercaptoethanol, 1 tablet/liter Roche EDTA-free complete protease inhibitor. The eluate from the strep affinity purification was dialyzed into a buffer containing 50mM HEPES-NaOH (pH 7.8), 500mM NaCl, 10% glycerol, 1mM 2-Mercaptoethanol. Then the protein was stored with 50% glycerol at -80°C.

Pcoofy1-His6-HRV-EYFP-PIF6 (*PIF6* genebank id: NC_003074) encodes EYFP-PIF6 with N-terminal His-tag was transformed into *Escherichia coli* BL21-star cells. The culture condition and the buffers for Ni²⁺-NTA affinity purification are the same as that of PhyB (1-621)-mCherry. After affinity purification, the eluate was polished by the HiLoadtm 16/600 SuperdexTm 75pg (GE) column. Then the purified protein was incubated with the His-PreScission (3C) protease (in house prep.) to remove the N-terminal histidine tag. The sample mixture was passed through a Ni-NTA column again to remove uncleaved and protease. The purified protein without His tag was frozen with liquid nitrogen and stored at -80°C.

FtsZ (1-366)-YFP-PIF6, and wild type FtsZ were purified as previously described². Briefly, overexpressed cells were lysed and separated by centrifugation. Protein was precipitated from the supernatant by adding 30% saturated ammonium sulfate(4°C) and incubated for 20 min at 4°C (slow shaking). After centrifugation and resuspension of the pellet, the protein was purified by anion exchange chromatography using a 5x 5ml Hi-Trap Q-Sepharose column (GE Healthcare). Wild type FtsZ was labeled with Alexa fluor 488 according to the protocol provided by Thermo Fisher.

***In vitro* spectroscopy of phyB**

Spectra of dark-adapted and red-light irradiated PhyB-mCherry-His6(PCB) were collected using UV/VIS-Spectrophotometer V650. Samples were irradiated from the top by different wavelengths. The approximate intensity at the cuvette window was 0.3 mW. cm⁻². A single cuvette was used for all measurements, and was loaded with 200µl of PhyB-mCherry-His6 solution charged with 1.5µM phycocyanobilin(PCB: supply by Santa Cruz Biotechnology, Inc.). The PCB concentration was quantified by absorbance spectroscopy at 680nm diluting the DMSO stock 1:100 into 1mL MeOH:HCl(95%:5%) solution . The concentration in mM was calculated as A₆₈₀ *2.64. Typical stock concentrations were diluted to 1.5mM. Aliquots can be stored at -20°C for at least one year, when protected from light.

Preparation of liposomes.

Different concentration (0.05mol% to 34mol%) of DOGS-NTA(Ni) lipid with DOPC dissolved in chloroform were transferred into a glass vial and the solvent was evaporated under a gentle stream of nitrogen. All the lipids were purchased from Avanti Polar Lipids, Inc. Any residual solvent was further removed by drying the lipid film in a vacuum for 30 min. The lipids were then rehydrated in SLB buffer (50mM HEPES-NaOH at pH7.5, 500mM NaCl) to a lipid concentration of 4mgml⁻¹ and incubated at 37°C for 30 min. The lipid film was then completely resuspended by vortexing rigorously to obtain multilamellar vesicles of different sizes. This mixture was then placed in a bath sonicator where shear forces help to reduce the size of the vesicles, giving rise to small unilamellar vesicles (SUVs). The SUV dispersion were stored at -20°C as 20µl aliquots. In the paper, if without specifying, the composition of the SLB is 34mol% DOGS-NTA(Ni) and 66 mol% DOPC.

Preparation of supported lipid bilayers.

Glass coverslips (1.5#, 24x24mm) were cleaned by piranha solution overnight, followed by extensive washing with milliQ H₂O. Then glass coverslips were blown dry with compressed air and cleaned in an air plasma for 10 min. The reaction chamber was prepared by attaching a plastic ring on a cleaned glass coverslip using ultraviolet glue (Thorlabs No. 68). For supported lipid bilayer formation, the SUV dispersion was diluted in SLB buffer to 0.5mgml⁻¹, of which 75µl was added to the reaction chamber. Adding CaCl₂ to a final concentration of 3mM induced fusion of the vesicles and the formation of a lipid bilayer on coversilide. After 20 min of incubation at 37°C, the sample was rinsed with 2ml pre-warmed SLB buffer.

Measurement of protein pattern density on the membrane

The surface density of protein on supported membranes was measured using quantitative fluorescence microscopy³. First, 1mg/ml vesicles containing fluorescent lipids (BODIPYDHPE /R-DHPE, Invitrogen Corp.) at various concentrations (0.01-0.8 mol%) and DOPC (Avanti Polar Lipids) were generated by extrusion through 100-nm pore membrane. Average diameters of the resulting suspensions were typically within 5% of 100 nm as measured by dynamic light scattering.

Supported bilayers for calibration standards were formed in self-made chambers that had been plasma cleaned. Vesicle suspensions at 1 mg/ml in sample buffer (50 mM HEPES, 500 mM NaCl, pH 7.5) were added to an equal volume of buffer in the chamber. SLBs were generated following the normal protocol. For fluorescence intensity measurement, the microscope was focused on the surface of the SLB where intensity was maximal and images were taken at different areas (n>4). The same experiments were repeated with different bilayers at least three times. Bilayer fluorescence was plotted against the molecular density of fluorescent lipids per µm² that is calculated by using a DOPC lipid footprint in supported bilayers of 0.72 nm²⁴. These data were fit to a straight line with a y-intercept of 0; see supplement Figure S7:

$$D_{lipid} = I_{bilayer(lipid)} * I \quad E.1$$

Where D_{lipid} is the area density of fluorescent lipid. $I_{bilayer(lipid)}$ is the slope of the fitting curve. I is the measured lipid fluorescence intensity. The Equation E1 is only directly applicable to similar supported bilayers containing BODIPY-DHPE. Therefore, the calibration must be corrected for

different dyes to render them comparable to the standards. We can calibrate the intensity of the sample fluorophore to the bilayer standard fluorophore as:

$$I_{bilayer(lipid)} = I_{bilayer(sample)} / F \quad E.2$$

where $I_{bilayer(sample)}$ is the calibrated and observed sample intensity, and F is a unitless scaling factor that represents the strength of the sample fluorophore versus the lipid-linked standard fluorophore. F for a pair of fluorophores can be measured by the microscope as:

$$F = I_{solution(sample)} / I_{solution(lipid)} \quad E.3$$

where $I_{solution(sample)}$ and $I_{solution(lipid)}$ are the concentration-normalized intensities of the sample and lipid vesicle standard solutions, respectively. $I_{solution(sample)}$ and $I_{solution(lipid)}$ can be measured from a serial dilution of samples and lipid vesicle. The fluorescence signals were plotted against the concentration. The data were fit to a straight line with a y-intercept of 0 and the slopes were designated as $I_{solution(sample)}$ and $I_{solution(lipid)}$. Background signal was measured from solutions of nonfluorescent vesicles.

Global Recruitment Assays.

Global recruitment assays were performed at room temperature on a Zeiss LSM780 confocal. Images were captured with a CCD camera. The assays were done by exposing to activating (660nm) or deactivating (740nm) wavelengths by CoolLED PE4000. The Ni-NTA agarose beads (Qiagen) were blocked with 1% w/v BSA for more than 1 h. To measure kinetics of recruitment and release, the PhyB-mCherry-His6 was immobilized on the blocked Ni-NTA agarose beads (Qiagen) for 1 h and later incubated with 1.5 μ M PCB for another 1 h. Then the unbinding protein was washed away and incubated with EYFP-PIF6 in Biotek chamber. The chamber was exposed to fixed periods of red or infrared light, while the EYFP-PIF6 distribution was imaged. The PhyB-PIF6 pool was returned to equilibrium (fully recruited or released) by exposure to the respective wavelengths in a loop. Such iterative measurements are necessary to eliminate the strong activating perturbations induced by the imaging light. Using red light mediated activation is highly sensitive and about 0.3mWcm⁻² at 660nm (2% 193mW) (measured with optical power meter PM100D, Thorlabs), is sufficient to drive rapid protein-to-protein interaction. The on and off plots of the fluorescence translocation assay were fitted with mono-exponential equation using Originpro 2017:

$$Y = Ae^{-kt} + B, \quad E.4$$

where Y represents fluorescence intensity at time t , A and B are parameters, and k represents the rate constant. The half-life, $t_{1/2}$, was determined using the following equation:

$$t_{1/2} = \ln 2 \ k^{-1} \quad \text{E.5}$$

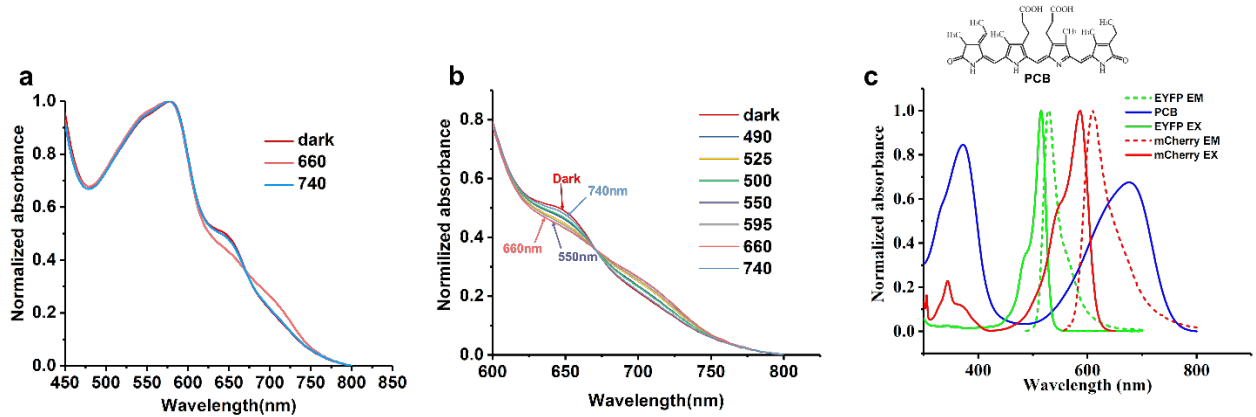
Protein Patterning on SLB

Printing protein patterns on SLB was performed at room temperature using confocal microscopy equipped with an argon laser and C-Apochromat 40x/1.20 water-immersion objective. Laser lines 488nm, and 514nm and 561nm lasers were used for fluorescence imaging. To produce patterns on the membrane, alternating 561nm and 633nm laser were used for photoactivation. The deactivation light (740nm) was provided with CoolLED. Images were collected with the CCD camera. The light pattern used for activation were drawn with the ZEN software. The Einstein's template pattern was modified from the pixel picture (<http://lego-art-studio.blogspot.com/>) with ZEN software.

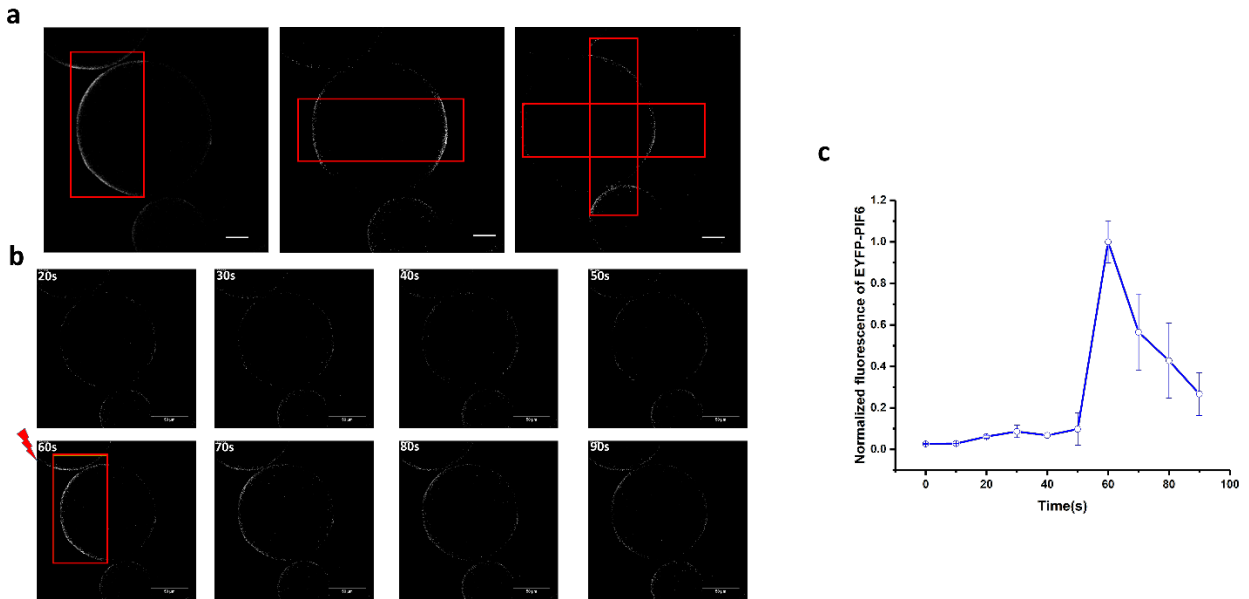
Image analysis and Repeatability of experiments.

Image analysis and processing was carried out with Fiji⁵. The frames of time-lapse movies were normalized to have a constant overall intensity. The number of replicated experiments is given in the respective figure captions. Representative micrographs and intensity curves correspond to at least four successfully repeated experiments. The FtsZ network was analyzed with Stretching Open Active Contours (SOAX)⁶. In order to analyze the architecture of the network, thresholds for FtsZ filament length (from 100nm to persistence length of 1.15 μm ⁷) and fluorescence intensity thresholds were introduced to decrease the noise caused by unspecific binding and aggregates. Large clusters of aggregates (diameter $1 > \mu\text{m}$)⁸ were not considered in the analysis.

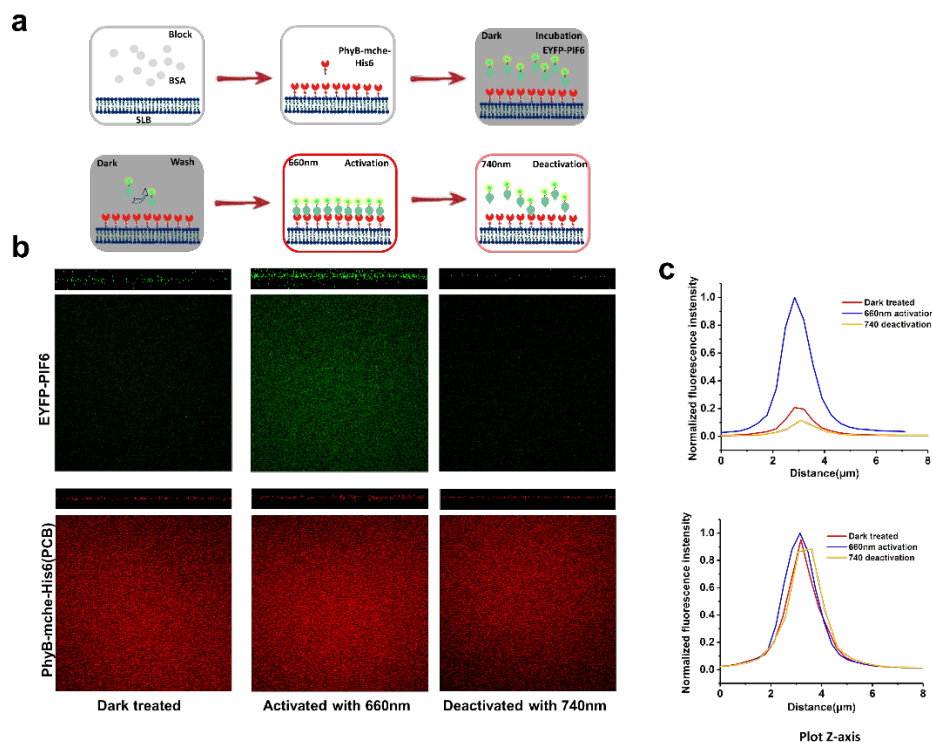
Supplement figures



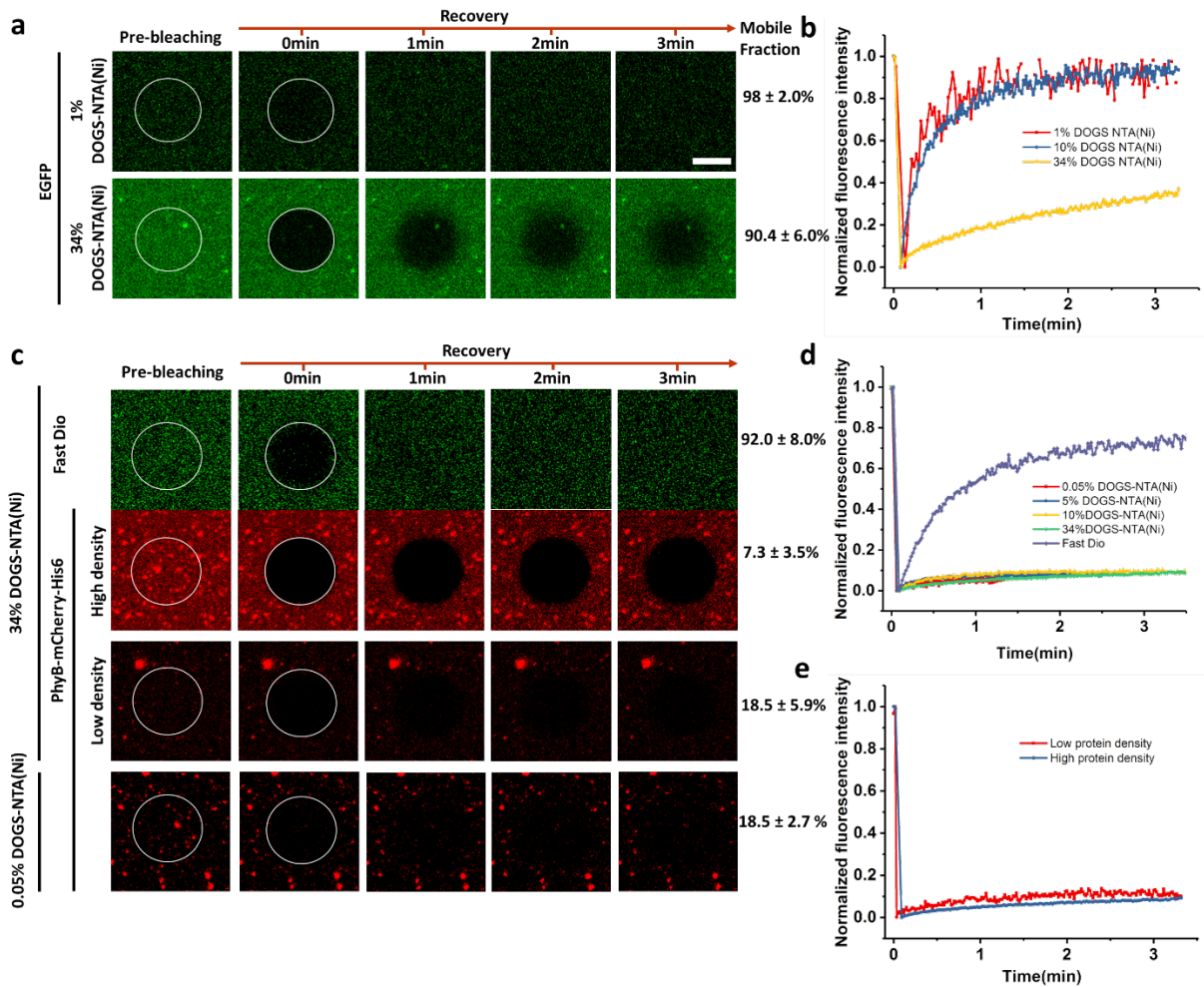
Supplement figure S1. a) The absorbance spectra of the PhyB-mCherry-His6(PCB) samples that were incubated in darkness, exposed to continuous red light (660nm) and far red light (740nm) to reach a steady state. b) The absorbance of PhyB-mCherry-His6 (PCB), after activation with 490nm, 525nm, 500nm, 550nm, 595nm, 660nm and 740nm. c) The spectra of mCherry, EYFP and PCB.



Supplement figure S2. a.) Reversible spatial recruitment of EYFP-PIF6 protein to the specific localization on the beads with 561 nm laser and 740nm LED light source. b) Time lapse images of reversible spatial recruitment c) Quantification of the fluorescence changing on the bead during activation and deactivation. The scale bar is 50 μ m. For a full sequence, see Supplementary Movie S2.



Supplement figure S3. Global light induced on- and off- recruitment on the SLB a) Illustration of the global activation process. Firstly, Ni-NTA lipid SLB was blocked with 1% w/v BSA for 1h. After washing with the SLB buffer, SLB was saturated with PhyB-mCherry-His6 protein and incubated with 1.5μM PCB for another 1h in the dark environment. The fluorescence images were taken after washing in a z-stack, showing in the b (left). A few EYFP proteins bound to the membrane, because the incubation process was not completely in dark environment. When the incubation was under red light (660nm), after washing, the homogeneous EYFP-PIF6 protein layer was recruited to the membrane (Figure b, middle). Followed by deactivation with far-red light (740nm), all the recruited protein was released to the bulk solution. c) Plots of fluorescence intensity for all the activation and deactivation processes in z-stack.

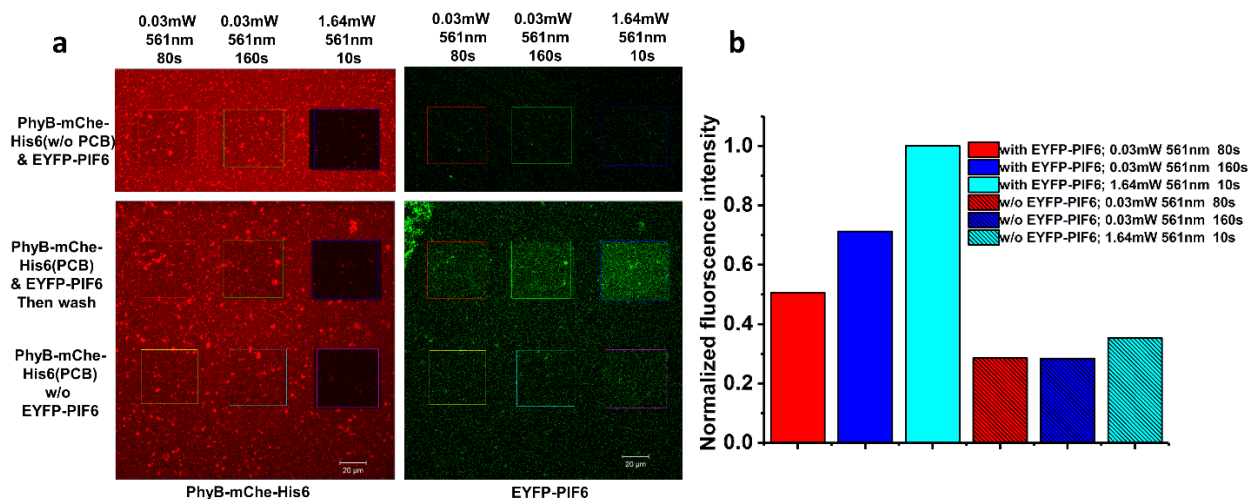


Supplement figure S4. Nearly static PhyB-mCherry-His6 layer on the membrane does not affect the fluidity of the membrane. a-b.) Immobilizing EGFP on SLBs that were composed of different mole fractions of DOGS-NTA(Ni) lipid from 1mol% to 34mol% ($1\mu\text{M}$ EGFP for incubation). The results show that although high concentrations of NTA lipid reduces their mobility, EGFP on SLBs maintains a high mobile fraction. c-e.) Immobilization of PhyB-mCherry-His6 on SLBs composed of different mole fractions of DOGS-NTA(Ni) lipid from 0.05% to 34% ($1\mu\text{M}$ PhyB-mCherry-His6 for incubation). The immobilized PhyB-mCherry-His6 layer showed low mobile behavior, even at low protein density (< 150 molecules/ μm^2) on the membrane, controlled either with low concentration NTA(Ni) lipid (0.05%) or low protein concentration (5nM PhyB-mCherry-His6). To confirm whether the PhyB-mCherry-His6 layer will affect the fluidity, the normal SLB composition (DOPC and DOGS-NTA(Ni)) was mixed with 0.01mol% Fast DiO. Scale bar, $5\mu\text{m}$. Fluorescence recovery after photobleaching data (FRAP) on the SLB were evaluated by choosing

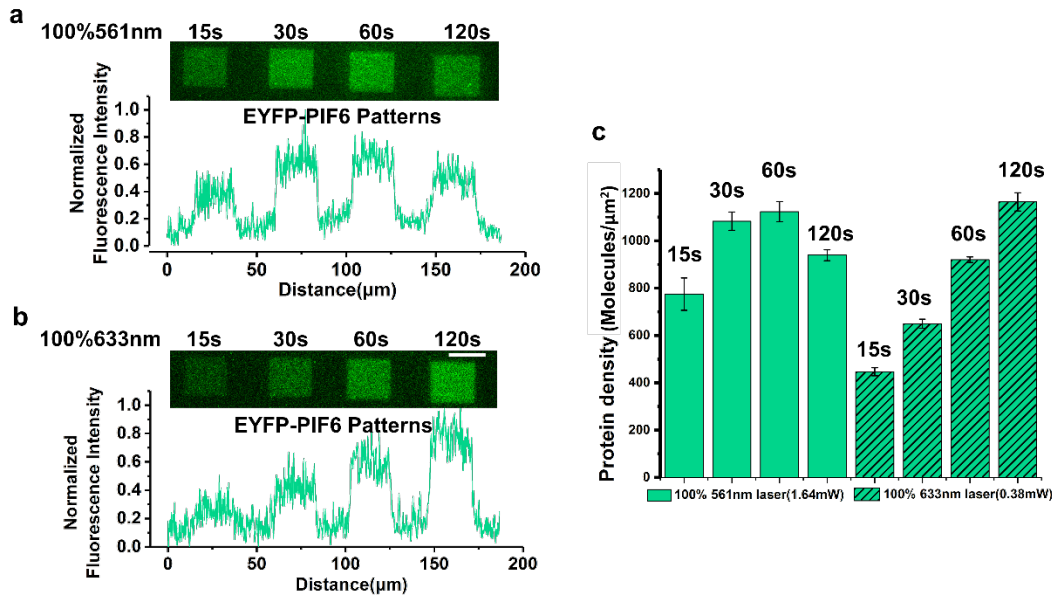
two separately circle areas ($r= 4\mu\text{m}$). One circle was taken as a reference. Another one was photobleached by 20 iterations of 488nm and 561nm, respectively, laser under 100% laser power. Their fluorescence recovery in the red and green channels, respectively, was monitored. Intensity traces were collected using Fiji, corrected for photobleaching and normalized with the pre-bleaching intensity and the reference intensity. The fluorescence recovery curves were then fitted by:

$$F(t)=y_0+A(e^{-2T/t})[I_0(2T/t)+I_1(2T/t)] \quad \text{E.6}$$

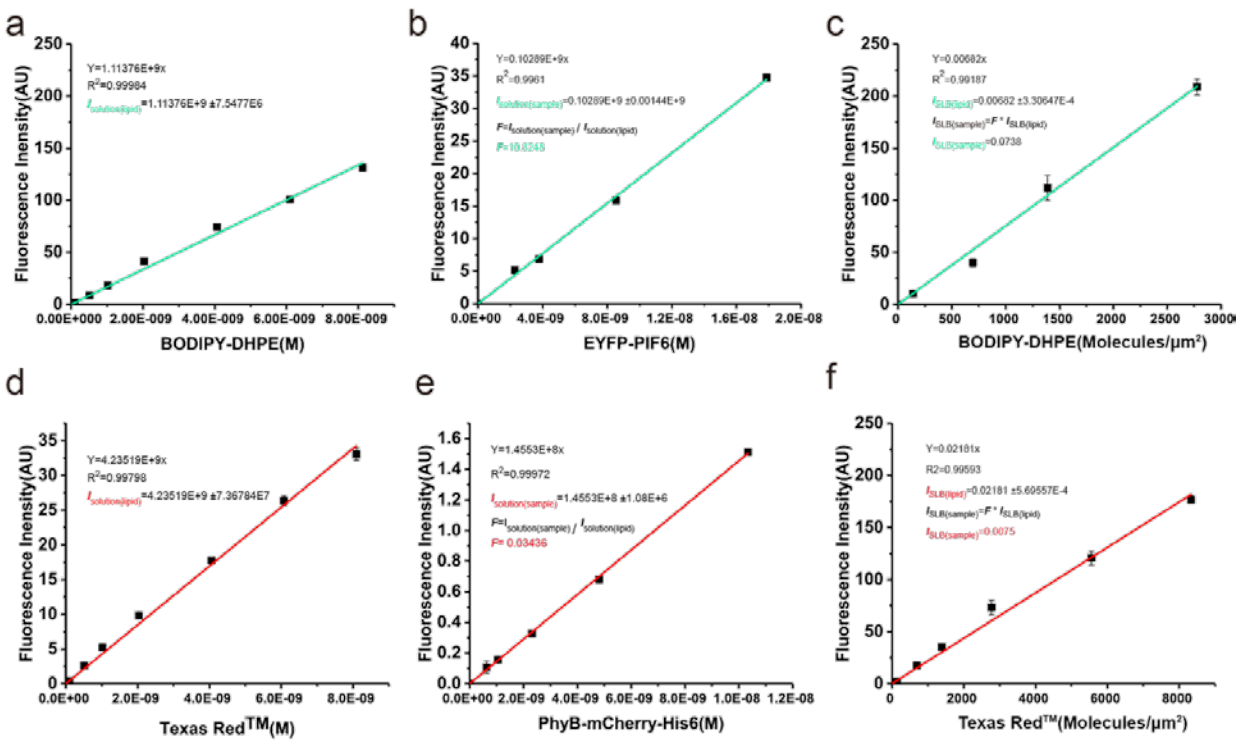
Here, I_0 , I_1 are modified Bessel functions, y_0 sets the fluorescence directly after bleaching and y_0+A determines the mobile fraction.



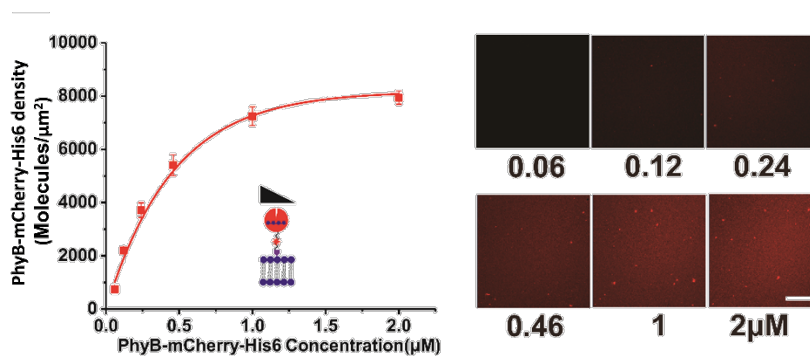
Supplement figure S5. Protein pattern printing on SLB with 561nm laser. a) The light induced printing was verified by multiple control experiments. The top row is the control experiment without light sensitive chemical (PCB). The middle row shows how different laser intensity and different bleaching change the amount of protein recruitment. The bottom row experiment was done without ligand protein (EYFP-PIF6). Only when PhyB-mCherry-His6 was charged with PCB and incubated with EYFP-PIF6 can the protein printing be performed on the SLB. b) Quantification of the printed pattern. The fluorescence intensity was measured and normalized with Fiji.



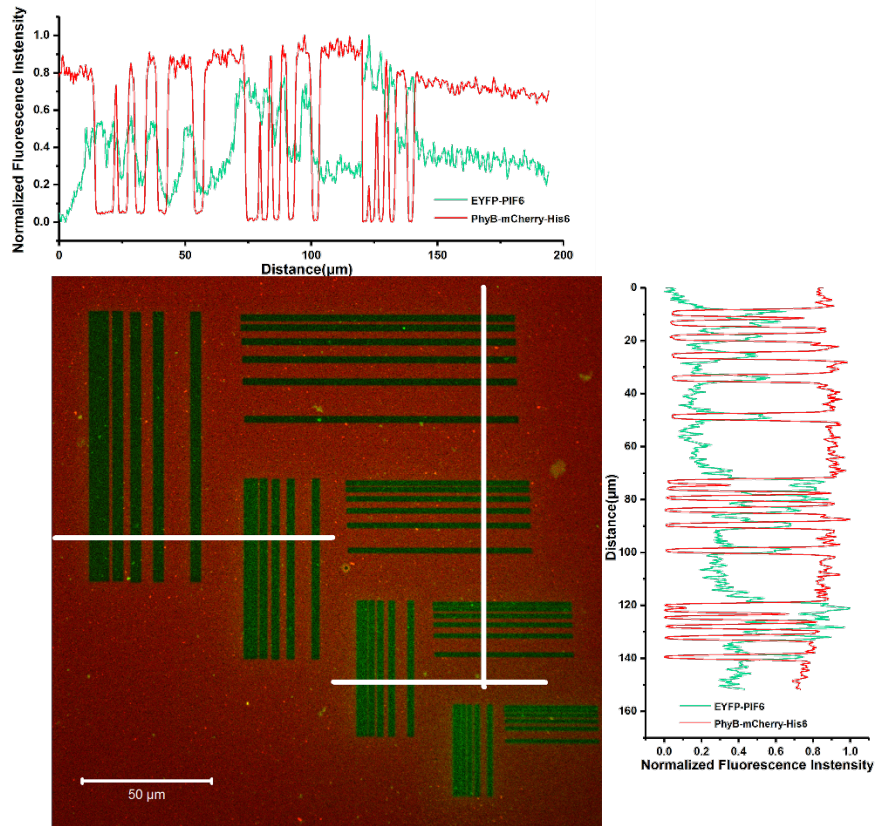
Supplement figure S6. a-b.) Both 561nm and 633 nm laser can be used for protein printing. c.) Protein density of patterns printed with 561nm and 633nm laser. Because the energy of 633nm laser is lower than the 561nm laser, longer activation was needed for printing for the former.



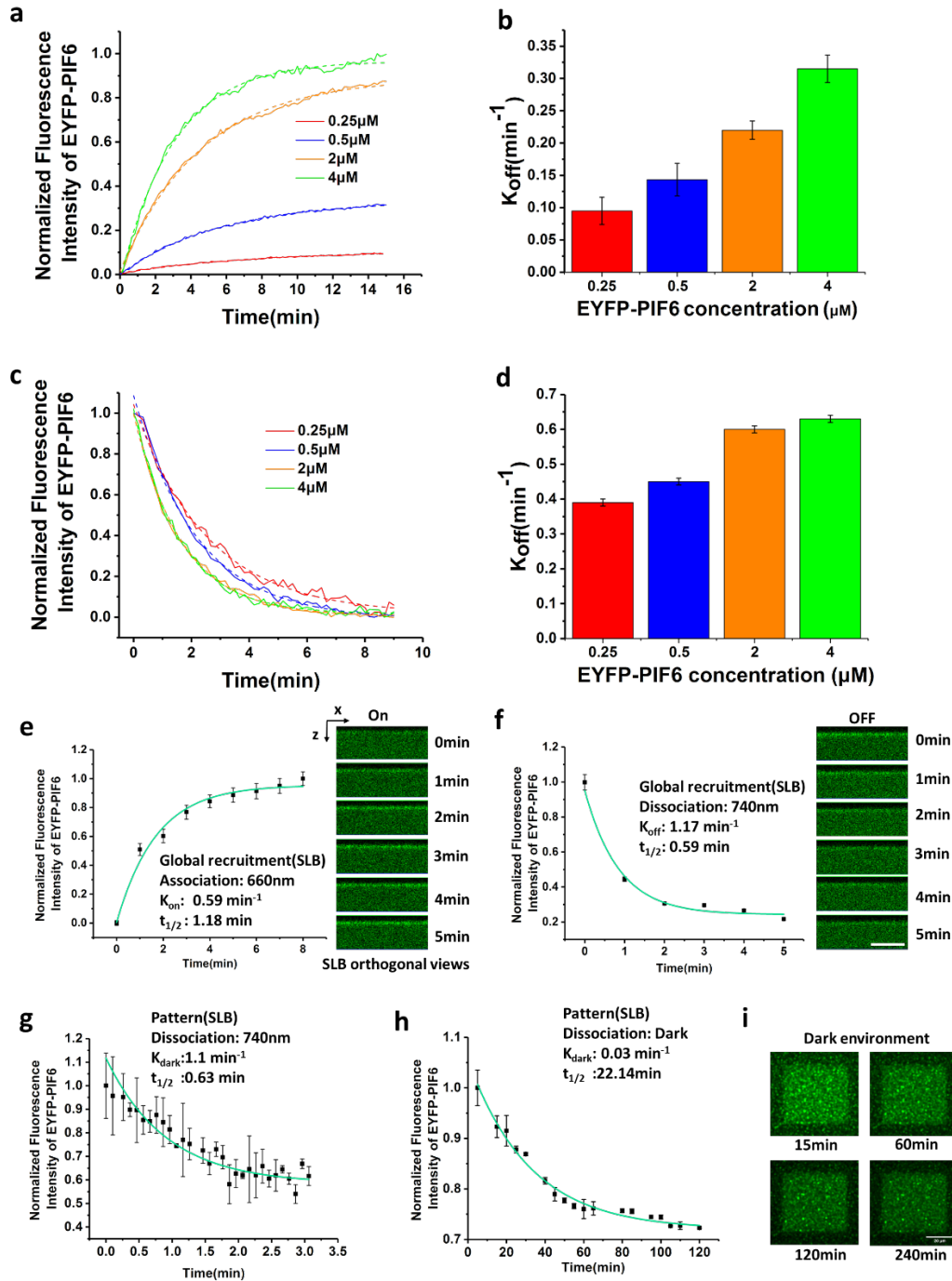
Supplement figure S7. Fluorescence calibration. a.) Fluorescence measured by confocal microscope in the green channel with increasing amounts of BODIY-DHPE in solution. b.) A calibration plot indicating the fluorescence intensities in solutions containing EYFP-PIF6. c.) SLB containing BODIY-DHPE was used as a surface density calibration standard. d.) Fluorescence in green channel with increasing amount of Texas RedTM in solution. e.) A calibration plot indicating the fluorescence intensities in solution containing PhyB-mCherry-His6. f.) SLB containing Texas RedTM was used as a surface density calibration standard.



Supplement figure S8. Plots of molecular density when SLBs were incubated with different concentrations of PhyB-mCherry-His6. The SLB composition used in the experiment was 34mol% DOGS-NTA and 66mol% DOPC. The error bars represent the mean value and standard deviation of the three independent experiments. The plots were fitted with BoxLucas model. The scale bar of the representative image is 50μm.

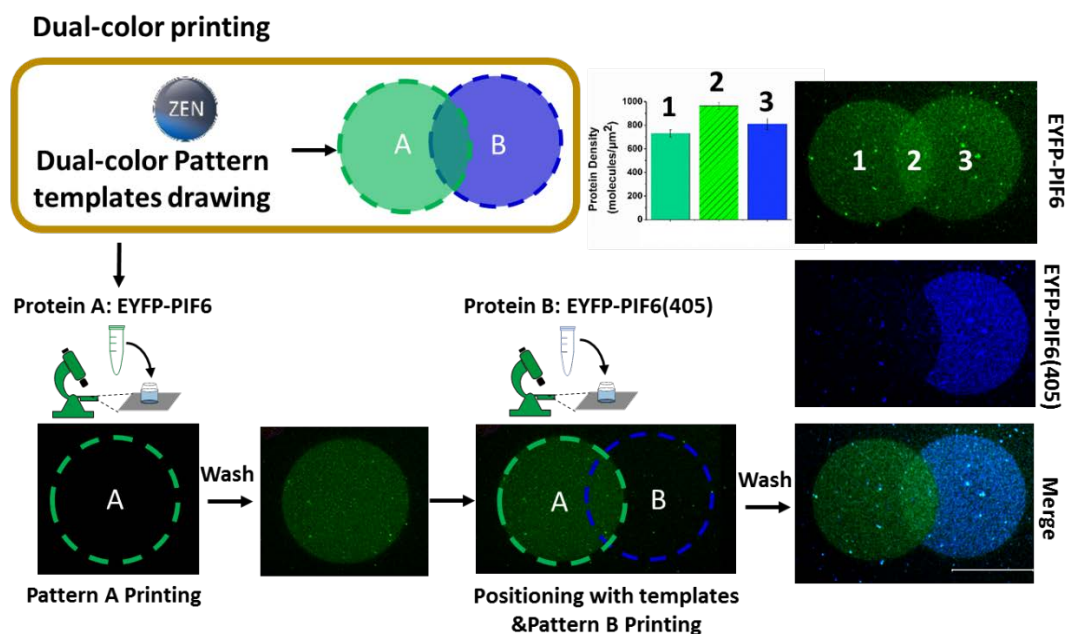


Supplement figure S9. Image of a resolution target produced by confocal microscopy with a Zeiss C-Apochromat 40x/1.20 water-immersion objective. The 6 lines were separated by about 1.5 μm , 3 μm , 4 μm , 6 μm and 12 μm in zoom 1. The line groups were printed in X or Y direction to evaluate the lateral resolution. Then the printing was performed with zoom 1, 1.5, 2 and 3. Average linear profiles of this region show that it is possible to resolve individual lines separated by about 0.5 μm (X) and 1 μm (Y).

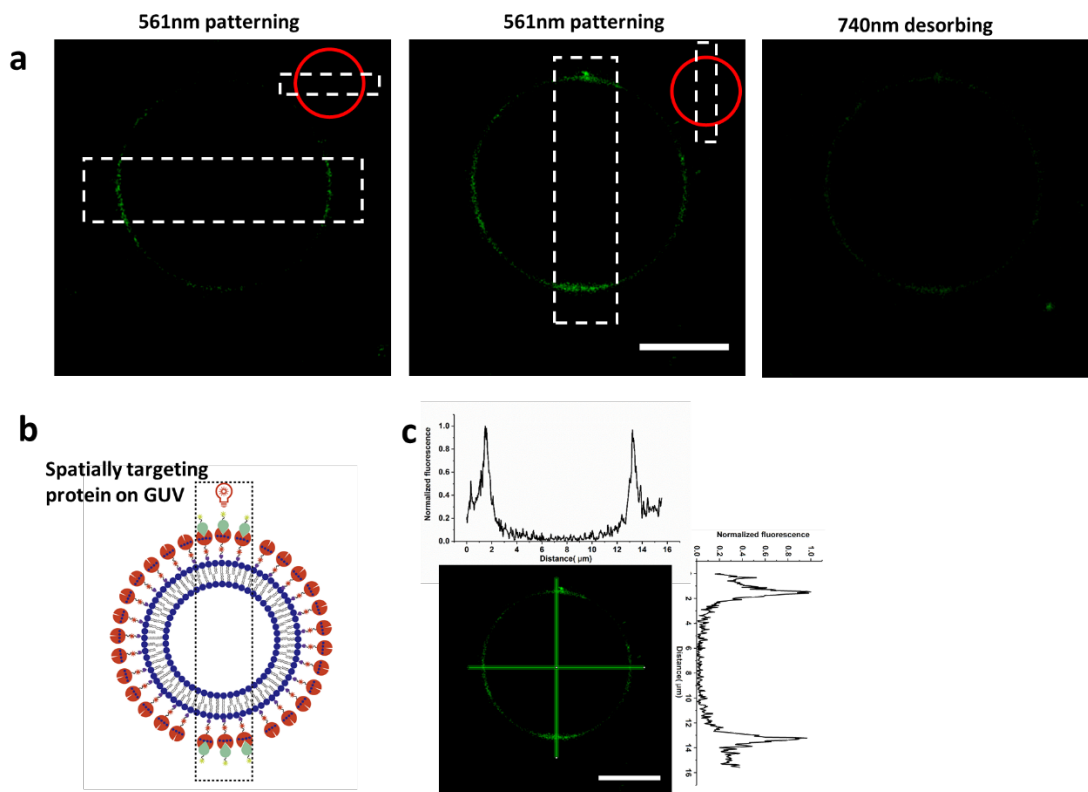


Supplement Figure S10. Light induced dynamics on NTA-Agarose beads and SLBs. a.) Real-time light induced responses of PhyB-mCherry-His6 and EYFP-PIF6 association on beads. The measured fluorescence was normalized by subtracting the original fluorescence before light activation and then all the data of curves were further normalized to [0, 1]. b.) Association rates versus EYFP-PIF6 concentration. c.) Real-time light induced responses of PhyB-mCherry-His6

and EYFP-PIF6 dissociation. The measured fluorescence was normalized to [0, 1]. d.) Dissociation rates versus EYFP-PIF6 concentration. In a. and c., each curve represents the measurement of a different EYFP-PIF6 concentration from the same batch of PhyB-mCherry-His6 coating beads. The binding curves were fitted with equation E.4. Dashed lines represent the fits. e-f.) Light induced activation PhyB-mCherry-His6 and EYFP-PIF6 association on SLB (34mol%DOGS-NTA(Ni), 66mol%DOPC). g.-h.) Pattern dissociation on SLB under 740nm and dark environment. EYFP-PIF6: 8 μ M. Scale bar, 20 μ m. i.) The persistence of the light-printed pattern on SLB (34mol%DOGS-NTA(Ni), 66mol%DOPC), scale bar, 20 μ m. The pattern can be maintained without obvious blur for at least four hours.



Supplement figure S11. Dual-color & multi-color printing. The dual-color template was split by ZEN software routine into two sequentially printed patterns. After each printing step (A,B), the unbound proteins were removed by rinsing. After the different printing steps, an integrated dual-color pattern could be obtained. In principle, the two-color printing can be further extended to multi-color. Different protein patterns may have regions of overlap; however, the first pattern will occupy the binding sites first. The density of either protein in the overlap region can be regulated by laser intensity and protein concentration. EYFP-PIF6: 4 μ M. EYFP-PIF6(Alexa fluor 405 NHS Ester): 4 μ M. Laser power: 100% 561nm laser(1.6mW). Activation time: 10s. Scale bar: 50 μ m.



Supplement figure S12. Controlling protein localization on GUVs with light. a.) Reversibly positioning EYFP-PIF6 on the GUV with 561nm illumination. The patterns can be dissolved with 740nm light. b.) Schematic of the patterning principle. c.) Line plots of the patterns on GUV. GUVs were prepared according to the published protocol⁹. GUVs (30mol%DOGS-NTA(Ni), 70mol%DOPC) were incubated with PhyB-mCherry-His6 (2 μ M) and PCB(1.5 μ M) for 1h. After coating the GUVs with PhyB-mCherry-His6(PCB), the buffer was diluted about 100 times, in order to decrease the concentration of the free PhyB-mCherry-His6(PCB) in the solution. Further, the patterns were printed by incubating with 1 μ M EYFP-PIF6. Scale bars in a. and c., 5 μ m.

Supplementary Table

Supplementary Table 1: Overview of the performances of protein surface patterning methods.

Reference	Light sensitive substrate	Multi-protein	Light (nm)	Resolution (µm)	membrane compatibility	Reversible Dynamics	Special Hardware	Binding approach
Bélisle 2008 ¹⁰	biotin-4-fluorescein	no	473	1	no	no	laser and mask	photobleaching based Biotin absorbance
Bélisle 2009 ¹¹	biotin-4-fluorescein	yes	473 ;671	1.5	no	no	laser and mask	photobleaching based Biotin absorbance
Walbour 2012 ¹²	biotin-5-fluorescein	no	490	2.5	no	no	digital mirror device	photobleaching based Biotin absorbance
Scott 2012 ¹³	biotin-4-fluorescein	no	780	1	no	no	laser and mask	photobleaching based Biotin absorbance
Labòria 2013 ¹⁴	photoactivatable trisNTAs (PA-trisNTAs)	yes	366; 405	z: 50; x: 2	no	no	laser and mask	NTA and His tag
Gatterdam 2014 ¹⁵	The pseudo tripeptide glutathione (GSH ^{NDBF})	yes	365;730	z: 8; x: 2	not show	Yes	laser and mask	pseudo tripeptide glutathione (GSH) and glutathione S-transferase (GST) interaction
Reuther 2014 ¹⁶	By heating thermoresponsive poly(N-isopropylacrylamide)	yes	—	unknown	no	no	laser	
Rudd 2015 ¹⁷	DSPE-PEG lipid anchor with benzylguanine (BG) and photocaged benzylguanine (BG-NPE) head groups.	no	405	unknown	yes	no	laser	benzylguanine (BG)- and SNAP-tag interaction
Strale 2016 ¹⁸	photoinitiator (4-benzoylbenzyl-trimethylammonium chloride	yes	375	0.5	no	no	UV Projection System	Photo drive the Molecular adsorption
This paper	PhyB(PCB)	yes	561	0.5-1	yes	yes	laser	Protein to protein interaction(PhyB-PIF6)

Supplementary Table 2: list of vectors, proteins and genes

<p>Vector 1: Pcoofy12-onestrep-PhyB621-mCherry-His6</p> <p>Protein 1 name: PhyB-mCherry-His6</p> <p>Gene sequence:</p> <p>taatacgaactcactatagggaattgtgagcggataacaattcccctctagaaataatTTTgtttaactttaagaaggagatataccatggggagc gctTGGAGCCACCCGAGTTTCGAAAAAGGTGGAGGTTCTGGCGGTGGATCGGGAGGTTTCAGCGTGGAGCCACC CGCAGTTTCGAGAAAaCgcgggtctggaagtctgtccaggggcccattggttccggagtcggggtagtggcggtggcgtggcggtgg ccgtggcggagaagaagaaccgtcgtcaagtcacactcctaataaccgaaggaggagaacaagctcaatcgtcgggaacgaaatctctcag accaagaagcaactgaatcaatgagcaaaagcaattcaacagtcacccgtcgacgcaagactccacgccgttttgaacaatccggcgaatca gggaaatcattcgactactcaaatcactcaaacgacgactacggttctctgtacctgagcaacagatcacagcttatctctcgaatccagc gaggtggttacattcagcctttcggatgtatgatcgccgtcgatgaatccagtttccggatcatcggttacagtgaanaacccagagaaatgtagg gattatgcctcaatctgttctactcttgagaaactgagattctagctatgggaactgatgtgagatcttgttctacttctcagactcgattctactc gagcgtgcttctggtcgcgagagattacctgttaaatccggttggatccattccaagaatactggtaaaccgttttacgccattctcataggatt gatgttggtgtgtattgatttagaccagctagaactgaagatcctgcgcttctattgctggtgctgttcaatcgcaaaactcgcggtcgtgcg atctctcagttacaggctctcctggtggagatattaagctttgtgtgacactgtcgtgaaagtgtgaggactgactggttatgatcgtgttatg gtttataagttcatgaagatgagcatggagaagtgtagctgagagtaaacgagatgatttagaccttatattggactgattatctcgtactg atattcctcaagcgtcaaggtcttgtttaagcagaaccgtgtccgaatgatagtagattgcaatgccacactgttctgtggtccaggacgatag gctaactcagctatgtgcttgggtggttctactcttaggctcctcatggtgtcactctcagtatatggctaactgggatctattgctttagca atggcggttataatcaatggaaatgaagatgatgggagcaatgtagctagtgaagaagctcgatgaggcttgggggttgggtgttggcatcac acttctctcgtgcataccgtttccgctaaggtatgctgtgagttttgatgcaggcttccggttacagttaaacatggaattgcagtttagcttgc</p>
--

aaatgtcagagaaacgcgttttgagaacgcagacactgttatgtgatgcttctgcgtgactgcctgctggaattgttacacagagtcaccagat
catggacttagtgaatgtgacggtgcagcatttctttaccacgggaagtattaccggtgggtgttctcctagtgaagttcagataaaagatgtt
tggagtgggtgcttgcaatcatgcgattcaaccggattaagcactgatagtttaggcgatgcgggatcccgggtgcagctgcgttaggggatg
ctgtgtcgggtatggcagttgcataatcacaaaaagagactttctttttggttctgatctcactgcgaaagaaatcaaatggggagggcgtaa
gcatcatccggaggataaagatgatgggcaacgaatgcacctcgttctcctttcaggcttttcttgaagttgtaagagccggagtcagccatgg
gaaactgcgaaatggatgcgattcactcgcctccagcttattctgagagactcttttaagaatctgaattcagatagtgctgtagtgctgtagtg
ctggtgtagtccctagtgcagcaaggcgaggaggataaacatggccatcatcaaggagttcatgcctcaaggtgcacatggagggtccgtg
aacggccacgagttcgagatcgagggcgagggcgagggccgccctacgagggcaccagaccgccaagctgaaggtgaccaagggtggccc
cctgcccttcgctgggacatcctgtccctcagttcatgtacggctcaaggcctacgtgaagcaccgccgacatccccgactacttgaagctg
tccttcccagggttcaagtgaggagcgcgtgatgaactcgaggacggcggcgtggtgaccgtgaccagactcctcctgcaggacggcga
gttcatctacaaggtgaagtcgcgccaccaactcccctccgacggccccgtaatgcagaagaagaccatgggctgggaggcctcctccgagc
ggatgtaccccaggacggcgcctgaagggcgagatcaagcagaggtgaagctgaaggacggcggcactacgacgctgaggtcaagacc
acctacaaggccaagaagcccgtgcagctgccggcgctacaacgtcaacatcaagttggacatcacctcccacaacgaggactacacccatcg
ggaacagtaagaacgcgagggccgactccaccggcggcatggacgagctgtaagggtagcgatagcagggcagtgctggttaaggc
tagcggtaaaaagaagaaaagaagcaagacaagtgtaattagccagttttacctggatgagcaccaccaccaccactga

Vector 2: Pcoofy1-His6-HRV-EYFP-PIF6

Protein2 name: EYFP-PIF6

Gene sequence:

Taatacgcactactaggggaattgtgagcggataacaattcccctctagaataatgttttaactttaagaaggagatataccatgaaa
catcaccatcaccatcactccgcggtctggaagtctgttccaggggcccATGGTGAGCAAGGGCGAGGAGCTGTTACACGGGG
TGGTGCCCATCCTGGTCGAGCTGGACGGCGACGTAAACGGCCACAAGTTCAGCGTGTCCGGCGAGGGCGAGG
GCGATGCCACCTACGGCAAGCTGACCCTGAAGTTCATCTGCACCACCGCAAGCTGCCCGTGCCCTGGCCCACC
CTCGTGACCACCTTCGGCTACGGCCTGCAGTGCTTCGCCGCTACCCCGACCACATGAAGCAGCAGACTTCTTC
AAGTCCGCCATGCCGAAGGCTACGTCCAGGAGCGCACCATCTTCTTCAAGGACGACGGCAACTACAAGACCC
GCGCCGAGGTGAAGTTCGAGGGCGACACCCTGGTGAACCGCATCGAGCTGAAGGGCATCGACTTCAAGGAGG
ACGGCAACATCCTGGGGCACAAGCTGGAGTACAACACTACAACAGCCACAACGTCTATATCATGGCCGACAAGCA
GAAGAACGGCATCAAGGTGAAGTTCAGATCCGCCACAACATCGAGGACGGCAGCGTGCAGCTCGCCGACCAC
TACCAGCAGAACACCCCATCGGCGACGGCCCCGTGCTGCTGCCGACAACCACTACCTGAGCTACCAGTCCGC
CCTGAGCAAAGACCCCAACGAGAAGCGCGATCACATGGTCTGCTGGAGTTCGTGACCGCCGCGGGATCACT
CTCGGCATGGACGAGCTGTACAAGggatccATGATGTTCTTACCAACCGATTATTGTTGCAGGTTAAGCGATCAA
GAGTATATGGAGCTTGTGTTTGAGAATGGCCAGATTCTTGCAAAGGGCCAAAGATCCAACGTTTCTCTGCATAA
TCAACGTACCAAATCGATCATGGATTTGTATGAGGCAGAGTATAACGAGGATTTTCATGAAGAGTATCATCCATG
GTGGTGGTGGTCCATCACAATCTCGGGGACACGCAGGTTGTTCCACAAAGTCATGTTGCTGCTGCCATGAA
ACAAACATGTTGAAAGCAATAAACATGTTGACTAA

Vector 3: Pcoofy1-His6-HRV-FtsZ(1-366)-YFP-PIF6

Protein3 name: FtsZ-YFP-Pif6

Gene sequence:

taatacgcactactagggcatcaccatcaccatcactccgcggtctggaagtctgttccaggggcccagtttgaaccaatggaacttacaat
gacgcggtgattaaagtcacgctgcggtcggcgggcggtgtaagctgttgaacacatggtgcgagcgcattgaaggtgttgaattctcgcg
gtaaataccgatgcacaagcgtgcgtaaaacagcggttggacagacgattcaaatcggtagcggatcaccaaaggactggcgctggcgcta
atccagaagttggccgcaatgcggctgatgaggatcgcatgattcgtgcggcgtggaaggtgcagacatggtctttattgctcgggtatgg
gtggtggtaccggtacaggtgcagcaccagtcgtcgtgaagtggaagattgggtatcctgaccgttgcgtcgtcactaagccttcaact
tgaaggcaagaagcgtatggcattcgcggagcaggggatcactgaactgccaagcatgtggactctctgatcactatcccgaacgacaaactgc
tgaagttctgggcccgggtatcctcctgctggatgcgtttggcgcagcgaacgatgtactgaaaggcgtgtgcaaggtatcgctgaactgattac

```
tcgtccgggtttgatgaactggactttgcagacgtacgcaccgtaatgtctgagatgggctacgcaatgatgggttctggcgtggcgagcgggtga
agaccgtgcggaagaagctgctgaaatggctatcttctccgctgctggaagatatcgacctgtctggcgcgcgggcgctgctgggtaacatcac
ggcgggcttcgacctgctgctggatgagttcgaacggtaggtaacacatccgtgcatttctccgacaacgcgactgtgggtatcggtacttctc
ttgaccggatgatgaatgacgagctgcgcgtaaccgttgtgcgacaggtatcgcatggacaaacgtcctgaaatcactctggtgaccaataagc
aggttcagcagccagtgatggatcgctaccagcagcatgggatggctccgctgaccaggagcagaagccggttgctaaagctgtaatgacaat
gcgcccgaactgcgccccctgcacctgcaggcggccgcatgggtgagcaagggcgaggagctgttcaccgggggtggtgccatcctggctgagct
ggacggcgacgtaaacggccacaagttcagcgtgtccggcgagggcgagggcgatgccacctacggcaagctgacctgaagctgatctgcacc
accggcaagctgccggtgccctggcccacctcgtgaccacctgggctacggcctgagtgcttcgcccgtaccccgaccatgaagcagcac
gacttctcaagtccgcatgccgaaggctactccaggagcgcaccatcttctcaaggacgacggcaactacaagaccgcccggaggtgaa
gttcgagggcgacacctgggtgaaccgcatcgagctgaaggcatcgacttcaaggaggacggcaacatcctggggcacaagctggagtacaac
tacaacagccacaacgtctatatcaccgcccgaagcagaagaacggcatcaaggccaactcaagatccgccacaacatcagggacggcggc
gtgacgtcgcggaccactaccagcagaacacccccatggcgacggccccgtgctgctgccgacaaccactacctgagctaccagtccgccc
gagcaaagaccccaacgagaagcgcgatcacatggtcctgctggagttcgtgaccgcccgggatcactctggcatggacgagctgtacaag
ggatccATGATGTTCTTACCAACCGATTATTGTTGCAGGTTAAGCGATCAAGAGTATATGGAGCTTGTGTTTGAGA
ATGGCCAGATTCTTGCAAAGGGCCAAAGATCCAACGTTTCTCTGCATAATCAACGTACCAAATCGATCATGGAT
TTGTATGAGGCAGAGTATAACGAGGATTTTCATGAAGAGTATCATCCATGGTGGTGGTGGTGCCATCACAATCT
CGGGGACACGCAGGTTGTTCCACAAAGTCATGTTGCTGCTGCCATGAAACAAACATGTTGGAAAGCAATAAA
CATGTTGACTAA
```

Vector 4: pQE80L-FtsZ
Protein4 name: FtsZ

```
atgtttgaaccaatggaacttaccatgacgcggtgattaaagtcacggtcggcgggcgggcggtaatgtgttgaacacatggtgcgcga
gacgattgaaggtgtgaattcttcgcggtaaataccgatgcacaagcgtcgtgtaaaacagcggttgacagacgattcaaatcggtagcggat
caccaaaggactggcgctggcgtaatccagaagttggccgcaatgcggctgatgaggatcgcgatgattgcgtgcggcgctggaaggtgca
gacatggtctttattgctgcggttatgggtgggtaccggtacaggtgcagcaccagtcgtcgtgaagtggcaaaagattgggtatcctgaccg
ttgctgctgactaagccttcaacttgaaggcaagaagcgtatggcattcgcggagcaggggatcactgaactgtccaagcatgtggactctc
gatcactatcccgaacgacaaaactgctgaaagtctgggcccgggtatctccctgctggatgcgttggcgacgcaacgatgtactgaaaggcgc
tgtgcaaggtatcgctgaaactgattactcgtccgggttgatgaacgtggactttgcagacgtacgcaccgtaatgctgagatgggctacgcaatg
atgggttctggcgtggcgagcgggtgaagaccgtgcggaagaagctgctgaaatggctatcttctccgctgctggaagatcgacctgtctggc
gcgcgggcgctgctggttaacatcacggcgggcttcgacctgctgctgagtgatgctgaaacggtaggtaacacatcctgacattgctccgac
aacgcgactgtggtatcggtacttcttgacctggatgatgaatgacgagctgcgcgtaaccgttgtgacaggtatcgcatggacaaacgtc
ctgaaatcactctggtgaccaataagcaggttcagcagccagtgatggatcgctaccagcagcatgggatggctccgctgaccaggagcagaa
gcccgttgctaaagctgtaatgacaatgcccgaactgcgaaagagccgattatctggatcccagattcctgcgtaagcaagctgatT
AA
```

Supplementary Movies

Supplement Movie S1. PhyB–PIF6 photoswitchable global recruitment *in vitro* were tested on the surface of Ni-NTA agarose beads.

Supplement Movie S2. Reversibly spatial activating recruitment of EYFP-PIF6 protein to the specific localization on the beads with 561 nm laser and 740nm LED light source.

Supplement Movie S3. Single FtsZ ring emerging from its recruitment to a supported membrane by the light sensitive interaction.

Supplement Movie S4. TIRF monitored global view of the rings developing on the SLB controlled with light sensitive interaction.

Supplement Movie S5. FtsZ rings dissociated from a supported membrane under 740nm light.

References

1. Scholz, J.; Besir, H.; Strasser, C.; Suppmann, S., A new method to customize protein expression vectors for fast, efficient and background free parallel cloning. *BMC Biotechnol.* **2013**, *13* (1), 12.
2. Osawa, M.; Anderson, D. E.; Erickson, H. P., Reconstitution of contractile FtsZ rings in liposomes. *Science* **2008**, *320* (5877), 792-794.
3. Galush, W. J.; Nye, J. A.; Groves, J. T., Quantitative fluorescence microscopy using supported lipid bilayer standards. *Biophys. J.* **2008**, *95* (5), 2512-2519.
4. Vacklin, H. P.; Tiberg, F.; Thomas, R., Formation of supported phospholipid bilayers via co-adsorption with β -D-dodecyl maltoside. *Biochim. Biophys. Acta - Biomembranes* **2005**, *1668* (1), 17-24.
5. Schindelin, J.; Arganda-Carreras, I.; Frise, E.; Kaynig, V.; Longair, M.; Pietzsch, T.; Preibisch, S.; Rueden, C.; Saalfeld, S.; Schmid, B., Fiji: an open-source platform for biological-image analysis. *Nat. Methods* **2012**, *9* (7), 676-682.
6. Xu, T.; Vavylonis, D.; Tsai, F.-C.; Koenderink, G. H.; Nie, W.; Yusuf, E.; Lee, I.-J.; Wu, J.-Q.; Huang, X., SOAX: a software for quantification of 3D biopolymer networks. *Sci Rep* **2015**, *5*, 9081.
7. Turner, D. J.; Portman, I.; Dafforn, T. R.; Rodger, A.; Roper, D. I.; Smith, C. J.; Turner, M. S., The mechanics of FtsZ fibers. *Biophys. J.* **2012**, *102* (4), 731-738.
8. Ratanji, K. D.; Derrick, J. P.; Dearman, R. J.; Kimber, I., Immunogenicity of therapeutic proteins: influence of aggregation. *J. Immunotoxicol.* **2014**, *11* (2), 99-109.
9. Angelova, M. I.; Dimitrov, D. S., Liposome electroformation. *Faraday Discuss Chem Soc* **1986**, *81*, 303-311.
10. Bélisle, J. M.; Correia, J. P.; Wiseman, P. W.; Kennedy, T. E.; Costantino, S., Patterning protein concentration using laser-assisted adsorption by photobleaching, LAPAP. *Lab Chip* **2008**, *8* (12), 2164-2167.
11. Bélisle, J. M.; Kunik, D.; Costantino, S., Rapid multicomponent optical protein patterning. *Lab Chip* **2009**, *9* (24), 3580-3585.
12. Waldbaur, A.; Waterkotte, B.; Schmitz, K.; Rapp, B. E., Maskless projection lithography for the fast and flexible generation of grayscale protein patterns. *Small* **2012**, *8* (10), 1570-1578.
13. Scott, M. A.; Wissner-Gross, Z. D.; Yanik, M. F., Ultra-rapid laser protein micropatterning: screening for directed polarization of single neurons. *Lab Chip* **2012**, *12* (12), 2265-2276.
14. Labòria, N.; Wieneke, R.; Tampé, R., Control of nanomolar interaction and in situ assembly of proteins in four dimensions by light. *Angew. Chem. Int. Ed.* **2013**, *52* (3), 848-853.
15. Gatterdam, V.; Ramadass, R.; Stoess, T.; Fichte, M. A.; Wachtveitl, J.; Heckel, A.; Tampé, R., Three - Dimensional Protein Networks Assembled by Two - Photon Activation. *Angew. Chem. Int. Ed.* **2014**, *53* (22), 5680-5684.

16. Reuther, C.; Tucker, R.; Ionov, L.; Diez, S., Programmable patterning of protein bioactivity by visible light. *Nano Lett.* **2014**, *14* (7), 4050-4057.
17. Rudd, A. K.; Valls Cuevas, J. M.; Devaraj, N. K., SNAP-tag-reactive lipid anchors enable targeted and spatiotemporally controlled localization of proteins to phospholipid membranes. *J. Am. Chem. Soc.* **2015**, *137* (15), 4884-4887.
18. Strale, P. O.; Azioune, A.; Bugnicourt, G.; Lecomte, Y.; Chahid, M.; Studer, V., Multiprotein Printing by Light - Induced Molecular Adsorption. *Adv. Mater.* **2016**, *28* (10), 2024-2029.

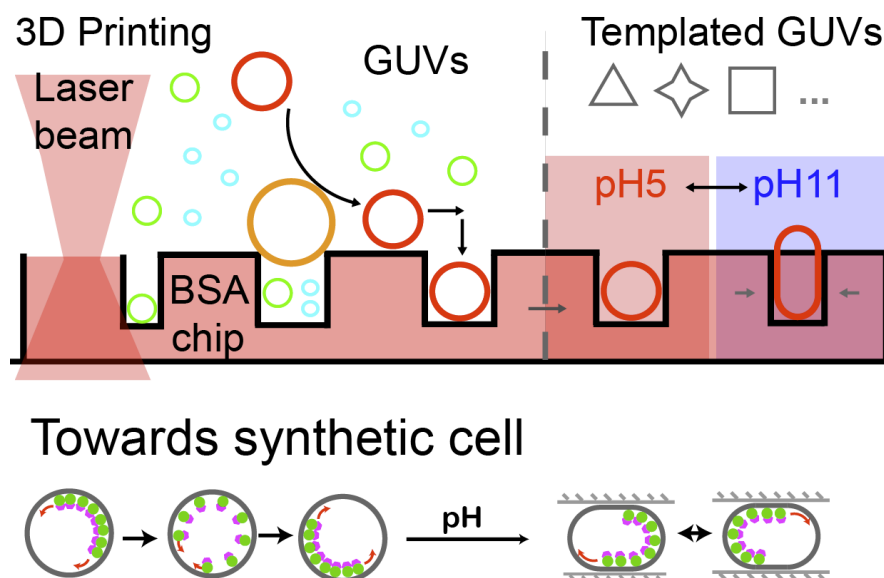
Manuscript

3D space regulation tools:

2.3 Shaping membrane vesicles in 3D-printed protein hydrogel cages

In this manuscript, we introduce a microscale device based on 3D printed protein hydrogel that can induce reversible shape changes in trapped vesicles without compromising their free-standing membranes. The tunable shaped vesicles are particularly desirable for reconstituting membrane polarity- or shape-dependent protein systems that request explicitly non-spherical geometries. The spatially well-defined microenvironment can mimic the dynamic native cell matrix, allowing us to investigate how synthetic cells react to and interact with external mechanical cues.

The results discussed in this section are currently under review.



Shaping membrane vesicles in 3D-printed protein hydrogel cages

Haiyang Jia, Thomas Litschel, Michael Heymann, Hiromune Eto, Henri G. Franquelim,
Petra Schwille*

Max Planck Institute of Biochemistry, Am Klopferspitz 18, D-82152 Martinsried, Germany.
E-mail: schwille@biochem.mpg.de

Keywords: bottom-up synthetic biology, membranes, 3D printing, Min system, hydrogel

Giant unilamellar phospholipid vesicles are attractive starting points for constructing minimal living cells from the bottom-up. Their membranes are compatible with many physiologically functional modules and act as selective barriers, while retaining a high morphological flexibility. However, their spherical shape renders them rather inappropriate to study phenomena that are based on distinct cell shape and polarity, such as cell division. Here, a microscale device based on 3D printed protein hydrogel is introduced to induce pH-stimulated reversible shape changes in trapped vesicles without compromising their free-standing membranes. Deformations of spheres to at least twice their aspect ratio, but also towards unusual quadratic or triangular shapes can be accomplished. Mechanical force induced by the cages to phase-separated membrane vesicles can lead to spontaneous shape deformations, from the recurrent formation of dumbbells with curved necks between domains to full budding of membrane domains as separate vesicles. Moreover, shape-tunable vesicles are particularly desirable when reconstituting geometry-sensitive protein networks, such as reaction-diffusion systems. In particular, vesicle shape changes by swelling of the hydrogel cages allow to induce different modes of self-organized protein oscillations, and thus, to influence reaction networks directly by external mechanical cues.

1. Introduction

Bottom-up reconstitution of well-characterized functional biomaterials, such as molecular entities, parts and modules, with the final goal of constructing a synthetic cell, is a fascinating variant of Synthetic Biology. Although this goal may not easily be within reach in the next years and potentially decades, cell-free reconstitution of fundamental biological functions has interesting implications for research on the origin of life^[1] on one hand, and may open up new potential applications from medicine to technology on the other hand.^[2] In order to accomplish large-scale biomimetic behavior and realize the vision of a fully functional synthetic cell, a large number of cutting-edge tools or technologies inspired by nanotechnology and material science have been developed and favorably employed to this end.^[3] With regard to providing a maximally biocompatible and biomimetic compartment as a first step towards a cell-like reaction space, giant unilamellar vesicles (GUVs) composed of phospholipids have in the past years gained great attention.^[4] GUV membranes mimic cellular membranes in many relevant aspects, their lipid composition can be tuned over a wide range,^[5] they can be supported by a minimal cortex,^[6] and even large transmembrane proteins can be reconstituted into them.^[7] However, many advanced protein functionalities like cell division, differentiation, migration and signaling require the establishment of spatial anisotropy, or in other words, polarization,^[8] which is hard to realize in spherical vesicles. In particular, reconstituted bacterial cell division machineries that are supposed to ultimately induce controlled vesicle splitting have been shown to require elongated geometries with distinct symmetry axes.^[9]

Thus, developing ways for a controlled deformation of GUVs into desired shapes, resulting in an anisotropic membrane or a polar physical microenvironment, will greatly improve our toolbox for the bottom-up reconstitution of biological functionality towards a synthetic cell. So far, several methods to template membrane vesicles and induce anisotropic structure *in vitro* have been developed, like microfluidics,^[10] micropipette aspiration, optical tweezers, and dielectrophoretic field cages.^[11] However, most of them require sophisticated technology or are unable to dynamically control the membrane geometry in a well-defined, i.e., precise and programmable, manner. On the other hand, cell biology-derived tools like 2D micro-patterning^[12] and 3D soft lithography of hydrogel^[13] have been successfully applied to control interfacial geometry in order to define the extracellular environment. Since the development of 3D printing technology, rationally designed 3D objects can be produced from various materials on different scales. In this

context, stimuli-responsive hydrogels, which can cycle between expanded and condensed states in response to environmental triggers (e.g., pH, ionic strength), could constitute an attractive material for 3D or 4D Printing.^[14] In fact, pH-responsive BSA hydrogels are already widely used to fabricate 3D tissue scaffolds^[15] and generating smart 4D stimuli-responsive micro-actuators.^[14, 16]

Here, we varied and expanded this technology towards the goal of selectively trapping GUVs within a customized 3D printed BSA hydrogel chip, and dynamically inducing structural anisotropy by applying external pH stimuli to the gel. The basic working principle is illustrated in **Figure 1**. 3D printed protein hydrogel can be designed as micro-chambers in appropriate sizes for capturing GUVs. The variable protein hydrogel structure acts as a geometrical cue to establish synthetic cell polarity *in vitro* by compressing vesicles into different shapes upon pH stimuli. This spatially well-defined microenvironment can mimic the dynamic native cell matrix, allowing us to investigate how synthetic cells react to and interact with external mechanical cues.

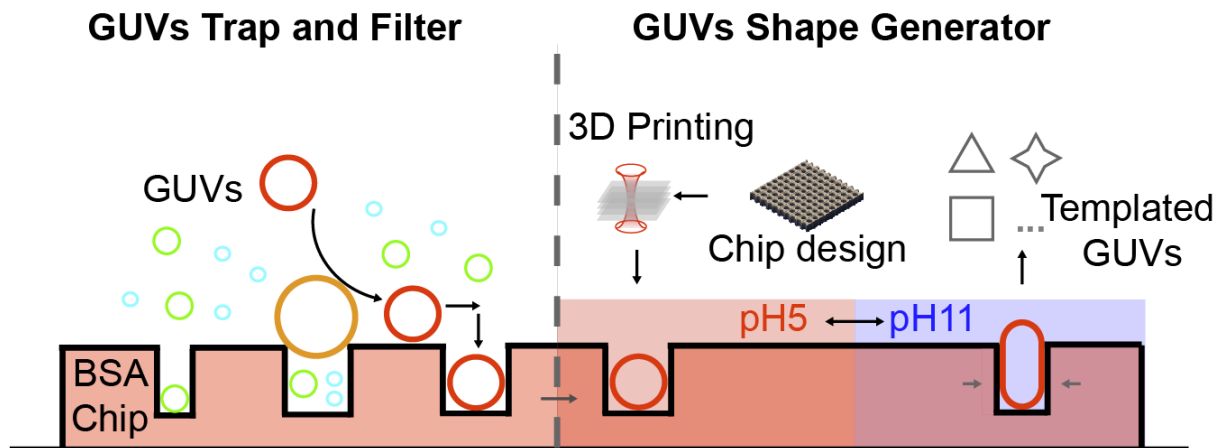


Figure1. Concept of 3D-printed protein hydrogel trapping and templating giant vesicles (GUVs)

2. Results and Discussion

GUVs themselves can be generated either by electroformation, gentle hydration of dehydrated lipids, inverted emulsion transfer or by microfluidic jetting. Procedures to handle these delicate objects are still not consummate.^[17] They encompass sedimentation with high density fluids, immobilization on functionalized surfaces,^[18] manipulation by micropipette aspiration^[19], or microfluidic systems.^[11, 17] As an alternative, but still being compatible with these established protocols, our 3D BSA protein hydrogel GUVs traps were fabricated in a layer-by-layer procedure

via two-photon polymerization process, using Rose bengal as the photoinitiator for BSA monomers. In contrast to other trapping approaches, surface functionalization for avoiding GUV-surface adhesion is not required for the 3D printed hydrogel chips. GUVs filled with high density solution, like sucrose, can spontaneously sink down into the hydrogel micro-chambers. Trapping in the chambers prevents GUVs from being flushed away and from being mechanically deformed by applied flow. To rationally design a trap that can be easily adapted to different sizes of GUVs, we chose a simple module consisting of a solid cube (14x14x14 μm) extrude-cut by half-cylinders (Diameter: 10 μm) on both sides (Supplement Figure S3a). These GUV traps were then arranged into a 10x10-module array. Through controlling the distance of rows and columns in the array, we can generate two different types of trap chips: individual traps, or group traps. With 1 μm distance for both rows and columns, the individual trap chip can be used to capture GUVs one by one within 81 separated cylinder wells (**Figure 2a** and Supplement Figure S1a). The GUVs here utilized were obtained through electroformation^[20], composed of DOPC(1,2-dioleoyl-sn-glycero-3-phosphocholine) and doped with 0.5 mol% Atto655-DOPE(1,2-dioleoyl-sn-glycero-3-phosphoethanolamine) for fluorescence detection. By extending the row distance to 15 μm , groups of GUVs can be trapped between two full rows (Figure 2b and Supplement Figure S1b), in order to manipulate many vesicles at once, or to enforce their communications and interactions. The sizes of GUVs to be trapped depend on the diameters or distances, respectively (Figure 2c). GUVs with diameters larger than the gap distance are filtered out. The selective trapping of GUVs by the hydrogel chip, either as individuals or in groups, allows their size to be roughly controlled, as a first criterion towards establishing geometric anisotropy of vesicles.

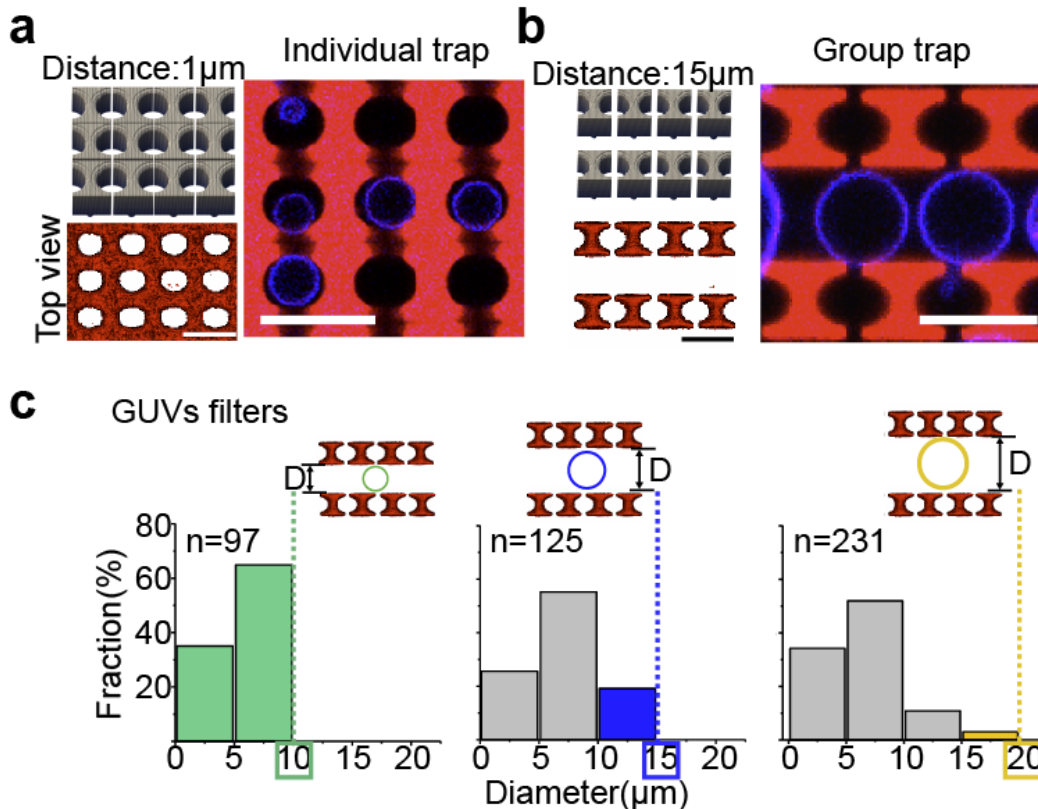


Figure 2. 3D-printed protein hydrogel chips filtering and trapping different-sized vesicles. a.) chip design for trapping individual GUVs, scale bar 20µm. Left (top): All micro-chambers were integrated in one chip. Left (bottom): top view. Right: trapping individual GUVs in separated hydrogel chambers. b.) chip design for group trapping, scale bar 20µm. Left (top): The chip was combined with separated units as barriers with certain distance. Left (bottom): top view. Right: trapping GUVs in between the hydrogel barriers. c.) 3D printed hydrogel traps as GUV filters with different row distances. n: number of trapped GUV numbers. D: distance.

In addition to allowing for a flexible size-filtering design, BSA hydrogel also shows tremendous potential in generating smart pH stimuli-responsive micro-devices that can be used to dynamically mimic the native cellular microenvironment *in vitro*. The isoelectric point of BSA is close to pH 5, where a protein has no net charge and fewer ion-dipole interactions. Therefore, the structures absorb less water than at higher pH and thus cover the smallest area at pH 5^[16a, 21] Due to the larger number of ionized amino acids in BSA, swelling of the structures can be induced at higher pH. However, precisely controlling pH can be difficult. To improve controllability, the swelling

capability can be effectively tuned by fabrication parameters such as slicing distance (layer distance), laser power, and laser scan speed, shown in **Figure 3** and Supplement Figure S2. The area swelling ratios of $14 \times 14 \times 15 \mu\text{m}$ cubes can be tuned from 1.1 to 1.7 (Figure 3b-d). A larger slicing distance results in lower crosslinking density and allows more water to enter inside the hydrogel, which in turn increases the swelling ability. Similarly, lower laser power also increases the swelling ratio to 1.7 (Figure 3c), but loses spatial resolution of printing. Because of the lower crosslinking degree under low laser power, the structures printed with 30mW laser power are approximately 30% larger than that printed with 50mW (supplement Figure S2d). When varying the scan speed, structures at pH between 5 and 8 have weak swelling capability and the maximal swelling ratio at pH 11 can only reach a factor of 1.5 (Figure 3d).

The controllable swelling ratios of 3D printed hydrogel structures enable a programmable templating of GUV geometries with pH-stimuli GUVs traps. Due to the swelling effect of the traps, the total structure occupies more volume, which should in turn shrink the free inner volume of the chambers. The swelling behavior of a square-frame trap was first investigated. It was designed by extruding cut $15 \times 15 \times 15 \mu\text{m}$ square wells in the center of $45 \times 45 \times 15 \mu\text{m}$ cuboid (Figure 3e). The hydrogel frame can swell 1.57 ± 0.15 fold (mean \pm s.d.) at pH 11 compared to pH 5; however, no shrinking of the inner area was observed. The potential reason is the increased surface tension at the inner side of the hydrogel frame, scaling inversely with radius. To improve the design towards a truly contractible and at the same time anisotropic trap, the structure was divided into eight separate small rectangular modules (Figure 3f). Allowing $2 \mu\text{m}$ distance between the modules in the relaxed state should support swelling in all directions. Because there exists no physical interaction between the module surfaces as in the previous design, the section area of the inner free space could be decreased to 75% ($\pm 2.2\%$) in the swollen state, when the pH was changed from 5 to 11 (Figure 3f, bottom right). Another advantage of the modular design is that the distance between the modules can be varied, in order to accommodate a larger growth regime and anisotropic compression. Small distances may lead to surface contact between the modules during swelling, which induces shape changes and restricts the overall compression effect (Supplement Figure S4).

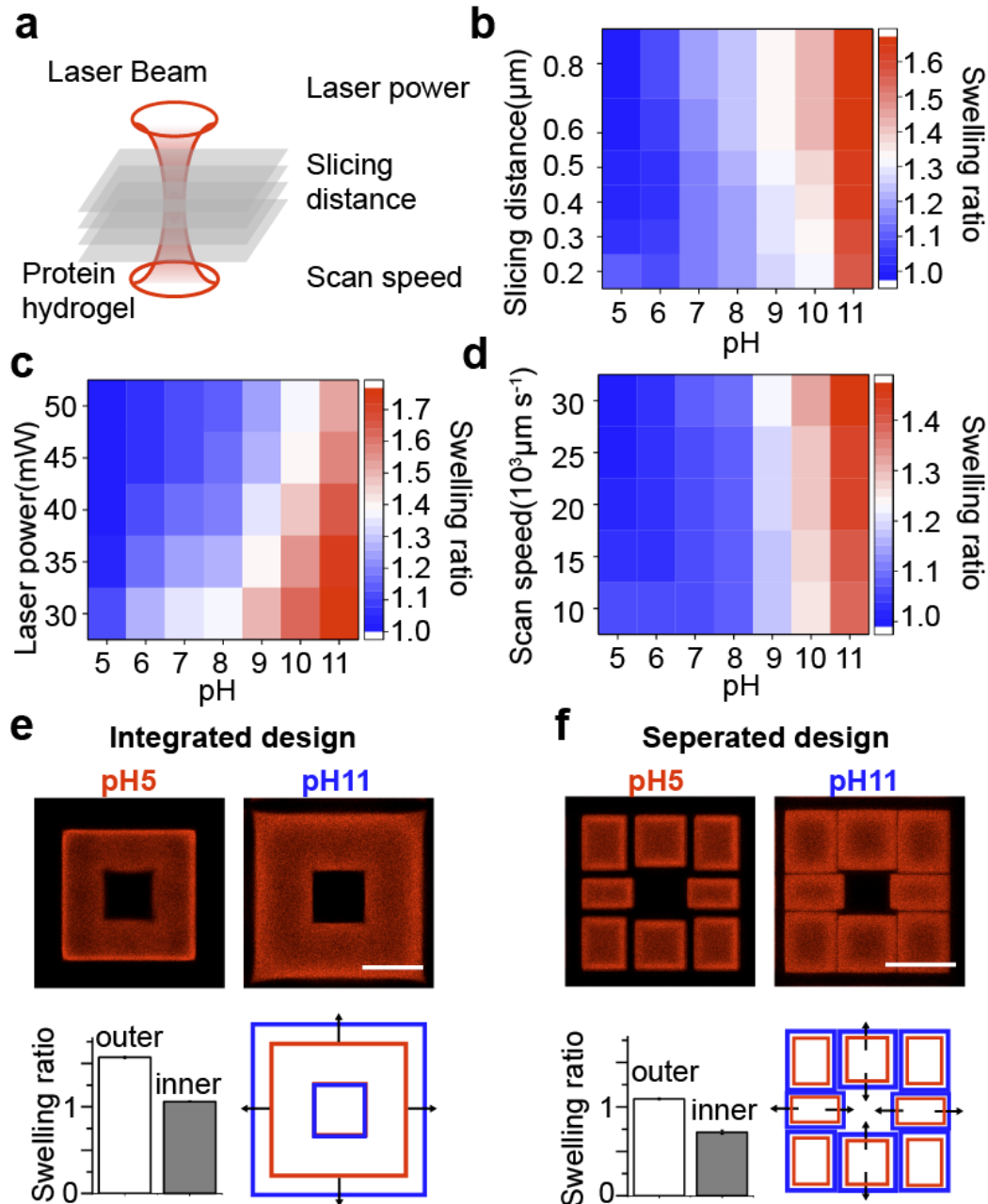


Figure 3. pH-stimuli responsive protein hydrogel. a.) Laser fabrication of hydrogel layer by layer with two-photon excitation. b-d.) Tuning pH-stimuli swelling ratio by varying slicing distance (b.), laser power (c.), and laser scan speed (d.). Printing parameters: (b) laser power: 50mW, Scan speed: $30000 \mu\text{m s}^{-1}$; (c) Slicing distance: $0.5 \mu\text{m}$, Scan speed: $30000 \mu\text{m s}^{-1}$; (d): Slicing distance: $0.5 \mu\text{m}$; laser power: 50mW. e-f.) pH-dependent swelling of integrated chip and the combined chip (Slicing distance: $0.5 \mu\text{m}$; laser power: 50mW; Scan speed: $30000 \mu\text{m s}^{-1}$), scale bar $20 \mu\text{m}$. Top: confocal imaging of the swelling effect under different pH. Bottom (left): swelling ratios of outer

and inner area. Bottom (right): directional swelling. Area swelling ratio is defined as A / A_0 , where A_0 is the area of the structure at pH 5, printed under slicing distance: $0.5\mu\text{m}$, laser power: 50mW , scan speed: $30000\mu\text{m s}^{-1}$.

In order to evaluate the mechanical effects of compression on the trapped vesicles, the pH stimuli-responsive hydrogel chambers were now applied to deform membrane vesicles. The basic module of the group trap can swell in both x- and y- directions and thus occupies free space between modules after shifting pH from 5 to 11 (**Figure 4a**). In the rows, the distance between the modules was significantly reduced. Perpendicularly to this, two neighboring modules fused to yield a lens-shaped well, but with larger diameter than the half-cylinder at pH5. The channels between the individual barriers were also narrowed to about 50% (Figure 4a). In response to the pH stimuli, the hydrogel can process fast swelling within one minute, supporting a dynamic mimicry of the cell microenvironment *in vitro* (Figure 4b and Supplement movie S1). The trapped GUVs were now investigated by optical microscopy (Figure 4c). After shifting the pH to 11, the spherical vesicles were compressed by the closing walls, flattening them and forcing them into non-spherical symmetry (Figure 4d, e). The distance between the two rows was $11.97 \pm 0.34 \mu\text{m}$ at pH 11, so that vesicles larger than $\sim 12 \mu\text{m}$ in diameter were compressed. With increasing confinement under swelling conditions over a time course of 6 minutes, the curvature became anisotropic, with flat areas facing the hydrogel and increased curvatures in the free zone (Figure 4d). At the same time, the membrane tension was increased, due to the loss of spherical symmetry and the volume conservation, which imposes some constraints on the aspect ratio σ (length vs. width) of the vesicles that can be reached by this procedure without compromising membrane integrity. An aspect ratio of up to about twofold (length vs. width) could however be easily reached in this setup (Supplement Figure S5). Importantly, the hydrogel swelling is reversible, and the vesicle shapes can thus be switched between spherical and elongated by alternating between the two pH values (Figure 4e).

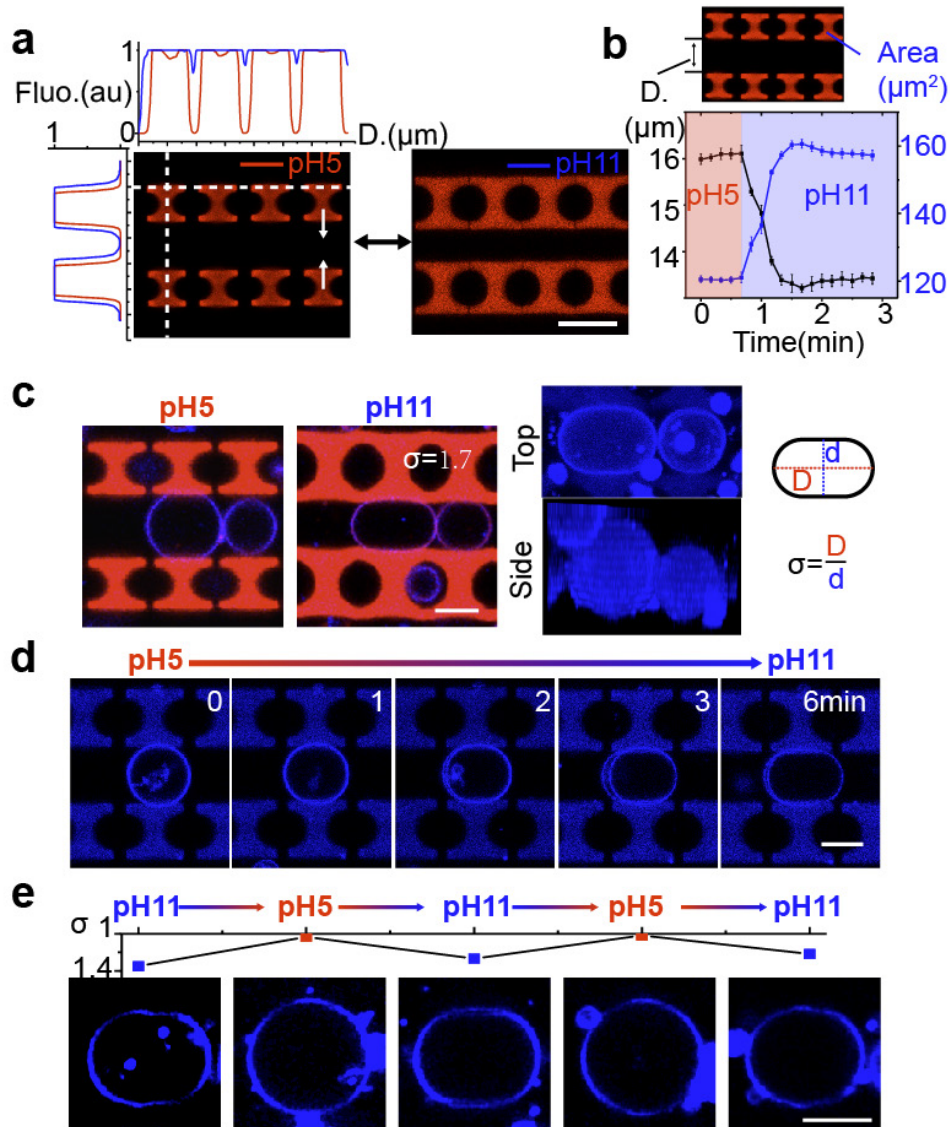


Figure 4. Reversibly deforming membrane vesicles by pH. a) Swelling effect of group trap at increased pH, scale bar 20 μm . The line plots demonstrate the swelling in both x- and y-axis, respectively. b.) Response of geometry factors area and distance when transitioning to pH 11 solution. c.) Swelling chip deforming DOPC GUV, scale bar 10 μm . Right: top and side view of deformed GUVs. d.) Dynamic deformation of GUV by exchanging pH from 5 to 11, scale bar 10 μm . e.) Reversibility of GUV aspect ratio (σ) by alternating pH, scale bar 10 μm .

Furthermore, different designs of the hydrogel structures allow us to induce unusual shapes of the GUVs, and thus, membrane geometries, by varying the contact zones between the hydrogel and

the vesicles. The cylindrical chip was designed by extruding a cylinder (diameter, 15 μm) in the center of cube (20x20x20 μm) (**Figure 5a** and Supplement Figure S3d). Then the cube with the cylindrical well was quartered. This chip was used to trap vesicles of $\sim 15 \mu\text{m}$ diameter. When the pH was increased from 5 to 11, the four separated modules swelled centripetally and compressed the captured membrane vesicle. The area of the cross section was reduced, in turn the height was increased. Similarly, with alternative designs, GUVs can be deformed to other shapes like cross prisms, cubes, and triangular prisms (Figure 5 b-c). Due to the surface tension of membrane vesicles, the templated cross-prismatic, cubic and triangular prismatic vesicles all formed curved corners and spherical domes.

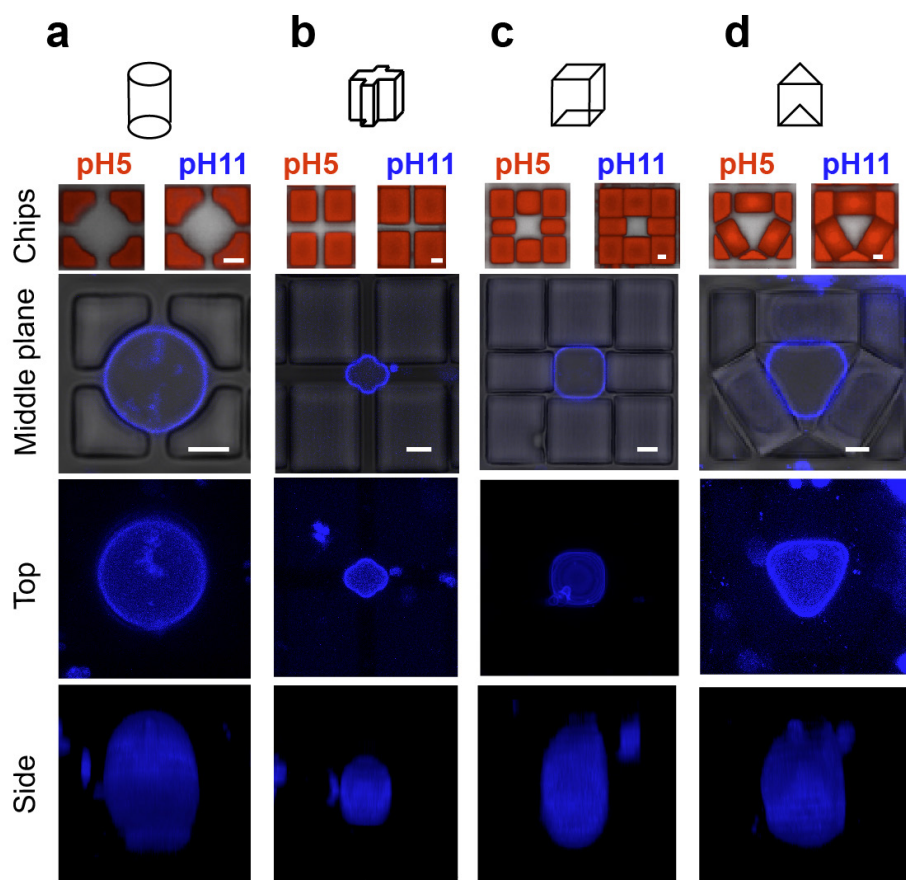


Figure 5. Various 3D hydrogel designs for templating DOPC vesicles into different shapes: a.) cylinder, b.) cross prism, c.) cube, d.) triangular prism. The schemes in the first row show the 3D geometries of trap wells. Below the schemes are the top views of the chips in response to different pH, scale bar 5 μm . Third row from top: confocal imaging of the middle cross section of vesicles,

scale bar 5 μ m. The bottom two rows represent the 3D z-stack reconstitution of different geometrical vesicles.

Having shown that GUVs can not only be reversibly compressed, but also molded into arbitrary non-spherical shapes by our laser-printed BSA pH responsive hydrogel structures, we next aim to demonstrate how these mechanical constraints may influence membrane structure and dynamics in the shaped vesicles. In particular, GUVs have long been used to elucidate the molecular details of lipid phase separation; however, their usually spherical symmetry and isotropic structure have significantly limited the comparability of these model membranes with biological ones. In physiological environments, cells acquire and maintain spatial and functional asymmetry of their plasma membrane^[22] in response to external mechanical cues. Similarly, in model membrane systems exhibiting visible lipid domains enriched in cholesterol and saturated lipids, strong correlations between membrane composition and 3D vesicle shape could be observed, which suggest that in turn, mechanical constraints will lead to significant membrane transformations. ^[22-23]

The phase separated GUVs we investigated in our stimuli responsive hydrogel cages consisted of ternary lipid mixtures composed of cholesterol (Ch), sphingomyelin (SM), and the unsaturated phospholipid DOPC, with a molar ratio of 2:2:1 at room temperature.^[24] The mixture can separate into two co-existing membrane phases: a liquid-ordered phase (L_o) enriched in SM and Ch; and a liquid-disordered (L_d) phase consisting primarily of DOPC. To discriminate between the L_o and L_d phases by fluorescence microscopy, we used 0.3%NBD-DSPE and 0.2% Atto655-DOPE, respectively. The spherical phase-separated GUVs were trapped in the triangular prismatic hydrogel chips (Supplement Figure S3c). When the GUVs were compressed by the swelling hydrogel chamber under pH stimuli, the vesicles deformed to fit the diminished inner area, often accompanied by a large-scale reorganization and fusion of the domains on their membrane surface (Supplement Figure S6). In several cases, particularly for vesicles with large domains, the spherical vesicle was transiently deformed upon compression into a dumbbell geometry, due to line tension between L_o - L_d domains,^[25] acquiring a clear curved neck at the domain boundary. Typically, the dumbbell-shaped phase-separated vesicle then rotated within the contracted hydrogel cavity, in order to adapt the space change and relax back into a spherical (yet compacted)

energetically favorable shape (**Figure 6b** and S7, Supplement Movie S2 for top view of 3D imaging, S3 for orthogonal view). Occasionally, however, the compression could lead to the fission of a Lo domain away from the trapped GUV membrane (i.e. budding as a way to overcome line tension,^[26] ultimately changing the overall membrane composition of the remaining “mother” vesicle (Figure 6c and Supplement movie S4). In the control experiment without the swelling traps, no triggered deformation events were detected upon pH change from 5 to 11 (Supplement figure S8). Thus, the ability to exert gentle but significant mechanical pressure on GUVs in our custom-designed protein hydrogel cages opens up a new way of manipulating vesicle model systems, inducing features that could be of great relevance in the design of cellular mimics, such as shape and differential membrane curvature, respectively tension.

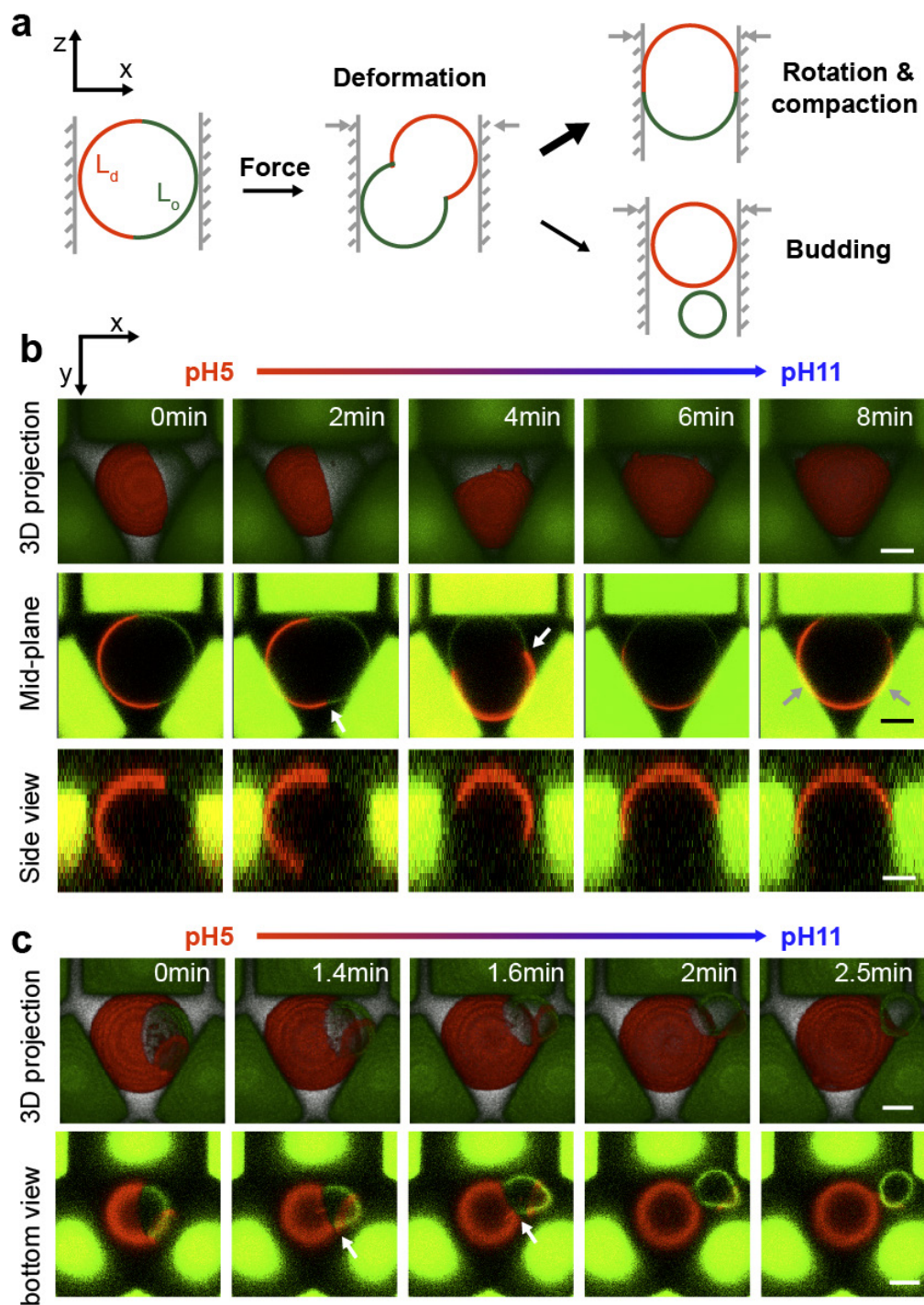


Figure 6. a.) Scheme of dynamic lipid phase reorganization adapting to the space-induced membrane deformation. b.) Dynamic membrane domain reorganization under pH-induced compression in the hydrogel chambers, scale bar 5 μm . c.) Membrane budding driven by the compression of the hydrogel chambers, scale bar 5 μm . GUVs were produced from

DOPC:SM:cholesterol (2:2:1) and labelled with NBD-DSPE (green) and Atto655-DOPE (red). The 3D projections of 3D images were compiled from Z-stack confocal images with ZEN software.

The boundary geometry that determines membrane dynamics, also affects the spatiotemporal patterns and oscillations formed by reaction-diffusion systems.^[27] A striking example of a reaction-diffusion system is the Min protein system, consisting of the proteins MinC, MinD, and MinE, which oscillate between the cell poles and spatially position the bacterial cell division machinery in *Escherichia coli*.^[28] *In vitro* reconstitution of the Min system on micropatterned surfaces or in microcompartments has shown that the geometry of the boundaries plays a pivotal role in its pattern formation and pace-making.^[9, 29] Recently, the Min system has been encapsulated into 3D spherical compartments, motivated by the long-term goal of creating a self-reproducible synthetic cell.^[30] Unlike *in vivo*, this reconstituted reaction-diffusion system reveals several distinct oscillation modes, namely pulsing oscillations, pole-to-pole oscillations and circling and trigger waves.^[30b] Reasons for such diverse behaviours are differences in protein concentration, vesicle size, proteins ratio or the isotropic geometry. Here, we aim to use the 3D hydrogel shaped vesicles to demonstrate how the anisotropy of microenvironment influences the reaction-diffusion system.

We encapsulated the oscillating Min system (MinD (50% EGFP-MinD) & MinE) in negatively charged GUVs (DOPC:DOPG (1,2-dielaidoyl-sn-glycero-3-phospho-(1'-rac-glycerol); molar ratio, 4:1) with an inverted emulsion method (cDICE method^[31]). Subsequently, the vesicles were trapped within the 3D printed protein hydrogel chips. Similar to what has been reported before³³, the majority of the uncompressed vesicles were showing pulsing oscillations, for which all proteins simultaneously oscillated between the vesicle inside and the inner membrane leaflet (**Figure 7a**). After the pH change from 5 to 11, vesicles that did not get deformed by the hydrogel structures, approximately maintained their frequency (Figure 7b and c). However, for vesicles that were compressed, due to the hydrogel swelling we observed an increase in oscillation frequency compared with their uncompressed state (Figure 7 d-f, Supplement Movie S5), which is basically related to the changing aspect ratio (Supplement Figure S9). Larger aspect ratios switching would result in shorter diffusion paths from within the vesicle to the membrane and shorten the period per oscillation. Intriguingly, in some cases the oscillation mode could transit into a different mode in response to the geometry changing (Figure 7g-i). In a vesicle with the pole-to-pole mode, Min

protein initially accumulated on one pole of vesicle. Because of the isotropic property, the wave impartially travelled from two sides and then re-accumulated on another pole. Obviously, pH stimuli compression would trigger the oscillation transiting from pole-to-pole mode to circling (Figure 7g-i, Supplement Movie S6). Min waves never travelled on two sides, but continuously revolved in a single direction on the inside surface of the GUV. The vesicle geometry transformation brought about a protein diffusion mode switching on membrane. Thus, dynamically regulating the anisotropy of spherical vesicles with pH-stimuli 3D hydrogel chip provides us with new mechanical cues for the investigation of reaction-diffusion systems in three-dimensional artificial microenvironments.

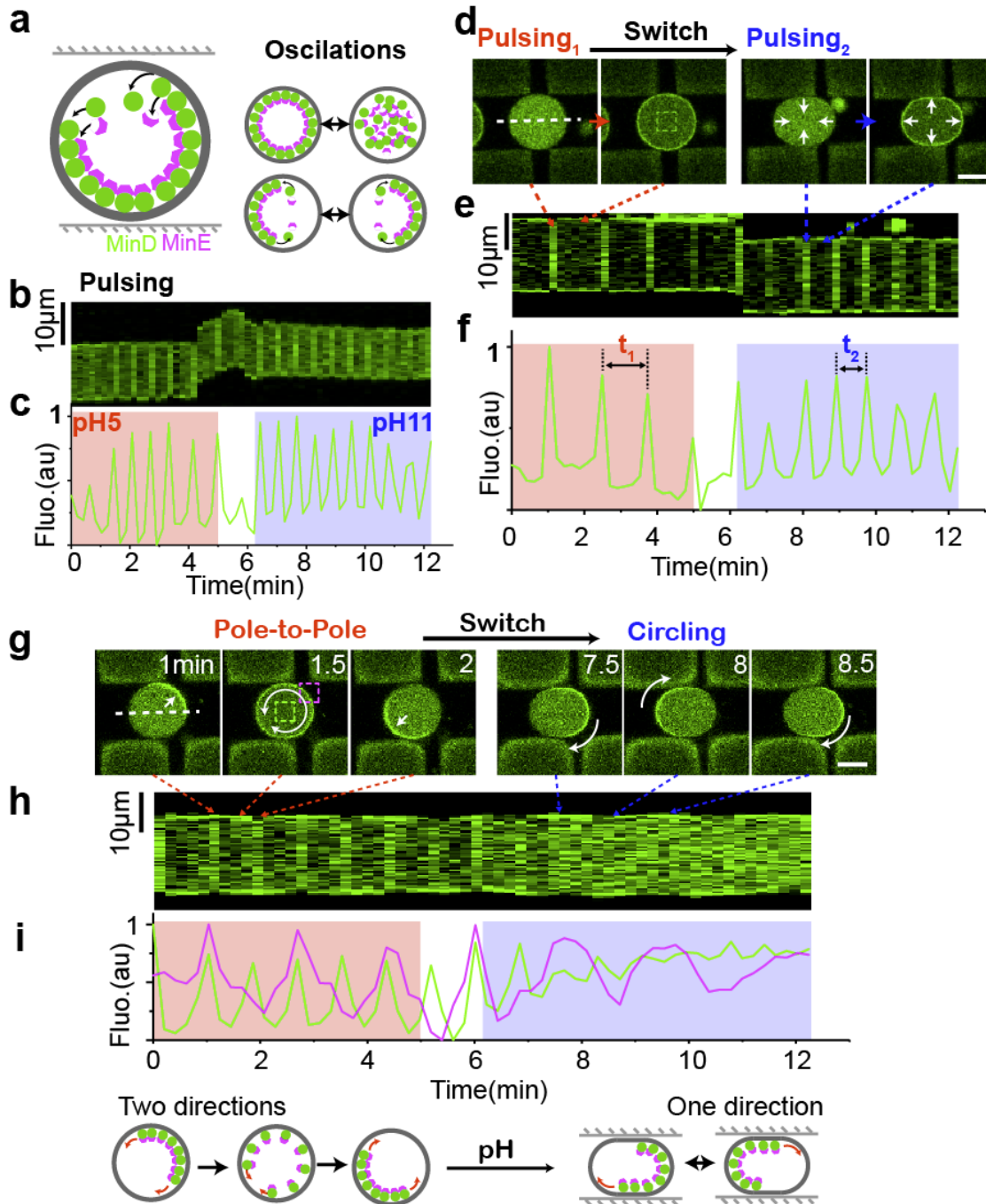


Figure 7. Protein oscillation modes transition in response to change in vesicle geometry. a.) Schematic of Min protein oscillations in vesicles. b-c.) Pulsing oscillation in a spherical vesicle under different pH conditions. d-f.) Pulsing oscillation acceleration during vesicles compression. g-i.) Min oscillation modes transition from pole-to-pole to circling. d., g. and j. show imaging frames from the confocal time series of oscillation (1.5 μ M MinD, 1.5 μ M eGFP-MinD, 3 μ M MinE, 5mM ATP). Scale bar: 10 μ m. b., e. and h. demonstrate the kymograph of the oscillation. The white

dash lines on the vesicles indicate the position for the kymograph analysis. c., f. and i. either describe the fluorescence oscillation inside vesicles (green) or on the membrane (purple). The green and purple dash box show the position for measuring the oscillation curves.

3. Conclusion

We have developed a new toolbox for mechanical manipulation of GUVs - model membrane vesicles, which constitute the basis for the engineering of advanced protocells and that should ideally be subject to defined shape transformations. This is particularly desirable when reconstituting membrane polarity- or shape-dependent protein systems, such as bacterial cell division machineries that request explicitly non-spherical geometries.^[9] Our hydrogel devices are based on custom-printed BSA protein that can be switched by pH, and are thus fully biocompatible. Their dimensions are limited only by the optical resolution of the two-photon laser used for printing. We demonstrated that the swelling ratio depends on the laser power used for printing, such that even more complex designs with differential volume expansion could in principle be realized. This opens up a fully new way of using GUVs as custom-made platforms to probe the functionality of reconstituted cellular modules in bottom-up synthetic biology.

Supporting Information

Supporting Information is available from the Wiley Online Library or from the author.

Conflict of Interest

The authors declare no conflict of interest.

Acknowledgements

H.J. is supported by the GRK2062, Molecular Principles of Synthetic Biology, funded by Deutsche Forschungsgemeinschaft (DFG). H.G.F acknowledges financial support by the DFG within the

SFB 863. This work is carried out in the context of the MaxSynBio consortium jointly funded by the Federal Ministry of Education and Research of Germany and the Max Planck Society.

References

- [1] H. Jia, M. Heymann, F. Bernhard, P. Schwille, L. Kai, *New Biotechnol.* **2017**, 39, 199.
- [2] C. Xu, S. Hu, X. Chen, *Materials Today* **2016**, 19, 516.
- [3] K. Göpflich, I. Platzman, J. P. Spatz, *Trends Biotechnol.* **2018**, 36, 938.
- [4] R. Dimova, Marques, Carlos *The Giant Vesicle Book*, Taylor & Francis Group, **2019**.
- [5] E. Sezgin, I. Levental, S. Mayor, C. Eggeling, *Nat. Rev. Mol. Cell Biol.* **2017**, 18, 361.
- [6] S. K. Vogel, F. Greiss, A. Khmelinskaia, P. Schwille, *Elife* **2017**, 6, e24350.
- [7] M. Dezi, A. Di Cicco, P. Bassereau, D. Lévy, *Proc. Natl. Acad. Sci. U.S.A.* **2013**, 201303857.
- [8] C. Yeaman, K. K. Grindstaff, W. J. Nelson, *Physiol. Rev.* **1999**, 79, 73.
- [9] K. Zieske, P. Schwille, *Elife* **2014**, 3, e03949.
- [10] A. Yamada, S. Lee, P. Bassereau, C. N. Baroud, *Soft Matter* **2014**, 10, 5878.
- [11] J. Korlach, C. Reichle, T. Müller, T. Schnelle, W. Webb, *Biophys. J.* **2005**, 89, 554.
- [12] M. Théry, V. Racine, M. Piel, A. Pépin, A. Dimitrov, Y. Chen, J.-B. Sibarita, M. Bornens, *Proc. Natl. Acad. Sci. U.S.A.* **2006**, 103, 19771.
- [13] M. Bao, J. Xie, A. Piruska, W. T. Huck, *Nat. Commun.* **2017**, 8, 1962.
- [14] B. Kaehr, J. B. Shear, *Proc. Natl. Acad. Sci. U.S.A.* **2008**, 105, 8850.
- [15] P.-S. Li, I.-L. Lee, W.-L. Yu, J.-S. Sun, W.-N. Jane, H.-H. Shen, *Sci. Rep.* **2014**, 4, 5600.
- [16] a) M. R. Lee, I. Y. Phang, Y. Cui, Y. H. Lee, X. Y. Ling, *Small* **2015**, 11, 740; b) C. L. Lay, M. R. Lee, H. K. Lee, I. Y. Phang, X. Y. Ling, *ACS nano* **2015**, 9, 9708.
- [17] T. Robinson, P. Kuhn, K. Eyer, P. S. Dittrich, *Biomicrofluidics* **2013**, 7, 044105.
- [18] D. Stamou, C. Duschl, E. Delamarche, H. Vogel, *Angewandte Chemie* **2003**, 115, 5738.
- [19] B. Sorre, A. Callan-Jones, J.-B. Manneville, P. Nassoy, J.-F. Joanny, J. Prost, B. Goud, P. Bassereau, *Proc. Natl. Acad. Sci. U.S.A.* **2009**, 106, 5622.
- [20] A. Khmelinskaia, H. G. Franquelim, E. P. Petrov, P. Schwille, *J. Phys. D* **2016**, 49, 194001.

-
- [21] T. Peters Jr, *All about albumin: biochemistry, genetics, and medical applications*, Academic press, **1995**.
- [22] D. Hoekstra, O. Maier, J. M. van der Wouden, T. A. Slimane, S. C. van IJzendoorn, *J. Lipid Res.* **2003**, 44, 869.
- [23] K. Bacia, P. Schwille, T. Kurzchalia, *Proc. Natl. Acad. Sci. U.S.A.* **2005**, 102, 3272.
- [24] S. L. Veatch, S. L. Keller, *Biophys. J.* **2003**, 85, 3074.
- [25] A. J. García-Sáez, S. Chiantia, P. Schwille, *J. Biol. Chem.* **2007**.
- [26] F. Jülicher, R. Lipowsky, *Physical review letters* **1993**, 70, 2964.
- [27] a) E. Frey, J. Halatek, S. Kretschmer, P. Schwille, in *Physics of Biological Membranes*, Springer **2018**, p. 229; b) D. Thalmeier, J. Halatek, E. Frey, *Proc. Natl. Acad. Sci. U.S.A.* **2016**, 113, 548.
- [28] M. Loose, E. Fischer-Friedrich, J. Ries, K. Kruse, P. Schwille, *Science* **2008**, 320, 789.
- [29] a) J. Schweizer, M. Loose, M. Bonny, K. Kruse, I. Mönch, P. Schwille, *Proc. Natl. Acad. Sci. U.S.A.* **2012**, 109, 15283; b) K. Zieske, P. Schwille, *Angew Chem. Int. Ed. Engl.* **2013**, 52, 459.
- [30] a) K. Zieske, G. Chwastek, P. Schwille, *Angew Chem. Int. Ed. Engl.* **2016**, 55, 13455; b) T. Litschel, B. Ramm, R. Maas, M. Heymann, P. Schwille, *Angew Chem. Int. Ed. Engl.* **2018**, 57, 16286.
- [31] M. Abkarian, E. Loiseau, G. Massiera, *Soft Matter* **2011**, 7, 4610.
- [32] K. Zieske, J. Schweizer, P. Schwille, *FEBS letters* **2014**, 588, 2545.

Supporting Information

Shaping membrane vesicles in 3D-printed protein hydrogel cages

Haiyang Jia, Thomas Litschel, Michael Heymann, Hiromune Eto, Henri G. Franquelim, Petra Schwille

Table of Contents

Experimental Procedures

Supplement figure S1 to S9

Supplement Movie S1 to S6

References

Experimental Procedures

Preparation of BSA Solution

4.2g bovine serum albumin (BSA) (Lyophilized powder, A7030, Sigma Aldrich) and 1.62 mL of DMSO (18v/v%) were added to 20 mM HEPES buffer to make up a total volume of 9 mL solution. The mixture was centrifuged (20000g) for 15min to remove impurities and foam before use. 85mM rose bengal (Sigma Aldrich, 330000) was prepared separated. The BSA photoresist (420g L⁻¹) was prepared by mixing BSA resin and rose bengal at the ratio of 9:1v/v.

3D BSA Hydrogel printing

3D BSA hydrogel printing was processed with the Nanoscribe Photonic Professional (Nanoscribe GmbH). 3D structures were design with Solidwork. The parameters were defined with Describe. If without specifying, the following parameters were used, laser power: 50mW (100%), scan speed: 30000 $\mu\text{m s}^{-1}$, slicing distance: 0.5 μm , hatching distance: 0.2 μm . All structures were printed with 63x NA1.4 objective in silicone isolator chamber (Thermo Fisher Scientific, 0717104) pasted on round glass coverslip (Diameter= 30mm, thickness #1.5). During printing, the chambers were covered a small coverslip to avoid strong evaporation. After fabrication, structures were rinsed with Phosphate Buffered Saline (PBS) buffer (pH7) to remove the excess BSA resin and photoresist.

Swelling Studies

Five repeat free-form solid cuboids (14x14x15 μm) with slicing distance 0.2–0.8 μm were fabricated with different laser power (30mW-50mW) and scan speed (10000-30000 $\mu\text{m s}^{-1}$). The swelling of structures were observed at different pHs (5-11) using confocal microscope. Structures swelling were studied from low pH to high pH. Structures were equilibrated in different pH solution for 10 minutes before they were transferred for imaging. Areas of the cubes were measure with Fiji (Analyze particles). Then the swelling ratios were calculation as A_{pH}/A_{pH5} , where A means area. Confocal imaging was performed on a commercial Zeiss LSM 780 laser scanning microscope, using a water immersion objective (C-Apochromat, 40 \times /1.2W, Zeiss). Samples were excited with the 561 nm laser.

GUVs preparation

Giant unilamellar vesicles (GUVs) were produced by electroformation in PTFE chambers with Pt electrodes according to the published protocol^[20] with minor changes. Six microliter of lipid mixture (1mg/mL in chloroform) was spread onto two Pt wires and dried in a desiccator for 30 min. The chamber was filled with 350 μ L of an aqueous solution of sucrose (~ 300 mOsm kg⁻¹). An AC electric field of 1.5 V (RMS) was applied at a frequency of 10Hz for 1.5h, followed by 2Hz for 0.25 h. Unless otherwise stated, vesicles composed of DOPC, containing additional 0.5mol% Atto655-DOPE, were electroformed in an aqueous solution of sucrose iso-osmolar compared to imaging buffer (~ 300 mOsm kg⁻¹). For the phase separation, GUVs were prepared from mixtures of DOPC, SM (18:0), and cholesterol (2:2:1) plus 0.2mol% Atto655-DOPE and 0.3mol%NBD-DSPE.

GUVs trapping and shaping

3D structures were exchanged into pH5 PBS buffer (~ 294 mOsm kg⁻¹) for 10min. Then, 20 μ L or more of the GUV suspension (without-diluted) were added on top of the printed structures in the imaging chambers. Samples were incubated for at least 0.5 h at room temperature. After GUVs sinking down and diffusing inside the traps, samples were transferred for imaging. Then, samples were gently equilibrated into pH11 PBS buffer for 10min to reach the maximal swelling. The deformation of the trapped GUVs were imaged with confocal microscopy. To avoid bursting the GUVs during deformation, the osmolality of pH11 PBS buffer (~ 307 mOsm kg⁻¹) was slightly higher than sucrose solution inside GUVs.

Min oscillation in vesicles

1. Proteins

The plasmids for the expression of His-MinD^[28], His-EGFP-MinD^[32] and His-MinE^[28] have been described previously. His-MinD, His-EGFP-MinD and His-MinE were purified according to the published protocols. In brief, proteins were expressed in *E. coli BL21* (DE3) pLysS and further were purified via Ni-NTA affinity purification. Then proteins were further purified using gel filtration chromatography in storage buffer (50mM HEPES, pH 7.25, 150mM KCl, 10% Glycerol, 0.1mM EDTA). Proteins were quick-frozen and stored in aliquots at -80°C until further use.

2. Proteins Encapsulation in vesicles

Min system was encapsulated in vesicles by emulsion transfer (the cDICE method^[31]) according to the published protocol^[30b]. Briefly, both inner and outer solution contain Min protein buffer (25mM tris-HCl (pH 7.5), 150mMKCl and 5mM MgCl₂). In addition, the solution encapsulated in the GUVs contained 1.5 μ M MinD, 1.5 μ M eGFP-MinD, 3 μ M MinE, 5mM ATP, v/v 15% iodixanol (from OptiPrepTM, Sigma Aldrich) and an oxygen scavenger system (3.7U ml⁻¹ pyranose oxidase, 90U/ml catalase, 0.8% glucose. Osmolarity of encapsulated solution was about 560mOsm kg⁻¹, measured with Fiske[®] Micro-Osmometer Model 210). As the GUV-surrounding solution, Min protein reaction buffer and 200 mM glucose were used to match the osmolarity of the inner solution.

The lipid we used is DOPC (1,2-Dioleoyl-sn-glycero-3-phosphocholine, Avanti Polar Lipids, Inc.) and DOPG (1,2-Dioleoyl-sn-glycero-3-phosphoglycerol, Avanti Polar Lipids, Inc.) (Both 25mg ml⁻¹ in chloroform) in a ratio of 4:1. The lipids were mixed in a silicon oil (5 cST) and mineral oil (sigma-aldrich. M5904) mixture (ratio, 4:1).

Then the inner solution was loaded into a 1 mL syringe, which was then placed into a syringe pump system (neMESYS base 120 with neMESYS 290N) and connected through tubing to a glass capillary (100 μ m inner diameter). 700 μ l of outer solution was pipetted into a spinning cDICE chamber, followed by approximately 5ml of the lipid-in-oil mixture. The capillary tip was then immersed in the oil phase and the inner phase injected at a flow rate of 50 μ l h⁻¹ for 15 minutes. The vesicles were withdrawn from the cDICE chamber with a micropipette.

Supplement figures

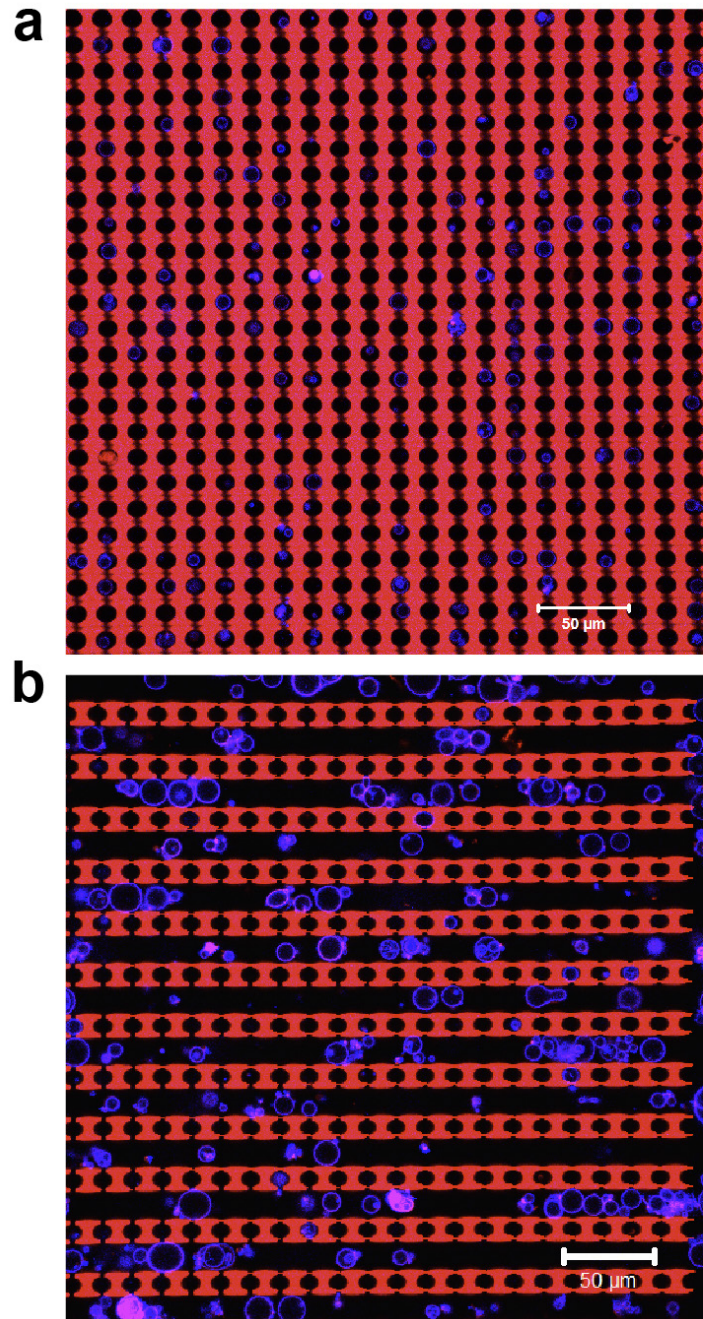


Figure S1. Overviews of the GUVs trapped in a.) The individual trap chip (22x 25 array) and b.) The group trap chip (11 channels), scale bar 50μm. GUVs were produced with DOPC and labelled with 0.5mol% Atto655-DOPE.

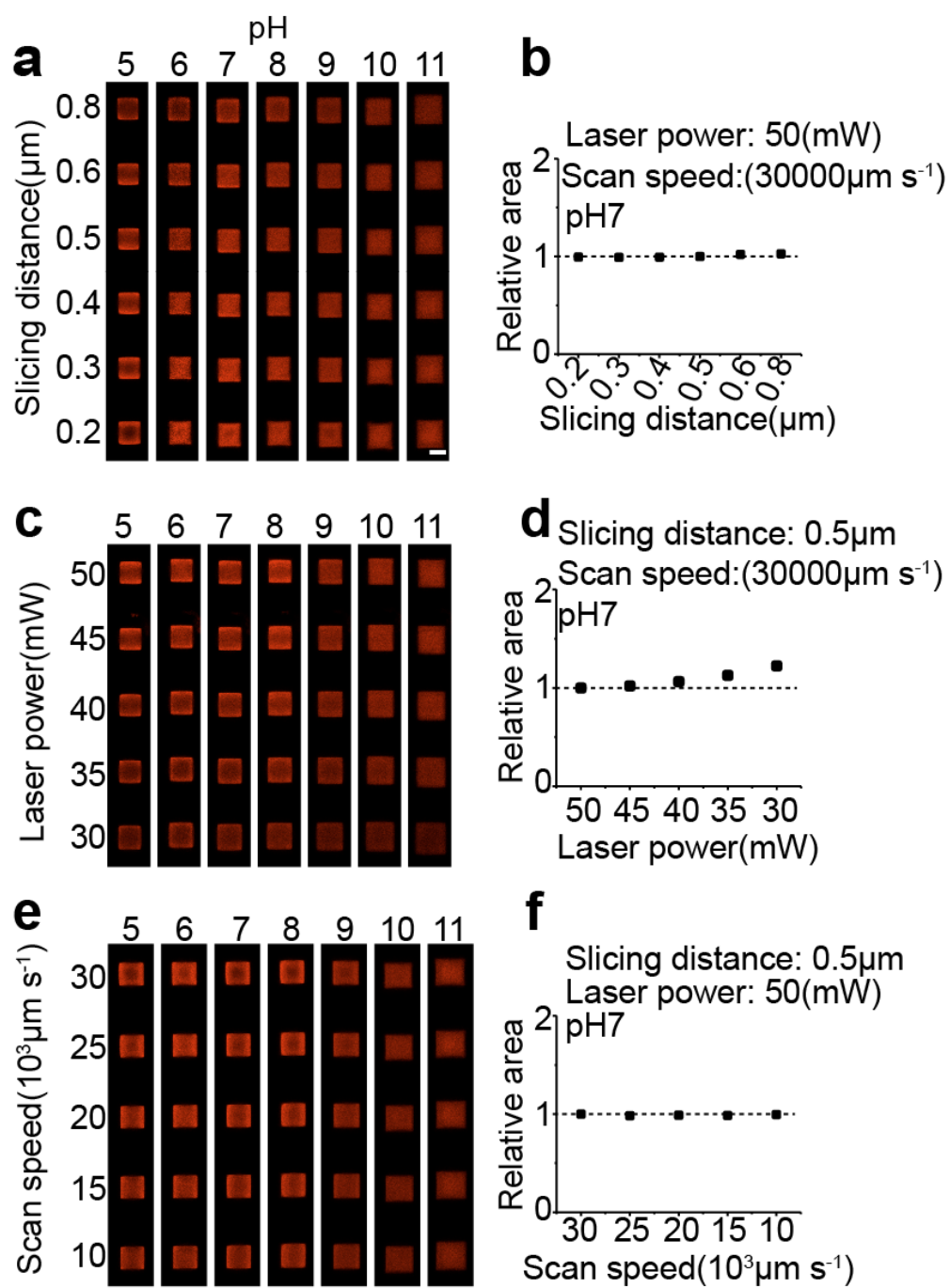


Figure S2. pH-dependent swelling of 3D printed cubic hydrogels fabricated with different fabrication parameters a.) pH responsive swelling of hydrogel cube with different slicing distances from 0.2 to 0.8 μm (Laser power: 50mW, Scan speed: 30000 $\mu\text{m s}^{-1}$), scale bar 10 μm . b.) relative area of structures printed with different slicing distance at pH7. The slicing distance will not influence printing size of the structures. c.) pH responsive swelling of hydrogel cube with different laser power from 30 to 50mW (Slicing distance: 0.5 μm , Scan speed: 30000 $\mu\text{m s}^{-1}$). d.) Relative area of structures printed with different laser power at pH7. Printing with laser power lower than 40mW increased structure size. e.) pH responsive swelling of hydrogel cube with different laser scan speed from 10000 to 30000 $\mu\text{m s}^{-1}$ (Slicing distance: 0.5 μm ; laser power: 50mW). f.) Relative area of structures printed with different scan speed at pH7. The relative area calculated with A/A_0 , where A_0 means the area of structure printed with fabrication parameters (Slicing distance: 0.5 μm , Laser power: 50mW, Scan speed: 30000 $\mu\text{m s}^{-1}$).

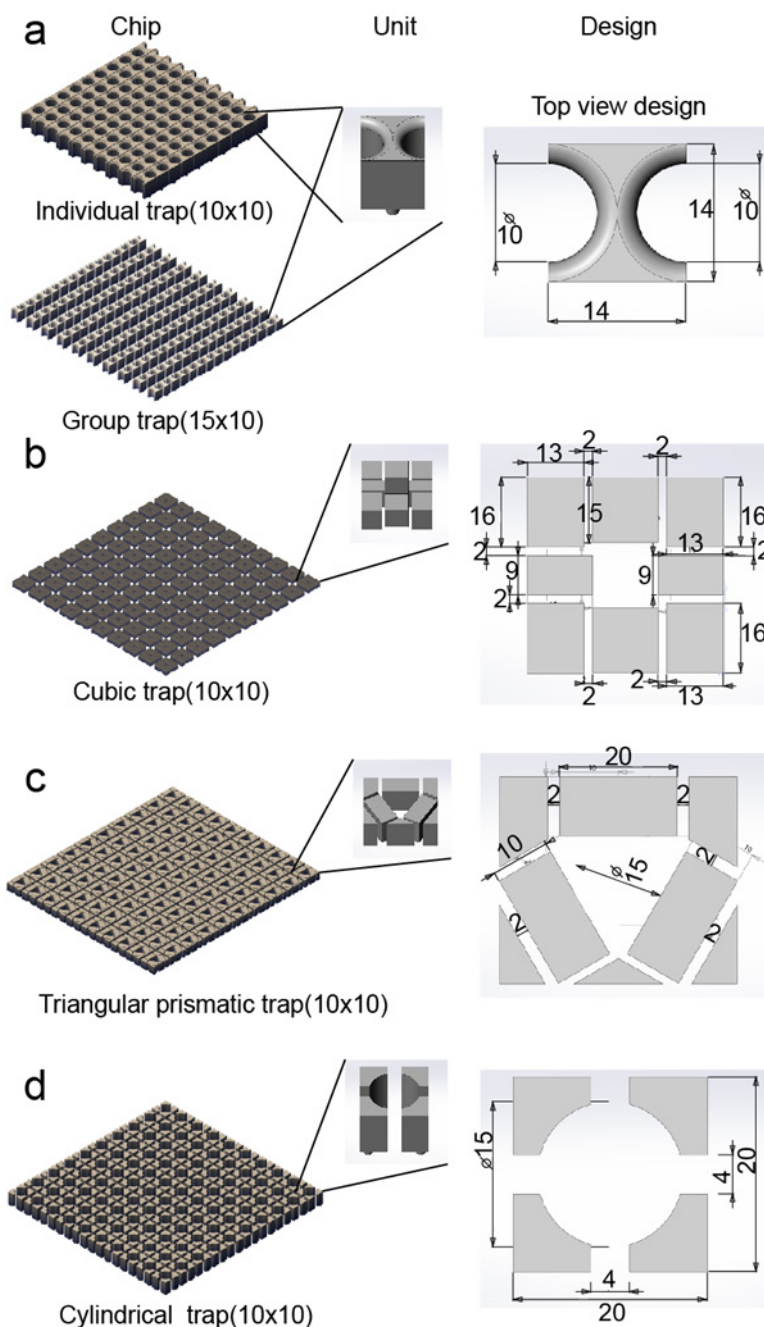


Figure S3. Schematic designs and dimensions of 3D protein hydrogel traps a.) Individual traps with 10x10 array in Fig. 1a. and group traps in Fig. 1b ,c, Fig.3 . b. and Fig.6.) Cubic traps with a 10x10 array in Fig.2f and Fig. 4. c.) Triangular prismatic traps with a 10x10 array in Fig. 4 and Fig. 5. d.) 10x10 cylindrical traps array in Fig. 4. If without specifying, all the structures used in this research are freestanding designs with pillars as supports (Diameters $2\mu\text{m}$, Height $2\mu\text{m}$)

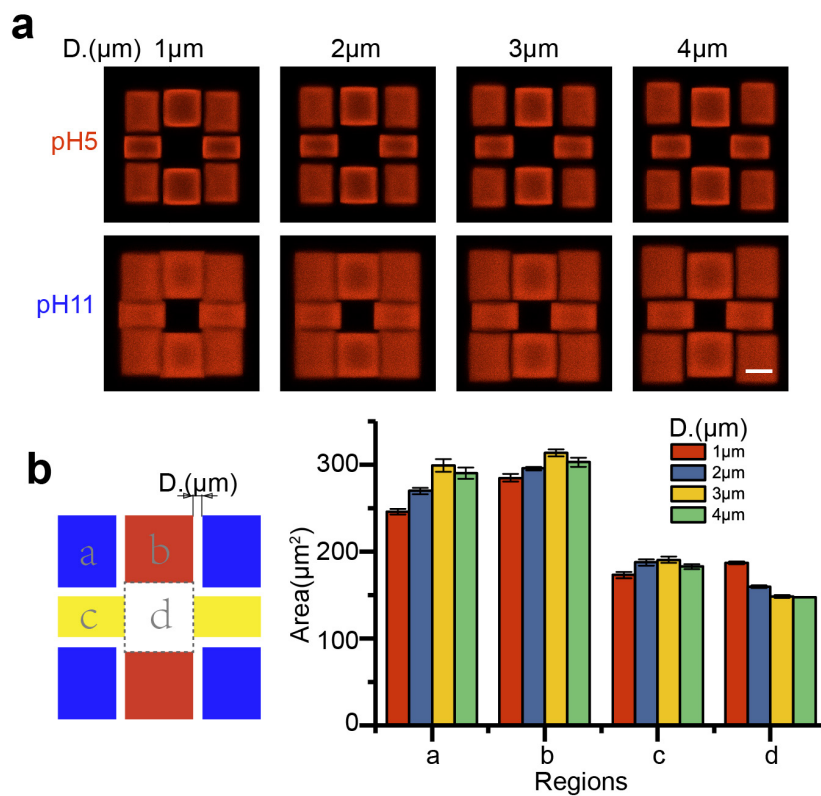


Figure S4. Distances between modules influence structure swelling capability. a.) pH responsive swelling of cubic traps with different distances between modules, scale bar, 10 μm . b.) Area swelling of different regions in the cubic trap with different distances, when pH was changed from 5 to 11. Module b and c are freestanding structures with pillar supports. Module a were cuboid without pillar supports.

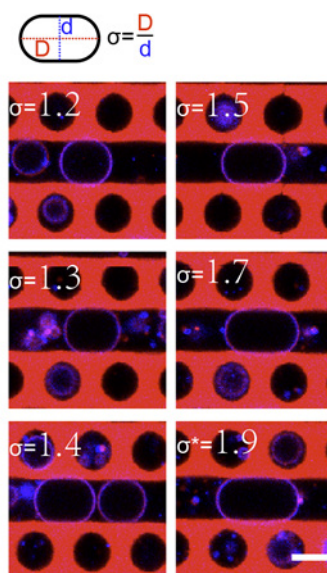


Figure S5. Swelling hydrogel compressing GUVs with different aspect ratios σ (width compared to length), scale bar $10\mu\text{m}$. The deformation of GUVs were processed in the group trap chip. Due to the size difference, GUVs with different aspect ratio can be obtained from the swelling compression. * GUV (Diameter $> 15\mu\text{m}$) trapped in the chip had been compressed at pH5.

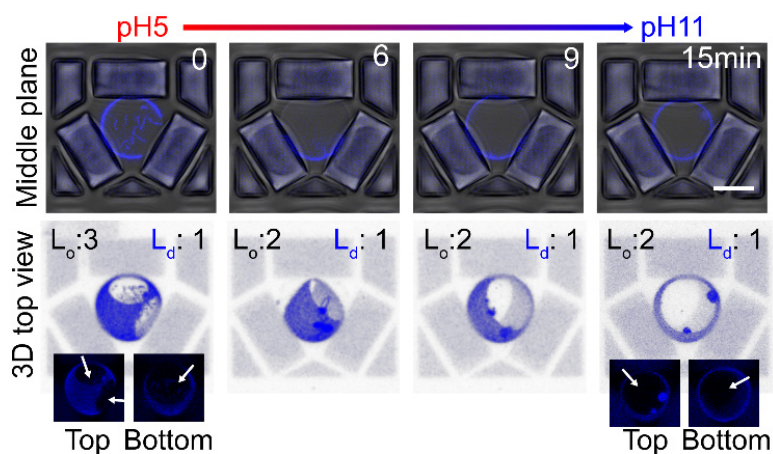


Figure S6. Dynamic lipid domain fusion and reorganization adapting to the space-induced membrane deformation, Scale bar, 10 μ m. Top: confocal images of middle plane of the vesicle. Bottom: top view of the 3D z-stack reconstitution. The numbers show the domain numbers of L_o and L_d phase. GUVs were produced from DOPC:SM:cholesterol (2:2:1). GUV in the images was labelled with Atto655-DOPE (blue).

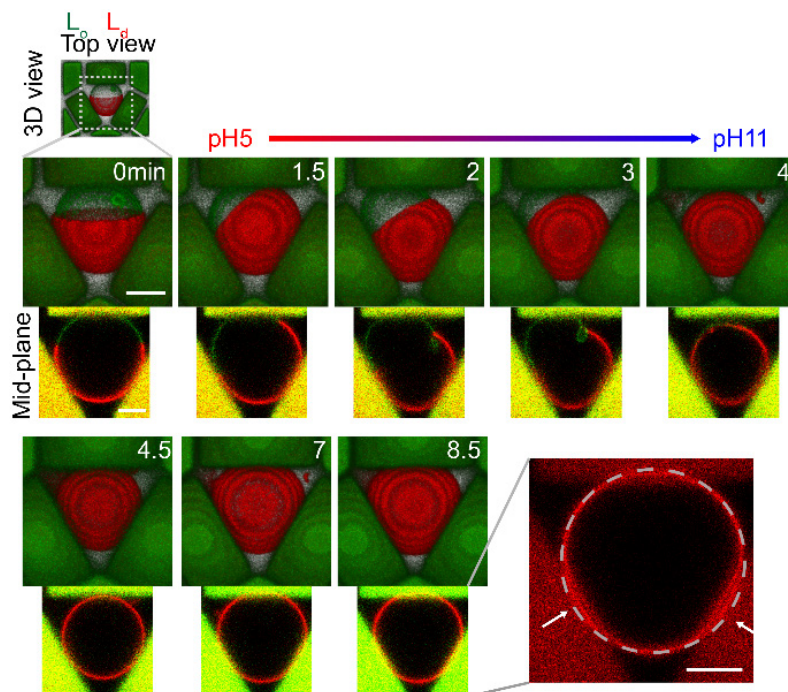


Figure S7. Dynamic membrane domain reorganization under pH-induced compression in the hydrogel chambers, scale bar 5 μ m. GUVs were produced from DOPC:SM:cholesterol (2:2:1) and labelled with NBD-DSPE(green) and Atto655-DOPE (red). The top views of 3D images were compiled from Z-stack confocal images with ZEN software.

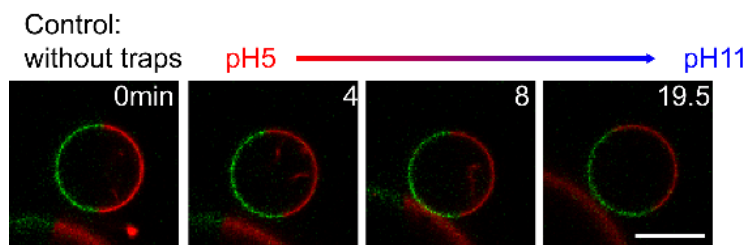


Figure S8. Free standing phase-separated GUVs upon pH stimuli, scale bar, 10 μ m. GUV in the images was labelled NBD-DSPE (green) and Atto655-DOPE (red).

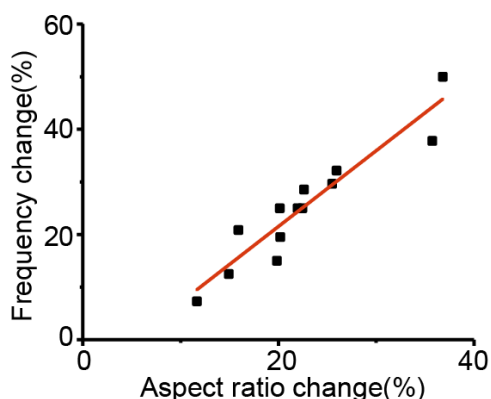


Figure S9. Pulsing oscillation acceleration during vesicles compression (1.5 μ M MinD, 1.5 μ M eGFP-MinD, 3 μ M MinE, 5mM ATP). Pulsing frequency change versus aspect ratio (W/H) change of vesicles that were before- and after- compressed.

Supplement Movies

Supplement Movie S1. pH responsive swelling of group trap, when pH was shift from 5 to 11.

Supplement Movie S2. Dynamic membrane phase separation and reorganization in pH-stimuli 3D hydrogel chamber (top view)

Supplement Movie S3. Dynamic membrane phase separation and reorganization in pH-stimuli 3D hydrogel chamber (orthogonal view)

Supplement Movie S4. Membrane budding driven by the space compression of the pH-stimuli 3D hydrogel chambers (top view)

Supplement Movie S5. Pulsing oscillation acceleration during vesicles compression

Supplement Movie S6. Min oscillation modes transition from pole-to-pole to circling.

References

- [1] A. Khmelinskaia, H. G. Franquelim, E. P. Petrov, P. Schwille, *J. Phys. D* **2016**, 49, 194001.
- [2] M. Loose, E. Fischer-Friedrich, J. Ries, K. Kruse, P. Schwille, *Science* **2008**, 320, 789.
- [3] K. Zieske, J. Schweizer, P. Schwille, *FEBS letters* **2014**, 588, 2545.
- [4] M. Abkarian, E. Loiseau, G. Massiera, *Soft Matter* **2011**, 7, 4610.
- [5] T. Litschel, B. Ramm, R. Maas, M. Heymann, P. Schwille, *Angew Chem. Int. Ed. Engl.* **2018**, 57, 16286.

Manuscript

3D space regulation tools:

2.4 Active forces driving 4D protein hydrogel origami

The results discussed in this section are unsubmitted manuscript.

In this manuscript, we engineered nanoscale actomyosin motor system to drive rapid microscale transformation between complex 3D printed hydrogel scaffolds by active contraction.

This is a research project in collaboration with Dr. Michael Heymann, Dr. Sven Vogel, Dr. Henri Franquelim, Dr. Frank Siedler, Hiro Eto in Schwille group, and Johannes Flommersfeld, David Brueckner in Prof. Chase Broedersz' group(LMU). Haiyang Jia is only first author for this manuscript. The author list and contributions will be determined when we are ready for submission.

Active forces driving 4D protein hydrogel origami

Haiyang Jia et.al.

Four-dimensional (4D) printing with soft materials capable of self-actuating and stimuli-actuating shape-morphing have applications in diverse areas, such as flexible electronics(1, 2), smart textiles(3), soft robotics(4, 5), biomedical devices(6), drug delivery(7) and tissue engineering(8). Rationally actuating shape transforming is essential for all such applications to accomplish the functions for which they are designed. Over the past few decades, there has been considerable progress in developing new actuation technologies, including those based on electrostatic forces(9, 10), thermal expansion(11), magnetostriction(12), and pressure. Most artificial actuators are easy to modulate remotely with external stimuli and enable miniaturization down to microscale; however, are considerably limited by either spatial scale, accurately control, triggering efficiency, or biocompatibility(13).

The natural analogues of active actuators are exemplified by nanoscale molecular motors, which are assembled into multiscale ensembles with integrated control systems. These systems can scale force production from piconewtons up to kilonewtons to govern active motion of cells, tissues and organs. By leveraging the performance of living cells and tissues and directly interfacing them with biocompatible soft materials, biohybrid and bioinspired robots were created from top-down to perform behaviors like natural systems, such as cellular micropump(14), a crab-like microrobot(15), myopod(16), “jellyfish”(17) and soft-robotic ray(5). Due to the scale limitation of cell or tissue, bio-hybrid actuators with living materials still represent a considerable bottleneck for many applications and hampers the development of advanced robots at nanometer- and micrometer-scale. Compared with the top down approaches, recently the emerged bottom-up reconstitution of well-characterized functional biomaterials, provide new chance to engineer nanoscale biohybrid actuators from molecular entities, parts and modules in a simple way. So far, a minimal system consisting of filamentous actin (F-actin) and myosin-II motors was reconstituted *in vitro* system(18). Active forces can be generated upon energy supplying, resulting in rapid actomyosin contractions that are able to introduce deformation in soft materials such as model membrane. The ability to efficiently produce detectable forces at molecular scales is the most exciting feature, which makes them as attractive biohybrid actuators candidates for all the

applications in which microrobots/nanorobots endowed with onboard propulsion systems are desirable.

Here we engineered nanoscale actomyosin motor system to drive rapid microscale transformation between complex 3D printed hydrogel scaffolds by active contraction. Our 3D hydrogel structures composed of photo-crosslinked protein were fabricated in a two-photon polymerized layer-by-layer procedure from photoresist resin containing bovine serum albumin (BSA) and rose bengal as photoinitiator (Figure 1a). By varying the fabrication laser power and scan speed, the elastic modulus of the resulting protein hydrogel structures could be tuned from 10kPa to 250kPa, a range that encompasses modulus values for a number of biological tissues, such as basement membrane and mammalian muscle (19, 20). To immobilize actomyosin motor system, the active surface of the protein hydrogel was accomplished by mixing biotinylated BSA into the photoresist resin.

Then we developed an actin network consisting of Alexa488-phalloidin stabilized actin filaments coupled onto the biotinylated hydrogel microstructures via biotin-neutravidin bonds (Figure 1a). Free form neutravidin (neutravidin/biotin-actin; 1:20) served as crosslinker to integrate individual actin filaments into mesh network, which endures the proper self-organization of our actin cortex in 3D space volumes. Actin networks as a spatial cue connected different parts of 3D structures and further supported the contractility of myosin motor on 3D hydrogel structures. By varying the amount of biotinylated BSA present in the photoresist resin, we could control over the density of the immobilized actin on the 3D scaffolds (Figure 1b). To demonstrate the ability to actuate the shape-morphing of 3D hydrogel structures, a soft pillar ring containing ten standing pillars was designed and printed with elastic modulus about 57kPa (Figure 1b). Three dimensional actin network crosslinked with neutravidin was reconstituted onto the biotinylated pillar ring. We then tested the response of the pillar supported actin network upon addition of myosin motors. Subsequently, pillars were almost homogeneously bended immediately to the center in an ATP-dependent manner, showing the diameter decreasing on tip of the pillar ring (Figure 1c, d), with the varied contraction velocity (Figure 1e). As a force motor, myofilaments slid on actin filaments, contracted the actin network, and collectively led to material response. During this progress, forces generated at the molecular level by motor proteins were transmitted by actin networks, resulting in large-scale active stresses on 3D microstructures. We then tuned the stiffness of pillar ring to further investigate the contractility of our motor system in response to the material elasticity changes (Figure 1f-g). Pillar rings with different elastic modulus showed different bending

curvatures (Figure 1g). In experiments, large displacements were detected in the pillar rings with elastic modulus under 100kPa. Through fitting structural curvatures with the elastic model, the force on the each pillar was about 200 ± 25 pN. We employed the finite-element analysis of the commercial software Solidworks to understand the large-scale force transition coordinated with the 3D structure transformation. The simulation conducted under the same conditions, including the hydrogel properties and generated force in the experiments, is in good agreement with the experimental results, which provides the possibility to program complex 3D structures by utilizing finite-element simulation (Figure 1g). Through changing material properties, we rationally turned the actuated displacements, laying the ground for designing complex 3D structure with controllable transformation.

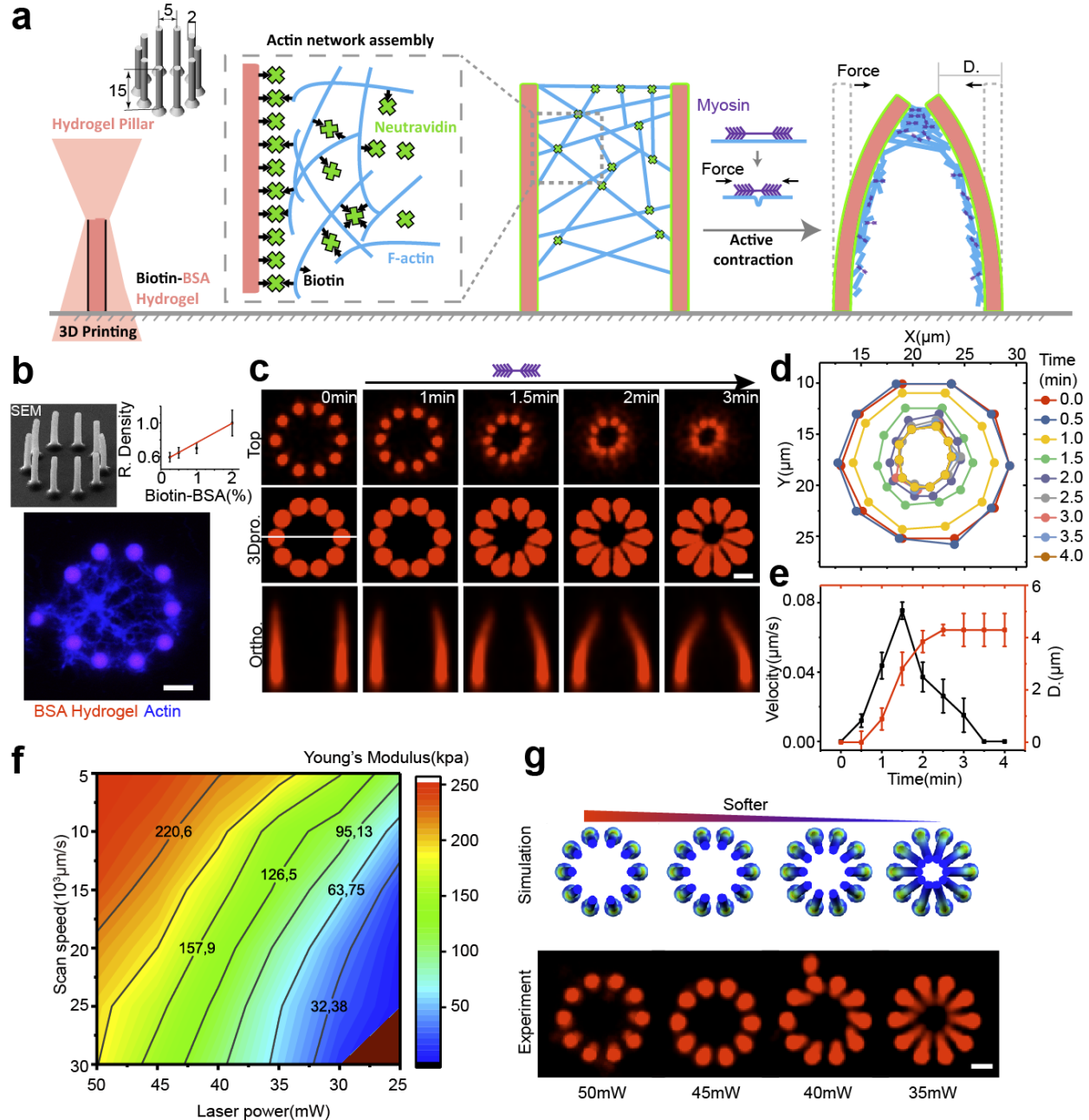


Figure 1 Validating actin-myosin actuator on 3D printed BSA hydrogel. a.) Illustration depicting 3D protein hydrogel printing procedure and the coupling of actin network to 3D scaffold. b.) Top: Scanning electron microscope (SEM) imaging of pillar ring and effect of the biotin-BSA ratio on the immobilized actin density. Bottom: z projection of actin network organization on pillar ring, scale bar $5\mu\text{m}$. c.) Contractile dynamics of pillar ring in response to the motor addition. Scale bar, $5\mu\text{m}$. d.) Pillar ring contraction analysis. Each circle represents a time point. e.) Pillar bending displacement and motion velocity during contraction. f.) Young's modulus map of the hydrogel

structures by varying printing parameters. g.) Simulation of the finite-element model and experiments results. Scale bar, 5 μ m.

Actin network architecture, such as size of and distance between nucleation points, can influence actomyosin contractility (22, 23). In our setup, individual pillars can be considered as a nucleation cluster. In order to program large-scale hydrogel contraction with the actomyosin actuator, we further investigated the effect of the geometrical boundaries, such as distances. To evaluate the respective contribution of distance to the contractility, we varied the ring diameter (D) and pillars' distance (d) (Figure 2a-b). When D and d increased equally, uniform contraction can only be performed on the rings with diameters $\leq 26\mu\text{m}$ (Figure 2a). For the ring with larger diameters, pillar contraction will differentiate into different groups, not integrate as a whole, meaning distance either the ring diameter or pillars' distance will influence integrity and consistency of the contractility. Additionally, the amount of the contracted pillar-clusters increased along with d increasing, demonstrating larger distance between neighbor pillars would amplify the differentiation. Intriguingly, when d was kept constant and D was increased by varying pillar number, a similar threshold was detected in the ring with diameter around 26 μm (Figure 2b). All the results demonstrate that unanimous contraction of the protein hydrogel structures is determined by the distance of actin supporting sites.

Another factor needed to be considered is torque that was determined by the angle between the force vector and the lever arm vector. To characterize the effect of angle on the actomyosin based active contraction, we designed a free-standing V structure with two stiff arms that were connected with a soft joint in the middle. One arm was fixed with a solid support, leaving the only freedom for another arm. When the actin-myosin network contracted and transmitted force to the arms. The force would prefer bending the soft joint, than the stiff arm, resulting in the folding movement of the freeform arm about the joint towards the fixed arm. The results show the active force based V structure folding can be accomplished from 45° up to 160° (Figure 2c).

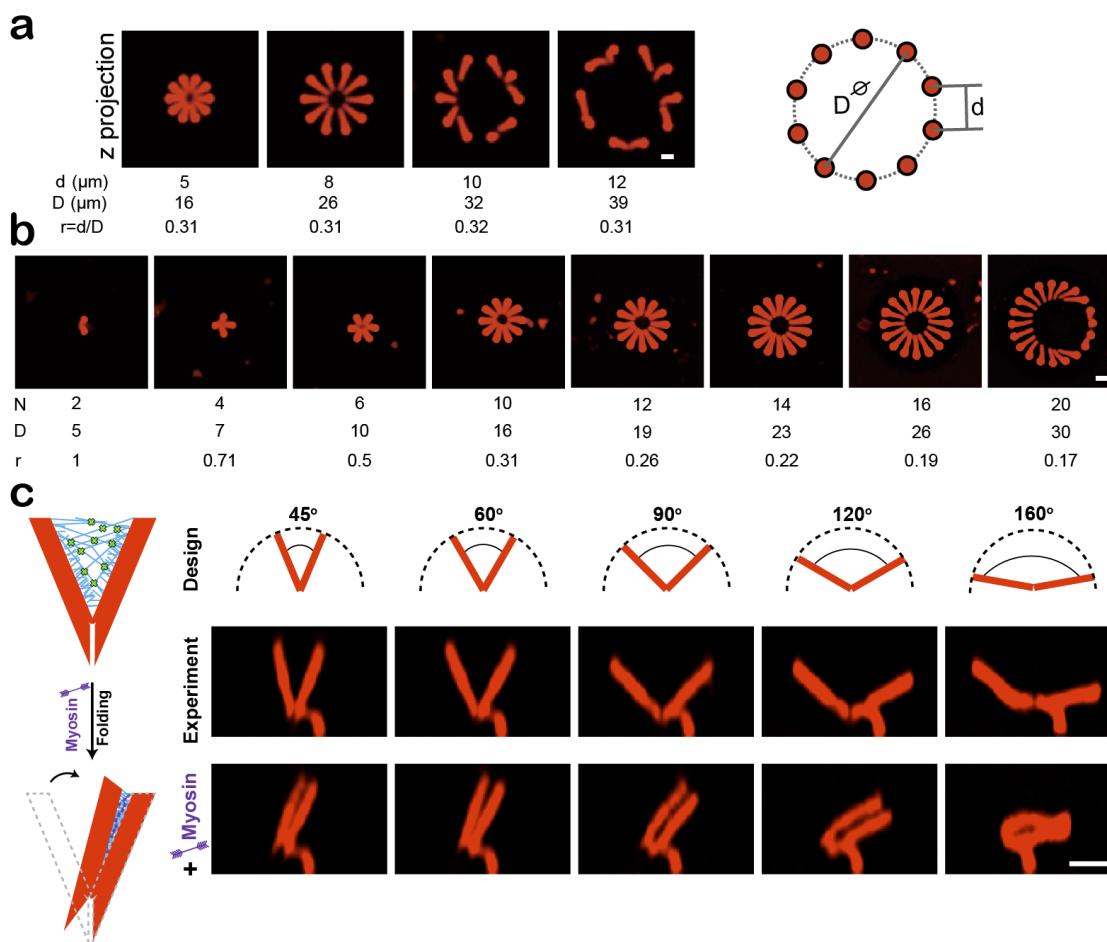


Figure 2 Geometrical properties determine active contraction of 3D printed structures. a.) Distance of nucleation sites and b.) size of pillar rings limit unanimous contraction. Scale bar, $5\mu\text{m}$. Pillar number was kept constant at 10 in a. Distance of nucleation sites was fixed at $5\mu\text{m}$ in b. c.) The active contraction of V structures. Scale bar, $5\mu\text{m}$. All structures were printed with laser power about 35mW and scan speed around $30000\mu\text{m/s}$, resulting in elastic modulus around 57kPa .

Active contraction of simple 3D hydrogel units was determined by the geometrical boundaries, such as size and angle, but not limited to them. Large-scale and intricate active contraction can be amplified by rationally assembling simple modules, the unit coordination of which would yield a high efficient and programmable shape-morphing under active force. As Fig. 3a illustrated, by combining V units that generate small scale folding, we created a series of functional folding architectures to demonstrate the programmable capabilities of large-scale folding. Basic V units were combined to be a V-wave and their connection sites were fixed to permit folding only on the

joints. The actomyosin actuator would simultaneously drive all the independent V units folding, resulting in rapid upwards curling (Figure 3a). Instead of using a large angle hinge with low folding ability, 90° and 135° angle folding can be accomplished alternatively by assembling two or three 45° V-unit (Figure 3a). Additionally, impossible large angle folding with the simple unit, such as 180° and 360°, can also be successfully accomplished by the unit combination. Complex combination such as two W structure assembled with four 45° V-unit in a row could rapidly transform into its contractile state within four minutes. V-wave combined with 6 V-unit could revolve about the first joint on the right, coil up its long V-chain and final turn 360° to form a closed hexagonal star (Figure 3a). Through combination, large 3D hydrogel structures with up to 60µm in length can still be successfully contracted without limitation, showing the possibility for programming large structural transformation. We further demonstrate actomyosin actuator render other capabilities to 3D hydrogel structures such as spring-like contraction. As another form of V-unit combination, hydrogel spring with more freedom was contracted along its axis under myosin triggering (Figure 3b).

Our method can be further extended to more intricate origami-like shape-morphing, such as self-folding a hydrogel box. The cruciform precursor was created by using a combination of flat panels and hinges. The solid supported central face was connected to the other five free-standing faces with inner hinges (Figure 3c). An extra rigid block was placed between the two hinging faces to serve as a sill for controlling folding-angle. Additionally, the flat panels and the rigid block formed a 90° angle, which allowed a simple self-folding sheet efficiently yield a complex 3D cube under active contraction.

The ideas presented here combine 3D printing biocompatible soft materials with bottom-up reconstituted nanoscale bio-motors to enable large scale shape-morphing of complex 3D microstructures. Our study is but a first step in engineering and programming bio-motor based actuator that are compatible and can be implemented with other soft materials, suggesting new possibilities for applications in biomedical devices and soft robotics.

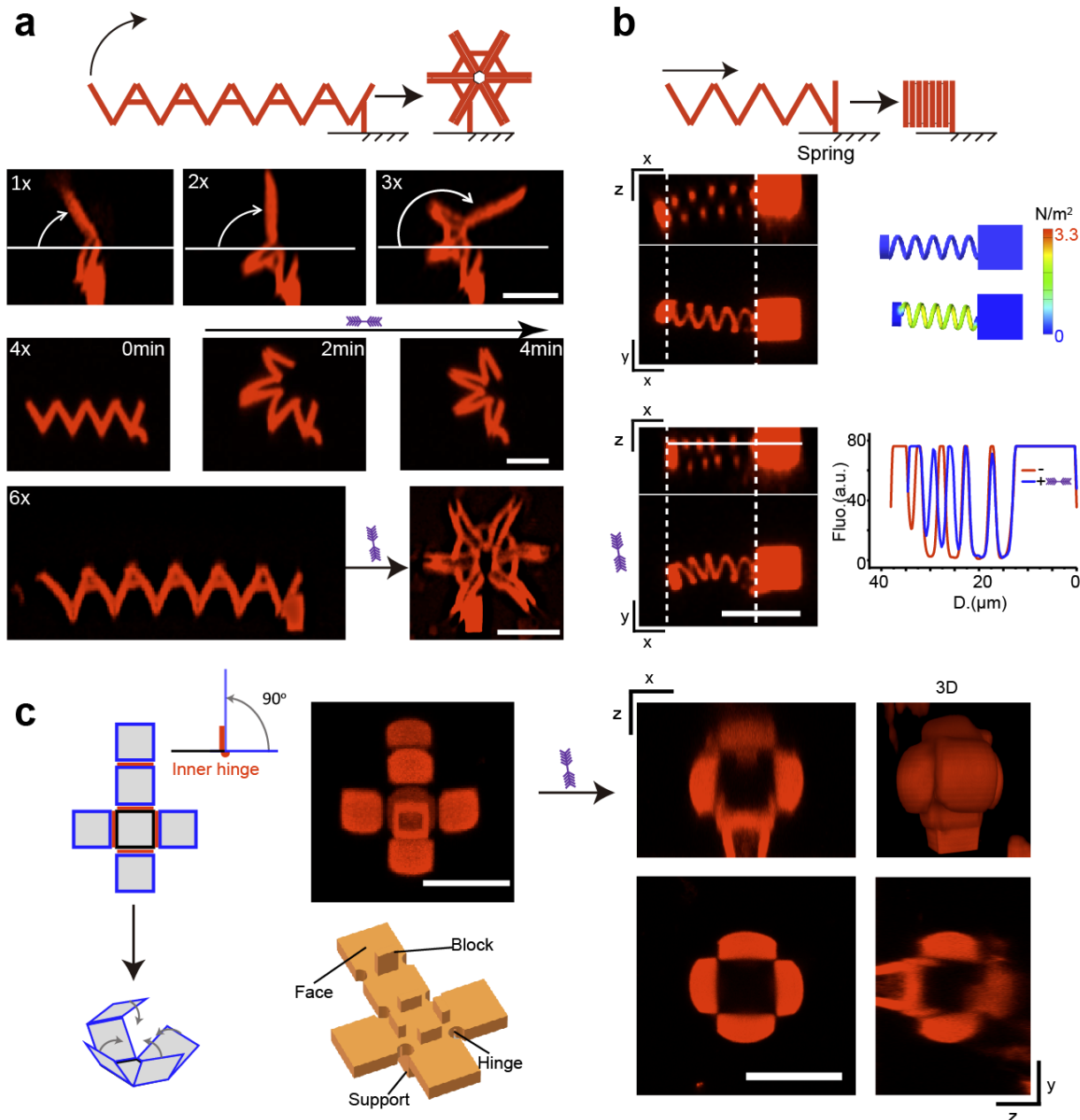


Figure 3 Large-scale and intricate transformations of 3D structures programmed with active contraction. a.) Schematic design and experimental results of V-unit combination demonstrating complex coiling dynamics under applied active force. Scale bar, $20\mu\text{m}$. b.) Schematic design and experimental results of a contractile protein hydrogel spring. The plot represents the spring contraction along its axis before and after triggering. c.) An intricate cube self-folding from its cruciform precursor. The orthogonal view and 3D imaging reconstitution demonstrate the closed cube under active force actuating. Scale bar, $20\mu\text{m}$.

References and Notes:

1. M. Ma, L. Guo, D. G. Anderson, R. Langer, Bio-inspired polymer composite actuator and generator driven by water gradients. *Science* **339**, 186-189 (2013).
2. M. Zarek *et al.*, 3D printing of shape memory polymers for flexible electronic devices. *Advanced Materials* **28**, 4449-4454 (2016).
3. J. Hu, H. Meng, G. Li, S. I. Ibekwe, A review of stimuli-responsive polymers for smart textile applications. *Smart Materials and Structures* **21**, 053001 (2012).
4. M. Wehner *et al.*, An integrated design and fabrication strategy for entirely soft, autonomous robots. *Nature* **536**, 451 (2016).
5. S.-J. Park *et al.*, Phototactic guidance of a tissue-engineered soft-robotic ray. *Science* **353**, 158-162 (2016).
6. C. L. Randall, E. Gultepe, D. H. Gracias, Self-folding devices and materials for biomedical applications. *Trends in biotechnology* **30**, 138-146 (2012).
7. R. Fernandes, D. H. Gracias, Self-folding polymeric containers for encapsulation and delivery of drugs. *Advanced drug delivery reviews* **64**, 1579-1589 (2012).
8. B. Grigoryan *et al.*, Multivascular networks and functional intravascular topologies within biocompatible hydrogels. *Science* **364**, 458-464 (2019).
9. G. H. Kwon *et al.*, Biomimetic soft multifunctional miniature aquabots. *Small* **4**, 2148-2153 (2008).
10. S. Taccola *et al.*, Toward a new generation of electrically controllable hygromorphic soft actuators. *Advanced Materials* **27**, 1668-1675 (2015).
11. Z. Ding *et al.*, Direct 4D printing via active composite materials. *Science advances* **3**, e1602890 (2017).
12. Y. Kim, H. Yuk, R. Zhao, S. A. Chester, X. Zhao, Printing ferromagnetic domains for untethered fast-transforming soft materials. *Nature* **558**, 274 (2018).
13. L. Hines, K. Petersen, G. Z. Lum, M. Sitti, Soft actuators for small - scale robotics. *Advanced materials* **29**, 1603483 (2017).
14. Y. Tanaka *et al.*, An actuated pump on-chip powered by cultured cardiomyocytes. *Lab on a Chip* **6**, 362-368 (2006).
15. J. Kim *et al.*, Establishment of a fabrication method for a long-term actuated hybrid cell robot. *Lab on a Chip* **7**, 1504-1508 (2007).
16. A. W. Feinberg *et al.*, Muscular thin films for building actuators and powering devices. *Science* **317**, 1366-1370 (2007).
17. J. C. Nawroth *et al.*, A tissue-engineered jellyfish with biomimetic propulsion. *Nature biotechnology* **30**, 792 (2012).
18. S. K. Vogel, Z. Petrasek, F. Heinemann, P. Schwille, Myosin motors fragment and compact membrane-bound actin filaments. *Elife* **2**, e00116 (2013).
19. B. C. W. Kot, Z. J. Zhang, A. W. C. Lee, V. Y. F. Leung, S. N. Fu, Elastic modulus of muscle and tendon with shear wave ultrasound elastography: variations with different technical settings. *PloS one* **7**, e44348 (2012).
20. T. Mirfakhrai, J. D. Madden, R. H. Baughman, Polymer artificial muscles. *Materials today* **10**, 30-38 (2007).
21. P. Ronceray, C. P. Broedersz, M. Lenz, Fiber networks amplify active stress. *Proceedings of the national academy of sciences* **113**, 2827-2832 (2016).

22. A.-C. Reymann *et al.*, Actin network architecture can determine myosin motor activity. *Science* **336**, 1310-1314 (2012).
23. T. Vignaud, L. Blanchoin, M. Théry, Directed cytoskeleton self-organization. *Trends in cell biology* **22**, 671-682 (2012).

Acknowledgments:

H.J. is supported by the GRK2062, Molecular Principles of Synthetic Biology, funded by Deutsche Forschungsgemeinschaft (DFG). H.G.F acknowledges financial support by the DFG within the SFB 863. This work is carried out in the context of the MaxSynBio consortium jointly funded by the Federal Ministry of Education and Research of Germany and the Max Planck Society.

Materials and Methods

Preparation of BSA Solution

3.8g bovine serum albumin (BSA) (Sigma Aldrich) and 1% Biotinylated-BSA(ThermoFisher) and 1.62 mL of DMSO (18v/v%) were added to 20 mM HEPES buffer to make up a total volume of 9 mL solution. The mixture was centrifuged (20000g) for 15min to remove impurities and foam before use. 85mM rose bengal (Sigma Aldrich, 330000) was prepared separated. The BSA photoresist (380g L⁻¹) was prepared by mixing BSA resin and rose bengal at the ratio of 9:1v/v.

3D BSA Hydrogel printing

3D BSA hydrogel printing was processed with the Nanoscribe Photonic Professional (Nanoscribe GmbH). 3D structures were design with Solidwork. The parameters were defined with Describe. If without specifying, the following parameters were used, laser power: 35mW (70%), scan speed: 30000μm s⁻¹, slicing distance: 0.3μm, hatching distance: 0.2μm. All structures were printed with 63x NA1.4 objective in silicone isolator chamber (Thermo Fisher Scientific, 0717104) pasted on round glass coverslip (Diameter=30mm, thickness #1.5). During printing, the chambers were covered a small coverslip to avoid strong evaporation. After fabrication, structures were rinsed with Phosphate Buffered Saline (PBS) buffer (pH7) to remove the excess BSA resin and photoresist.

Young's modulus measurement with Atomic Force Microscopy(AFM)

AFM was performed on a JPK Instruments Nanowizard III BioAFM mounted on a Zeiss LSM510 Meta laser scanning confocal microscope (Jena, Germany). Non-coating silicon cantilevers (XNC12/CR-AU B, MikroMasch) were used for the quantitative imaging (QI) mode and force spectroscopy. Data was analyzed using JPK data processing software Version 5.1.4 (JPK Instruments). The modulus was obtained by fitting the extended part of the force–penetration curves with a simple Hertz model (JPK data analysis software).

Scanning Electron Microscopy (SEM) imaging of hydrogel

To prepare sample for SEM imaging, BSA microstructures were exchanged into acetone sequentially with increasing serial concentrations (20%, 40%, 60%, and 100%). The samples were then dried with Leica EM CPD300 Automated Critical Point Dryer after immersing in pure acetone. Samples were sputter coated with platinum at 40 mV or 30 s using a Cressington Sputter Coater 208HR. Coated surfaces were viewed using a Mira3 SEM operating at an accelerating voltage of 4.5kV and beam current of 5 in SEI mode.

F-actin preparation

Actin filaments were prepared according to the published protocol (Vogel S K, Elife, 2013). Briefly, rabbit skeletal muscle actin monomers (Molecular Probes) and biotinylated rabbit actin monomers (tebu-bio [Cytoskeleton Inc.]) were mixed in a 5:1 (actin:biotin-actin) ratio. Polymerization of the mixture (39.6 μM) was induced in F-Buffer containing 50mM KCl, 2mM MgCl_2 , 1mM DTT, 1mM ATP, 10mM Tris–HCl buffer (pH 7.5). The biotinylated actin filaments were labeled and stabilized with Alexa-Fluor 488 Phalloidin (Molecular Probes) according to the manufacturer protocol. Finally, 2 μM (refers to monomers) of Alexa-488-Phalloidin labeled biotinylated actin filaments were obtained.

Myofilaments preparation

Myosin was purified from rabbit skeletal muscle tissue as previously described (Smith et al., 2007). Myofilament assembly was induced in reaction buffer containing 50mM KCl, 2mM MgCl_2 , 1mM DTT and 10mM Tris–HCl buffer (pH 7.5). Equilibration of the mixture for approximately 30 min gave us a median length of 560nm in our system. If without specifying, myosin concentration (refer to the monomers) used in the experiments was 0.3 μM .

Active contraction on 3D printed hydrogel structures

Biotinylated 3D hydrogel structures were incubated with 1mg/ml Neutravidin for at least half an hour. Then, the free flowing neutravidin in solution were gently washed away with washing buffer containing 50mM KCl, 2 mM MgCl₂, 10 mM Tris-HCl buffer (pH 7.5). Then the microstructures were further incubated with 0.3 μ M (refer to the monomers) actin pre-formed filaments and 2.25nM neutravidin (neutravidin: biotin-actin, 1:20) for about 2h, following by carefully washing with buffer. For Active contraction, 100 μ l pre-formed myofilaments with 0.5mM ATP were added in the reaction chamber.

Finite-element analysis

The shapes deformed by actomyosin motor system in Figure1 were simulated using the simulation function of Solidworks. For all the simulation, the elastic modulus of the structures printed with different parameters were input into the software. The applied external force were in accordance to the force that can be generated with our actin-myosin system.

3 Discussion and Perspective

Bottom-up reconstitution as a powerful shortcut afford us to explore the mysteries of the mechanisms and molecular origins of life. So far, functional and fundamental biological units, comprised various membrane systems, transcription/translation modules, cytoskeletal, and molecular motors, have already been identified and successfully reconstituted in simplified environments. After all, the secret of life does not only lie in these separated building blocks, but even more in their particular interactions and compatible self-organization in space and time. Towards this end, hierarchical assembly and spatiotemporal connection are being awaited for identification and development. **In this thesis, to address the demands, we developed various spatiotemporal methodological tools and technologies to integrate different functional components compatibly in space and time.**

Firstly, we have developed a synthetic temperature feedback regulation toolbox based on RNA thermometer elements, aiming to manipulate protein production temporally in cell free protein synthesis system. We tuned the thermal response of the thermal-sensor rapidly and simply by an *in vitro* strategy, and finally adapted RNA thermometers for the PURE system⁸⁴. We explored new functional genetic parts of RNA thermometers with broad switching range from 35 to 42 °C, being useful for diverse requirements of gene circuits engineering *in vitro*. Since ionic strength strongly influences the stability of RNA secondary structure⁸⁵, ionic condition change will affect the switching behaviors of RNA Thermometers in cell free system. Therefore, to extend the application to other cell-extract based systems with different iron concentrations, the melting temperature of the same sequence need to be re-adjusted.

Instead of simple regulation of single gene, the next level of applications was extended from thermal genetic circuits to *in vitro* compartmentalized cell free reactions towards artificial cells. As translation level regulators, RNA thermometers can minimize the transcriptional redundancy of the genetic circuits, making them attractive to a minimal cell model. We generated protocells from bottom-up by encapsulating a temperature feedback transcription/translation machinery into picoliter emulsion droplets. Rationally designed synthetic temperature feedback regulation tools could render protocells response to heat, and the capability to convert the environment stimulus into biological signals. With these temperature sensitive devices, the protocells can process different inputs in a deterministic way. We demonstrated a thermally driven gene multiplexer and a logic AND gate, which are capable of processing both thermal and chemical signals. As shown, thermal regulation show promising applications, such as establishing reaction schemes that require a delicate concentration ratio and sequential expression. Dynamic thermal logic circuits capable of compatibly controlling multiple genes provide the logical control of different biological functions in a defined workflow. Although genetic circuits could handle different components working in the same system, the inherent stochasticity noises still cannot be ignored. In this thesis, we have demonstrated that the expression of RFP controlled with RNATs differentiated over time in microcompartment population, which may be due to the stochastic on/off switching of the RNATs, inhomogeneous distributions of materials among different bioreactors or heat damage. Despite the progress we made in understanding the differentiation, how to minimize and control expression differentiation are still open questions in the field and needs to be performed in the future.

Notwithstanding that, the thermo-sensors are not consummate; such tuneable temperature sensitive protocells show new light on a variety of applications in biotechnology, medicine, and industry. For example, by their ability to detect temperature changes, protocells based therapy could be applied to produce, deliver and release pharmaceuticals by sensing the fever of host or artificially focused ultrasound heating. Undoubtedly, further development of environment sensitive logics as shown here within artificial cells or protocells will bring attractive opportunities to many fields.

Having shown, we can program protein production temporally in microcompartments with genetic regulation tools. **Secondly**, we have developed an *in vitro* protein patterning assay on membranes based on the reversible and light-switchable interaction PhyB-PIF6, that can enable spatiotemporal control for bottom-up protein self-assembly. The range of potential and desired applications extends from dynamically controlling local protein interactions in well-defined regions to spatially targeting the self-assembly of larger protein structures on both solid supported and free-standing membranes.

Compared with the classical chemistry-based protein patterning methods *in vitro*⁸⁶⁻⁹⁵, our assay has shown to be compatible with model membranes, allowing us to mimic natural biological regulation processes by utilizing patterned light. The method does not rely on unspecific chemical binding, thus preserves physiological properties. Additionally, optogenetic tools based patterning techniques also show superiority in the aspect of reversible operation, allowing dynamic protein localization. The method can function without special hardware besides widely available confocal microscopes. The high spatial and temporal specificity of light activation establishes this system as a useful tool for local control of protein patterns in two and three dimensions on model membranes. We also demonstrated the generality and orthogonal protein alignment of the approach for sequentially patterning different proteins. Multi-proteins printing can also be successfully processed with our approaches. Our current setup is limited by loading different proteins manually. This can cause laser focus shifts; therefore, custom-made microfluidics will be needed for such extended multicolor patterns in the future to render loading and rinsing more precise. So far, diverse light-inducible protein interaction pairs operating in the visible spectral range have been developed *in vivo* and applied in physiologically relevant studies. Validating the different wavelengths sensitive tools *in vitro* will simplify the multi-printing procedures by switching different wavelengths, and will further facilitate the biorthogonal operation of independent components in large-scale system.

For bottom-up synthetic biology, the ability to guide large-scale and reversible self-assembly of functional protein structures by light can tremendously help in designing minimal cellular systems with desired properties, without having to rely entirely on biochemical cues. We demonstrated printing self-assembling proteins such as the bacterial cytoskeleton protein FtsZ. The targeted assembly into filaments and artificial ring structures can be accomplished, showing promising

applicable potential for large-scale assembly of cell divisome⁹⁶⁻⁹⁷. However, large-scale bottom-up reconstitution could be limited by heavy workload of purification and systematic compatibility. Therefore, it could be interesting to integrate the light targeting system with genetic controllable cell-free protein synthesis system to achieve one-step production and localization. In summary, our light patterning method provides a promising tool for the design of bio-molecular systems composed of proteins and model membranes. Fast patterning of proteins provides a promising tool to track many interactions and activities of proteins on membranes in parallel, representing a new design option for protein microarrays. In the future, approaches like this will greatly help the spatial reconstitution of biological systems from the bottom-up, with a wide range of potential applications from fundamental protocell research to tissue engineering.

Micro-compartments as spatial boundaries represent the most basic unit for synthetic cells. However, the spherical shape of microcompartments, such as giant unilamellar vesicles, renders them rather inappropriate to study phenomena that are based on distinct cell shape and polarity.

Thirdly, we have developed a new toolbox for mechanical manipulation of GUVs - model membrane vesicles, which constitute the basis for the engineering of advanced protocells and should thus be subject to defined shape transformations. We introduced a microscale device based on 3D printed protein hydrogel to induce pH-stimulated reversible shape changes in trapped vesicles without compromising their free-standing membranes. Our hydrogel devices are based on custom-printed BSA protein are thus fully biocompatible. Their dimensions are limited only by the optical resolution of the two-photon laser used for printing. We demonstrated that the swelling ratio depends on the laser power used for printing, such that even more complex designs with differential volume expansion could in principle be realized.

The selective trapping of GUVs by the hydrogel chip allows their size to be roughly controlled, as a first criterion towards establishing geometric anisotropy of vesicles. The trapped GUVs can not only be reversibly compressed, but also molded into arbitrary non-spherical shapes by our laser-printed BSA pH responsive hydrogel structures. Such spatially well-defined microenvironment can mimic the dynamic native cell matrix, allowing us to investigate how synthetic cells react to and interact with external mechanical cues.

Moreover, mechanical force induced by the cages to phase-separated membrane vesicles can lead to spontaneous shape deformations, from the recurrent formation of dumbbells with curved necks

between domains to budding of membrane domains as separate vesicles. Thus, the ability to exert gentle but significant mechanical pressure on GUVs in our custom-designed protein hydrogel cages opens up a fully new way of manipulating vesicle model systems, inducing features that could be of great relevance in the design of cellular mimics, such as shape and differential membrane curvature.

Additionally, the shape-tunable vesicles are particularly desirable when reconstituting membrane polarity- or shape-dependent protein systems, such as the spatiotemporal patterns and oscillations formed by reaction-diffusion of Min systems that request explicitly non-spherical geometries. Our platform opens up a fully new way of using GUVs as custom-made platforms to probe the functionality of reconstituted cellular modules in bottom-up synthetic biology.

In the last section, we programmably engineered and functionalized the contractible 3D hydrogel scaffolds for actin-myosin motor reconstitution. The controllable and contractible scaffolds provide an outstanding *in vitro* platform for investigation of the active contraction, which can be further extended to study cell spreading and migration. Moreover, nanoscale actomyosin motor as a bio-actuator could generate, transmit active contraction and then drive large-scale shape transformation of complex 3D hydrogel scaffolds. Our study shows new light on engineering and programming nano-motor based actuator that are compatible and could be implemented with other soft materials, suggesting new possibilities for applications in biomedical devices and soft robotics.

Overall, we developed a 4D regulation toolbox to facilitate a bottom-up reconstitution both in time and in space. The spatiotemporal regulation of 4D toolbox cover the aspects from dynamic gene transcription & translation, reversible protein interaction, spatially protein positioning, sequentially protein assembly, extend to defining geometrical membrane boundaries and mimicking cellular anisotropic microenvironment. The 4D regulation toolbox presented here is a big step towards achieving the main objectives; however, the non-trivial explorations of hierarchical assembly and spatiotemporal connection are still the tip of iceberg. In this regard, the quest for assembling a synthetic cell from modules in space and time will continue to require great efforts and inspirations from a wider community of biologists, chemists, physicists, biotechnologists as well as micro- and nanotechnologists.

Bibliography

1. Marquardt, D.; Geier, B.; Pabst, G., Asymmetric lipid membranes: towards more realistic model systems. *Membranes* **2015**, *5* (2), 180-196.
2. Schweizer, J.; Loose, M.; Bonny, M.; Kruse, K.; Mönch, I.; Schwille, P., Geometry sensing by self-organized protein patterns. *Proceedings of the National Academy of Sciences* **2012**, *109* (38), 15283-15288.
3. Rudd, A. K.; Valls Cuevas, J. M.; Devaraj, N. K., SNAP-tag-reactive lipid anchors enable targeted and spatiotemporally controlled localization of proteins to phospholipid membranes. *Journal of the American Chemical Society* **2015**, *137* (15), 4884-4887.
4. Chen, X.; Venkatachalapathy, M.; Kamps, D.; Weigel, S.; Kumar, R.; Orlich, M.; Garrecht, R.; Hirtz, M.; Niemeyer, C. M.; Wu, Y. W., “Molecular Activity Painting”: Switch - like, Light - Controlled Perturbations inside Living Cells. *Angewandte Chemie International Edition* **2017**, *56* (21), 5916-5920.
5. Bartelt, S. M.; Chervyachkova, E.; Steinkühler, J.; Ricken, J.; Wieneke, R.; Tampe, R.; Dimova, R.; Wegner, S. V., Dynamic blue light-switchable protein patterns on giant unilamellar vesicles. *Chemical Communications* **2018**, *54* (8), 948-951.
6. Zieske, K.; Schweizer, J.; Schwille, P., Surface topology assisted alignment of Min protein waves. *FEBS letters* **2014**, *588* (15), 2545-2549.
7. Zieske, K.; Schwille, P., Reconstitution of Pole - to - Pole Oscillations of Min Proteins in Microengineered Polydimethylsiloxane Compartments. *Angewandte Chemie International Edition* **2013**, *52* (1), 459-462.
8. Zieske, K.; Schwille, P., Reconstitution of self-organizing protein gradients as spatial cues in cell-free systems. *Elife* **2014**, *3*, e03949.
9. Abraham, T.; Mao, M.; Tan, C., Engineering approaches of smart, bio-inspired vesicles for biomedical applications. *Physical Biology* **2018**, *15* (6), 061001.
10. Shang, L.; Cheng, Y.; Zhao, Y., Emerging droplet microfluidics. *Chemical reviews* **2017**, *117* (12), 7964-8040.
11. Deshpande, S.; Dekker, C., On-chip microfluidic production of cell-sized liposomes. *Nature protocols* **2018**, *13* (5), 856.
12. Deshpande, S.; Spoelstra, W. K.; van Doorn, M.; Kerssemakers, J.; Dekker, C., Mechanical division of cell-sized liposomes. *ACS nano* **2018**, *12* (3), 2560-2568.
13. Yamada, A.; Lee, S.; Bassereau, P.; Baroud, C. N., Trapping and release of giant unilamellar vesicles in microfluidic wells. *Soft Matter* **2014**, *10* (32), 5878-5885.
14. Guo, M. T.; Rotem, A.; Heyman, J. A.; Weitz, D. A., Droplet microfluidics for high-throughput biological assays. *Lab on a Chip* **2012**, *12* (12), 2146-2155.
15. Weiss, M.; Frohnmayer, J. P.; Benk, L. T.; Haller, B.; Janiesch, J.-W.; Heitkamp, T.; Börsch, M.; Lira, R. B.; Dimova, R.; Lipowsky, R., Sequential bottom-up assembly of mechanically stabilized synthetic cells by microfluidics. *Nature materials* **2018**, *17* (1), 89.

16. Yang, Y.; Wang, J.; Shigematsu, H.; Xu, W.; Shih, W. M.; Rothman, J. E.; Lin, C., Self-assembly of size-controlled liposomes on DNA nanotemplates. *Nature chemistry* **2016**, *8* (5), 476.
17. Langecker, M.; Arnaut, V.; Martin, T. G.; List, J.; Renner, S.; Mayer, M.; Dietz, H.; Simmel, F. C., Synthetic lipid membrane channels formed by designed DNA nanostructures. *Science* **2012**, *338* (6109), 932-936.
18. Göpfrich, K.; Li, C.-Y.; Mames, I.; Bhamidimarri, S. P.; Ricci, M.; Yoo, J.; Mames, A.; Ohmann, A.; Winterhalter, M.; Stulz, E., Ion channels made from a single membrane-spanning DNA duplex. *Nano letters* **2016**, *16* (7), 4665-4669.
19. Zhang, Z.; Yang, Y.; Pincet, F.; Llaguno, M. C.; Lin, C., Placing and shaping liposomes with reconfigurable DNA nanocages. *Nature chemistry* **2017**, *9* (7), 653.
20. Franquelim, H. G.; Khmelinskaia, A.; Sobczak, J.-P.; Dietz, H.; Schwille, P., Membrane sculpting by curved DNA origami scaffolds. *Nature communications* **2018**, *9* (1), 811.
21. Czogalla, A.; Franquelim, H. G.; Schwille, P., DNA nanostructures on membranes as tools for synthetic biology. *Biophysical journal* **2016**, *110* (8), 1698-1707.
22. Parolini, L.; Mognetti, B. M.; Kotar, J.; Eiser, E.; Cicuta, P.; Di Michele, L., Volume and porosity thermal regulation in lipid mesophases by coupling mobile ligands to soft membranes. *Nature communications* **2015**, *6*, 5948.
23. Löffler, P. M.; Ries, O.; Rabe, A.; Okholm, A. H.; Thomsen, R. P.; Kjems, J.; Vogel, S., A DNA - Programmed Liposome Fusion Cascade. *Angewandte Chemie International Edition* **2017**, *56* (43), 13228-13231.
24. Korlach, J.; Reichle, C.; Müller, T.; Schnelle, T.; Webb, W., Trapping, deformation, and rotation of giant unilamellar vesicles in octode dielectrophoretic field cages. *Biophysical journal* **2005**, *89* (1), 554-562.
25. Théry, M.; Racine, V.; Piel, M.; Pépin, A.; Dimitrov, A.; Chen, Y.; Sibarita, J.-B.; Bornens, M., Anisotropy of cell adhesive microenvironment governs cell internal organization and orientation of polarity. *Proceedings of the National Academy of Sciences* **2006**, *103* (52), 19771-19776.
26. Bao, M.; Xie, J.; Piruska, A.; Huck, W. T., 3D microniches reveal the importance of cell size and shape. *Nature communications* **2017**, *8* (1), 1962.
27. Deng, N.-N.; Yelleswarapu, M.; Huck, W. T., Monodisperse uni- and multicompartment liposomes. *Journal of the American Chemical Society* **2016**, *138* (24), 7584-7591.
28. Deng, N.-N.; Yelleswarapu, M.; Zheng, L.; Huck, W. T., Microfluidic assembly of monodisperse vesosomes as artificial cell models. *Journal of the American Chemical Society* **2016**, *139* (2), 587-590.
29. Hindley, J. W.; Elani, Y.; McGilvery, C. M.; Ali, S.; Bevan, C. L.; Law, R. V.; Ces, O., Light-triggered enzymatic reactions in nested vesicle reactors. *Nature communications* **2018**, *9* (1), 1093.
30. Lee, K. Y.; Park, S.-J.; Lee, K. A.; Kim, S.-H.; Kim, H.; Meroz, Y.; Mahadevan, L.; Jung, K.-H.; Ahn, T. K.; Parker, K. K., Photosynthetic artificial organelles sustain and control ATP-dependent reactions in a protocellular system. *Nature biotechnology* **2018**, *36*(6): 530.
31. Schuster, B. S.; Reed, E. H.; Parthasarathy, R.; Jahnke, C. N.; Caldwell, R. M.; Bermudez, J. G.; Ramage, H.; Good, M. C.; Hammer, D. A., Controllable protein phase separation and modular recruitment to form responsive membraneless organelles. *Nature communications* **2018**, *9* (1), 2985.
32. Jia, H.; Heymann, M.; Bernhard, F.; Schwille, P.; Kai, L., Cell-free protein synthesis in micro compartments: building a minimal cell from biobricks. *New biotechnology* **2017**, *39*: 199-205.
33. Shin, J.; Noireaux, V., An E. coli cell-free expression toolbox: application to synthetic gene circuits and artificial cells. *ACS synthetic biology* **2012**, *1* (1), 29-41.
34. Takahashi, M. K.; Chappell, J.; Hayes, C. A.; Sun, Z. Z.; Kim, J.; Singhal, V.; Spring, K. J.; Al-Khabouri, S.; Fall, C. P.; Noireaux, V.; Murray, R. M.; Lucks, J. B., Rapidly Characterizing the Fast Dynamics of RNA Genetic Circuitry with Cell-Free Transcription Translation (TX-TL) Systems. *ACS synthetic biology* **2015**, *4* (5), 503-515.
35. Green, A. A.; Silver, P. A.; Collins, J. J.; Yin, P., Toehold switches: de-novo-designed regulators of gene expression. *Cell* **2014**, *159* (4), 925-939.

36. Martini, L.; Mansy, S. S., Cell-like systems with riboswitch controlled gene expression. *Chemical Communications* **2011**, 47 (38), 10734-10736.
37. Sadler, F. W.; Dodevski, I.; Sarkar, C. A., RNA thermometers for the PURExpress system. *ACS synthetic biology* **2017**, 7 (1), 292-296.
38. Kobori, S.; Ichihashi, N.; Kazuta, Y.; Yomo, T., A controllable gene expression system in liposomes that includes a positive feedback loop. *Molecular bioSystems* **2013**, 9 (6), 1282-1285.
39. Takahashi, M. K.; Hayes, C. A.; Chappell, J.; Sun, Z. Z.; Murray, R. M.; Noireaux, V.; Lucks, J. B., Characterizing and prototyping genetic networks with cell-free transcription-translation reactions. *Methods* **2015**, 86, 60-72.
40. Niederholtmeyer, H.; Sun, Z. Z.; Hori, Y.; Yeung, E.; Verpoorte, A.; Murray, R. M.; Maerkl, S. J., Rapid cell-free forward engineering of novel genetic ring oscillators. *Elife* **2015**, 4, e09771.
41. Hutchison, C. A.; Chuang, R.-Y.; Noskov, V. N.; Assad-Garcia, N.; Deerinck, T. J.; Ellisman, M. H.; Gill, J.; Kannan, K.; Karas, B. J.; Ma, L., Design and synthesis of a minimal bacterial genome. *Science* **2016**, 351 (6280), aad6253.
42. Richardson, S. M.; Mitchell, L. A.; Stracquadanio, G.; Yang, K.; Dymond, J. S.; DiCarlo, J. E.; Lee, D.; Huang, C. L. V.; Chandrasegaran, S.; Cai, Y., Design of a synthetic yeast genome. *Science* **2017**, 355 (6329), 1040-1044.
43. Deng, N.-N.; Vibhute, M.; Zheng, L.; Zhao, H.; Yelleswarapu, M.; Huck, W. T., Macromolecularly crowded protocells from reversibly shrinking monodisperse liposomes. *Journal of the American Chemical Society* **2018**, 140(24): 7399-7402.
44. Hansen, M. M.; Meijer, L. H.; Spruijt, E.; Maas, R. J.; Rosquelles, M. V.; Groen, J.; Heus, H. A.; Huck, W. T., Macromolecular crowding creates heterogeneous environments of gene expression in picolitre droplets. *Nature nanotechnology* **2016**, 11 (2), 191.
45. van Nies, P.; Westerlaken, I.; Blanken, D.; Salas, M.; Mencía, M.; Danelon, C., Self-replication of DNA by its encoded proteins in liposome-based synthetic cells. *Nature communications* **2018**, 9 (1), 1583.
46. Dudley, Q. M.; Karim, A. S.; Jewett, M. C., Cell - free metabolic engineering: biomanufacturing beyond the cell. *Biotechnology journal* **2015**, 10 (1), 69-82.
47. Howorka, S., Building membrane nanopores. *Nature nanotechnology* **2017**, 12 (7), 619.
48. Adamala, K. P.; Martin-Alarcon, D. A.; Guthrie-Honea, K. R.; Boyden, E. S., Engineering genetic circuit interactions within and between synthetic minimal cells. *Nature chemistry* **2017**, 9 (5), 431.
49. Lentini, R.; Santero, S. P.; Chizzolini, F.; Cecchi, D.; Fontana, J.; Marchiorretto, M.; Del Bianco, C.; Terrell, J. L.; Spencer, A. C.; Martini, L., Integrating artificial with natural cells to translate chemical messages that direct E. coli behaviour. *Nature communications* **2014**, 5.
50. Gardner, P. M.; Winzer, K.; Davis, B. G., Sugar synthesis in a protocellular model leads to a cell signalling response in bacteria. *Nature Chemistry* **2009**, 1 (5), 377-383.
51. Schwarz-Schilling, M.; Aufinger, L.; Mückl, A.; Simmel, F., Chemical communication between bacteria and cell-free gene expression systems within linear chains of emulsion droplets. *Integrative Biology* **2016**, 8 (4), 564-570.
52. Qiao, Y.; Li, M.; Booth, R.; Mann, S., Predatory behaviour in synthetic protocell communities. *Nature chemistry* **2017**, 9 (2), 110.
53. Villar, G.; Graham, A. D.; Bayley, H., A tissue-like printed material. *Science* **2013**, 340 (6128), 48-52.
54. Dupin, A.; Simmel, F. C., Signalling and differentiation in emulsion-based multi-compartmentalized in vitro gene circuits. *Nature chemistry* **2019**, 11 (1), 32.
55. Loose, M.; Mitchison, T. J., The bacterial cell division proteins FtsA and FtsZ self-organize into dynamic cytoskeletal patterns. *Nature cell biology* **2014**, 16 (1), 38.
56. Ramirez-Diaz, D. A.; García-Soriano, D. A.; Raso, A.; Mücksch, J.; Feingold, M.; Rivas, G.; Schwille, P., Treadmilling analysis reveals new insights into dynamic FtsZ ring architecture. *PLoS biology* **2018**, 16 (5), e2004845.

57. Loose, M.; Fischer-Friedrich, E.; Ries, J.; Kruse, K.; Schwille, P., Spatial regulators for bacterial cell division self-organize into surface waves in vitro. *Science* **2008**, *320* (5877), 789-792.
58. Ramm, B.; Glock, P.; Mücksch, J.; Blumhardt, P.; García-Soriano, D. A.; Heymann, M.; Schwille, P., The MinDE system is a generic spatial cue for membrane protein distribution in vitro. *Nature communications* **2018**, *9* (1), 3942.
59. Vogel, S. K.; Petrusek, Z.; Heinemann, F.; Schwille, P., Myosin motors fragment and compact membrane-bound actin filaments. *Elife* **2013**, *2*, e00116.
60. Reymann, A.-C.; Martiel, J.-L.; Cambier, T.; Blanchoin, L.; Boujemaa-Paterski, R.; Théry, M., Nucleation geometry governs ordered actin networks structures. *Nature materials* **2010**, *9* (10), 827.
61. Reymann, A.-C.; Boujemaa-Paterski, R.; Martiel, J.-L.; Guérin, C.; Cao, W.; Chin, H. F.; Enrique, M.; Théry, M.; Blanchoin, L., Actin network architecture can determine myosin motor activity. *Science* **2012**, *336* (6086), 1310-1314.
62. Ennomani, H.; Letort, G.; Guérin, C.; Martiel, J.-L.; Cao, W.; Nédélec, F.; Enrique, M.; Théry, M.; Blanchoin, L., Architecture and connectivity govern actin network contractility. *Current Biology* **2016**, *26* (5), 616-626.
63. Galland, R.; Leduc, P.; Guérin, C.; Peyrade, D.; Blanchoin, L.; Théry, M., Fabrication of three-dimensional electrical connections by means of directed actin self-organization. *Nature materials* **2013**, *12* (5), 416.
64. Hariadi, R. F.; Sommese, R. F.; Sivaramakrishnan, S., Tuning myosin-driven sorting on cellular actin networks. *Elife* **2015**, *4*, e05472.
65. e Silva, M. S.; Alvarado, J.; Nguyen, J.; Georgoulia, N.; Mulder, B. M.; Koenderink, G. H., Self-organized patterns of actin filaments in cell-sized confinement. *Soft Matter* **2011**, *7* (22), 10631-10641.
66. Cao, L.; Kerleau, M.; Suzuki, E. L.; Wioland, H.; Jouet, S.; Guichard, B.; Lenz, M.; Romet-Lemonne, G.; Jegou, A., Modulation of formin processivity by profilin and mechanical tension. *eLife* **2018**, *7*, e34176.
67. Zieske, K.; Chwastek, G.; Schwille, P., Protein patterns and oscillations on lipid monolayers and in microdroplets. *Angewandte Chemie International Edition* **2016**, *55* (43), 13455-13459.
68. Osawa, M.; Anderson, D. E.; Erickson, H. P., Reconstitution of contractile FtsZ rings in liposomes. *Science* **2008**, *320* (5877), 792-794.
69. Miyazaki, M.; Chiba, M.; Eguchi, H.; Ohki, T.; Ishiwata, S. i., Cell-sized spherical confinement induces the spontaneous formation of contractile actomyosin rings in vitro. *Nature cell biology* **2015**, *17* (4), 480.
70. Kurokawa, C.; Fujiwara, K.; Morita, M.; Kawamata, I.; Kawagishi, Y.; Sakai, A.; Murayama, Y.; Shin-ichiro, M. N.; Murata, S.; Takinoue, M., DNA cytoskeleton for stabilizing artificial cells. *Proceedings of the National Academy of Sciences* **2017**, *114* (28), 7228-7233.
71. Pan, J.; Li, F.; Cha, T.-G.; Chen, H.; Choi, J. H., Recent progress on DNA based walkers. *Current opinion in biotechnology* **2015**, *34*, 56-64.
72. Omabegho, T.; Gurel, P. S.; Cheng, C. Y.; Kim, L. Y.; Ruijgrok, P. V.; Das, R.; Alushin, G. M.; Bryant, Z., Controllable molecular motors engineered from myosin and RNA. *Nature nanotechnology* **2018**, *13* (1), 34.
73. Hariadi, R. F.; Appukutty, A. J.; Sivaramakrishnan, S., Engineering Circular Gliding of Actin Filaments Along Myosin-Patterned DNA Nanotube Rings To Study Long-Term Actin–Myosin Behaviors. *ACS nano* **2016**, *10* (9), 8281-8288.
74. Hariadi, R.; Sommese, R.; Adhikari, A.; Taylor, R.; Sutton, S.; Spudich, J.; Sivaramakrishnan, S., Mechanical coordination in motor ensembles revealed using engineered artificial myosin filaments. *Nature nanotechnology* **2015**, *10* (8), 696.
75. Meier, E. L.; Goley, E. D., Form and function of the bacterial cytokinetic ring. *Current opinion in cell biology* **2014**, *26*, 19-27.
76. Carvalho, K.; Tsai, F. C.; Lees, E.; Voituriez, R.; Koenderink, G. H.; Sykes, C., Cell-sized liposomes reveal how actomyosin cortical tension drives shape change. *Proceedings of the National Academy of Sciences* **2013**, *110*(41): 16456-16461.

77. Jia, H.; Sun, X.; Sun, H.; Li, C.; Wang, Y.; Feng, X.; Li, C., Intelligent Microbial Heat-Regulating Engine (IMHeRE) for Improved Thermo-Robustness and Efficiency of Bioconversion. *ACS synthetic biology* **2016**, *5* (4), 312-320.
78. Papworth, C.; Bauer, J.; Braman, J.; Wright, D., Site-directed mutagenesis in one day with > 80% efficiency. *Strategies* **1996**, *8*: 3-4.
79. Wagner, O.; Thiele, J.; Weinhart, M.; Mazutis, L.; Weitz, D. A.; Huck, W. T.; Haag, R., Biocompatible fluorinated polyglycerols for droplet microfluidics as an alternative to PEG-based copolymer surfactants. *Lab on a Chip* **2016**, *16* (1), 65-69.
80. Schindelin, J.; Arganda-Carreras, I.; Frise, E.; Kaynig, V.; Longair, M.; Pietzsch, T.; Preibisch, S.; Rueden, C.; Saalfeld, S.; Schmid, B., Fiji: an open-source platform for biological-image analysis. *Nature methods* **2012**, *9* (7), 676-682.
81. Shimizu, Y.; Inoue, A.; Tomari, Y.; Suzuki, T.; Yokogawa, T.; Nishikawa, K.; Ueda, T., Cell-free translation reconstituted with purified components. *Nature biotechnology* **2001**, *19* (8), 751-755.
82. Xue, Y.; Gracia, B.; Herschlag, D.; Russell, R.; Al-Hashimi, H. M., Visualizing the formation of an RNA folding intermediate through a fast highly modular secondary structure switch. *Nature communications* **2016**, *7*: ncomms11768.
83. Thirumalai, D.; Denesyuk, N. A., How do metal ions direct ribozyme folding? *bioRxiv* **2016**, 037895.
84. Shimizu, Y.; Inoue, A.; Tomari, Y.; Suzuki, T.; Yokogawa, T.; Nishikawa, K.; Ueda, T., Cell-free translation reconstituted with purified components. *Nature biotechnology* **2001**, *19* (8), 751.
85. Draper, D. E., A guide to ions and RNA structure. *Rna* **2004**, *10* (3), 335-343.
86. Bélisle, J. M.; Correia, J. P.; Wiseman, P. W.; Kennedy, T. E.; Costantino, S., Patterning protein concentration using laser-assisted adsorption by photobleaching, LAPAP. *Lab on a Chip* **2008**, *8* (12), 2164-2167.
87. Hong, S.; Zhu, J.; Mirkin, C. A., Multiple ink nanolithography: toward a multiple-pen nano-plotter. *Science* **1999**, *286* (5439), 523-525.
88. Scott, M. A.; Wissner-Gross, Z. D.; Yanik, M. F., Ultra-rapid laser protein micropatterning: screening for directed polarization of single neurons. *Lab on a Chip* **2012**, *12* (12), 2265-2276.
89. Théry, M., Micropatterning as a tool to decipher cell morphogenesis and functions. *J Cell Sci* **2010**, *123* (24), 4201-4213.
90. Martin, T. A.; Herman, C. T.; Limpoco, F. T.; Michael, M. C.; Potts, G. K.; Bailey, R. C., Quantitative photochemical immobilization of biomolecules on planar and corrugated substrates: a versatile strategy for creating functional biointerfaces. *ACS applied materials & interfaces* **2011**, *3* (9), 3762-3771.
91. Falconnet, D.; Csucs, G.; Grandin, H. M.; Textor, M., Surface engineering approaches to micropattern surfaces for cell-based assays. *Biomaterials* **2006**, *27* (16), 3044-3063.
92. Strale, P. O.; Azioune, A.; Bugnicourt, G.; Lecomte, Y.; Chahid, M.; Studer, V., Multiprotein Printing by Light - Induced Molecular Adsorption. *Advanced Materials* **2016**, *28* (10), 2024-2029.
93. Gatterdam, V.; Ramadass, R.; Stoess, T.; Fichte, M. A.; Wachtveitl, J.; Heckel, A.; Tampé, R., Three - Dimensional Protein Networks Assembled by Two - Photon Activation. *Angewandte Chemie International Edition* **2014**, *53* (22), 5680-5684.
94. Labòria, N.; Wieneke, R.; Tampé, R., Control of nanomolar interaction and in situ assembly of proteins in four dimensions by light. *Angewandte Chemie International Edition* **2013**, *52* (3), 848-853.
95. Reuther, C.; Tucker, R.; Ionov, L.; Diez, S., Programmable patterning of protein bioactivity by visible light. *Nano letters* **2014**, *14* (7), 4050-4057.
96. Lutkenhaus, J.; Pichoff, S.; Du, S., Bacterial cytokinesis: from Z ring to divisome. *Cytoskeleton* **2012**, *69* (10), 778-790.
97. Martos, A.; Jiménez, M.; Rivas, G.; Schwille, P., Towards a bottom-up reconstitution of bacterial cell division. *Trends in cell biology* **2012**, *22* (12), 634-643.

Abbreviations

2D	Two dimensions
3D	Three dimensions
ATP	Adenosine triphosphate
ARBS	Anti-ribosome binding sites
BSA	Bovine serum albumin
CFPS	cell free protein synthesis
CDS	Coding sequence
CCD	Charge-coupled device
Ch	Cholesterol
DNA	deoxyribonucleic
DOPC	1,2-dioleoyl-sn-glycero-3-phosphocholine
DOGS-NTA	1,2-dioleoyl-sn-glycero-3-[(N-(5-amino-1-carboxypentyl)iminodiacetic acid)succinyl]
DOPE	1,2-dioleoyl-sn-glycero-3-phosphoethanolamine
DMSO	Dimethyl sulfoxide
DOPG	1,2-dielaidoyl-sn-glycero-3-phospho-(1'-rac-glycerol)
EGFP	Enhanced green fluorescent protein
EYFP	Enhanced yellow fluorescence protein
FtsZ	Filamenting temperature-sensitive mutant Z
F-actin	Filament actin
FRAP	Fluorescence recovery after photobleaching
GTP	Guanosine-5'-triphosphate

Abbreviations

GUVs	Giant unilamellar vesicles
IPTG	Isopropyl β -D-1-thiogalactopyranoside
LOV	Light-Oxygen-Voltage
LSM	Laser scanning microscope
LED	Light-emitting diode
Lo	liquid-ordered phase
Ld	liquid-disordered phase
Ni-NTA	Nickel nitrilotriacetic acid
NBD-DSPE	1,2-distearoyl-sn-glycero-3-phosphoethanolamine-N-(7-nitro-2-1,3-benzoxadiazol-4-yl)
PhyB	Phytochrome B
PIF	Phytochrome interacting factors
PCB	Phycocyanobilin
POI	Protein of interest
PMSF	Phenylmethanesulfonyl fluoride
PDMS	polydimethylsiloxane
PBS	Phosphate Buffered Saline
RNATs	RNA thermometers
RNA	Ribonucleic acid
RBS	Ribosome binding sites
RFP	Red fluorescent protein
SLBs	Supported lipid bilayers
SM	Sphingomyelin
SOAX	Stretching open active contours
SUVs	Small unilamellar vesicles
TIRF	Total internal reflection fluorescent microscope
UV	Ultraviolet

Acknowledgments

My wonderful PhD adventure has finally draw to an end. Its completion is thanks in large part to the special people who challenged, supported and stuck with me along the way.

First and foremost, I would like to express my sincere gratitude to my advisor Prof. Petra Schuille for the continuous support of my PhD study and research, for her patience, motivation, enthusiasm, and immense knowledge, for the inspiring research environment and academic freedom she generated. If I become only half the scientist and half the thinker that Petra is, I will be surely be one of my greatest accomplishments.

Moreover, I would like to express the deep appreciation to the members of Thesis Advisory Committee, Prof. Kirsten Jung and Dr. Tobias Härtel. I will thank them for their scientific input, valuable suggestions and thoughtful feedback, always aiming to move me forward. I would particularly like to thank Dr. Tobias Härtel for his support and help, especially in the beginning of my PhD study.

My sincere thanks also goes to Dr. Kai Lei, Dr. Michael Heymann, Dr. Henri Franquelim and Dr. Sven Vogel. It is a great fortunate to meet Lei here. Lei also gives insightful comments and great help in science. I obtained a lot of knowledge of cell free system and protein purification from him. Michael is the giant, for not only his height, but also his knowledge. He always has tones of ideas and gives me constructive comments. I also want to thank Henri for help of membrane and AFM. Henri's meticulous comments were an enormous help to me. I am indebt to Sven for his help of actin-myosin system. I quite enjoy our collaboration project.

I would like to offer my special thanks to Dr. Frank Siedler for the SEM support. Special thanks also to Thomas Litschel for Min oscillation application, to Hiro Eto for the Nanoscribe and 3D printing setup.

Acknowledgments

I would like to express my gratitude to our secretary, Silke, for her general supports.

Moreover, I would like to thank all the TAs and all other Schwille group members.

I am highly grateful for the collaboration with Prof. Dr. Chase Broedersz, David Brueckner and Johannes Flommersfeld, who analyzed the actin-myosin contraction on 3D hydrogel theoretically.

I would like to thank GRK2062 (Research Training Group GRK2062 Molecular Principles of Synthetic Biology) and the amazing network of people.

I am incredibly grateful for the support of my family: my parents and sister for enduring support of me over years. Last but not least, I would sincerely thank the most important person for me: my love Huan Sun. She provides love, companionship and entertainment, and brings so much happiness to my life. Loving in long distance makes us cherish each other in joy and in sorrow. She is constantly at my side and makes my abroad life not lonely. Collisions of thought in science with her give me a lot of inspiration.

Curriculum Vitae

Haiyang Jia

Zhangjiakou, Hebei, China

EDUCATION

Max Planck Institute of Biochemistry

PhD student, Cellular and Molecular Biophysics

Mentor: Prof. Petra Schwille

Thesis Advisory Committee: Prof. Kirsten Jung; Dr. Tobias Härtel

Topic: 4D regulation toolbox for bottom-up synthetic biology

Martinsried, Germany
2015-present

Beijing Institute of Technology

Master degree, Chemical Engineering and Technology

Supervisor: Prof. Chun Li

Topic: Intelligent Microbial Heat Regulating Engine (IMHeRE) for Improving Thermo-robustness and Efficiency of Bioconversion

Beijing, China
2012-2015

Shihezi University

Bachelor degree, Biological Science

Topic: *Cath5* enhancing the resistibility of the *Arabidopsis* to *Aphid*

Xinjiang, China
2008-2012

ADWARDS

2013 iGEM, Gold medal, World Championship

2014 iGEM, Gold medal, The Giant Jamboree

2015 Excellent Graduate Student, Beijing Institute of Technology

PUBLICATIONS

Haiyang Jia, et al. Active contraction driving 4D protein origami, in preparation.

Huan Sun, **Haiyang Jia**, et al. Exploring ageing of cell division by site-specific incorporation of halogen modified Tyr, in preparation.

Haiyang Jia, Thomas Litschel, et al. Shaping membrane vesicles in 3D-printed protein hydrogel cages, submitted.

Haiyang Jia, Michael Heymann, et al. Temperature-sensitive protein expression in protocells[J]. **Chemical Communications**, 2019, DOI: 10.1039/C9CC02734C

Haiyang Jia, Petra Schwille. Bottom-up synthetic biology: reconstitution in space and time [J]. **Current opinion in biotechnology**, 2019, 60:179–187.

Haiyang Jia, Kai Lei, Michael Heymann, et al. Light-induced Printing of Protein Structures on Membranes in vitro[J]. **Nano letters**, 2018, 18(11): 7133-7140.

Haiyang Jia, Michael Heymann, Frank Bernhard, et al. Cell-free protein synthesis in micro compartments: building a minimal cell from biobricks[J]. **New biotechnology**, 2017, 39: 199-205.

Huan Sun*, **Haiyang Jia***, et al. Rational synthetic combination genetic devices boosting high temperature ethanol fermentation [J]. **Synthetic and systems biotechnology**, 2017, 2(2): 121-129.(* Equal contribution)

Haiyang Jia, Xiangying Sun Huan Sun, Chun Li et al., Intelligent Microbial Heat Regulating Engine (IMHeRE) for Improving Thermo-robustness and Efficiency of Bioconversion, **ACS Synthetic Biology**, 2016, 5(4): 312-320

Haiyang Jia, Yanshuang Fan, Xudong Feng, Chun Li. Enhancing stress-resistance for efficient microbial biotransformations by synthetic biology. **Frontiers in Bioengineering and Biotechnology** 2, 2014.00044

Haiyang Jia, Huan Sun, Xiangying Sun, Chun Li, Construction and Application of Temperature Sensitive Thermotolerant System in *Escherichia coli*, **CIESC Journal**, 2015: 0-0. (DOI: 10.11949/j.issn.0438-1157. 20141929, EI)

Genlin Zhang, Feng Qi, **Haiyang Jia**, et al. Advances in bioprocessing for efficient bio manufacture [J]. **Rsc Advances**, 2015, 5(65): 52444-52451.